

# **Synthesis of Conjugated Polymers and Small Molecules for Organic Light-Emitting Devices and Photodetectors**

by

**Petri Murto**

*Thesis  
Submitted to Flinders University  
for the degree of*

**Doctor of Philosophy**  
College of Science and Engineering  
13 November 2018

---



THESIS FOR THE DEGREE OF DOCTOR OF PHILOSOPHY

**Synthesis of Conjugated Polymers and Small Molecules for  
Organic Light-Emitting Devices and Photodetectors**

PETRI MURTO



Department of Chemistry and Chemical Engineering

CHALMERS UNIVERSITY OF TECHNOLOGY

Gothenburg, Sweden 2018

Synthesis of Conjugated Polymers and Small Molecules for  
Organic Light-Emitting Devices and Photodetectors

PETRI MURTO

ISBN 978-91-7597-800-0

© PETRI MURTO, 2018.

Doktorsavhandlingar vid Chalmers tekniska högskola

Ny serie nr 4481

ISSN 0346-718X

Division of Applied Chemistry

Department of Chemistry and Chemical Engineering

Chalmers University of Technology

SE-412 96 Gothenburg

Sweden

Telephone + 46 (0)31-772 1000

and

Flinders Institute for Nanoscale Science & Technology

Flinders University

Sturt Road, Bedford Park, Adelaide, South Australia 5042

Australia

Telephone + 61 (08) 8201 3911

I certify that this thesis does not incorporate without acknowledgment any material previously submitted for a degree or diploma in any university; and that to the best of my knowledge and belief it does not contain any material previously published or written by another person except where due reference is made in the text.

Cover:

Unintended crystallization of an oily, red fluorescent monomer during storing in a low-polarity solvent. Image taken by an optical microscope.

Printed by Chalmers Reproservice  
Gothenburg, Sweden 2018.

# Synthesis of Conjugated Polymers and Small Molecules for Organic Light-Emitting Devices and Photodetectors

Petri Murto

Department of Chemistry and Chemical Engineering  
Chalmers University of Technology

## Abstract

Production cost and environmental impact are the two major concerns that are related to the conventional optoelectronic devices. It is desirable for the modern semiconductors that they are free of toxic/costly metals, they can be processed with low-cost solution-based methods, and their optical, electronic, and mechanical properties can be easily tuned depending on the target application. In this thesis, a range of different conjugated polymers and small molecules are designed and synthesized as semiconductors for organic light-emitting diodes (OLEDs), light-emitting electrochemical cells (LECs), and organic photodetectors (OPDs).

In organic light-emitting devices, the emissive molecule is commonly mixed with a charge transporting host matrix, which can be either a small molecule or a conjugated polymer. The latter is beneficial since it does not require deposition of the emitter and matrix components in high vacuum and high temperature conditions. The polymeric materials can be dissolved and printed on a substrate of any desired size and production scale, at room temperature, and even under ambient air. The specific wavelength range of near-infrared (NIR) at  $\lambda > 700$  nm is of interest for a wide range of applications spanning from optical communication to biosensing. However, the low energy of NIR range poses challenges for the materials design, in terms of emission efficiency and light intensity, which are further addressed in this thesis, allowing the fabrication of high-performance NIR-OLEDs and NIR-LECs.

For photodetectors, absorption of a wide spectrum of light is beneficial in biosensing and imaging applications. Low noise and fast charge extraction are necessary for the detection of light at high speeds even at low intensities. These aspects are studied in this thesis by designing new polymers with different absorption, charge transport, and morphological properties in the photoactive layer. Two polymers enabled the fabrication of visible (red) OPDs with a low dark current (the main constituent in the noise), high detectivity, and high photoresponse speed.

Keywords: *conjugated polymers, fluorescence, light-emitting electrochemical cell, near-infrared, organic light-emitting diode, organic photodetector, solution processing*

## List of Publications

This thesis is based on the work contained in the following papers, referred to by Roman numerals in the text:

**Paper I. Triazolobenzothiadiazole-Based Copolymers for Polymer Light-Emitting Diodes: Pure Near-Infrared Emission via Optimized Energy and Charge Transfer.** Petri Murto, Alessandro Minotto, Andrea Zampetti, Xiaofeng Xu, Mats R. Andersson, Franco Cacialli, Ergang Wang, *Advanced Optical Materials* **2016**, *4*, 2068–2076.

**Paper II. Efficient Near-Infrared Electroluminescence at 840 nm with “Metal-Free” Small-Molecule:Polymer Blends.** Alessandro Minotto, Petri Murto, Zewdneh Genene, Andrea Zampetti, Giuseppe Carnicella, Wendimagegn Mammo, Mats R. Andersson, Ergang Wang, Franco Cacialli, *Advanced Materials* **2018**, 1706584.

**Paper III. Intense and Stable Near-Infrared Emission from Light-Emitting Electrochemical Cells Comprising a Metal-Free Indacenodithieno[3,2-*b*]thiophene-Based Copolymer as the Single Emitter.** Shi Tang, Petri Murto, Xiaofeng Xu, Christian Larsen, Mats R. Andersson, Ergang Wang, Ludvig Edman, *Chemistry of Materials* **2017**, *29*, 7750–7759.

**Paper IV. Incorporation of Designed Donor–Acceptor–Donor Segments in a Host Polymer for Strong Near-Infrared Emission from a Large-Area Light-Emitting Electrochemical Cell.** Petri Murto, Shi Tang, Christian Larsen, Xiaofeng Xu, Andreas Sandström, Juuso Pietarinen, Benedikt Bagemihl, Birhan A. Abdulahi, Wendimagegn Mammo, Mats R. Andersson, Ergang Wang, Ludvig Edman, *ACS Applied Energy Materials* **2018**, *1*, 1753–1761.

**Paper V. High Performance Organic Photodetectors from a High-Bandgap Indacenodithiophene-Based  $\pi$ -Conjugated Donor–Acceptor Polymer.** Cindy Montenegro Benavides, Petri Murto, Christos L. Chochos, Vasilis G. Gregoriou, Apostolos Avgeropoulos, Xiaofeng Xu, Kim Bini, Anirudh Sharma, Mats R. Andersson, Oliver Schmidt, Christoph J. Brabec, Ergang Wang, Sandro F. Tedde, *ACS Applied Materials & Interfaces* **2018**, *10*, 12937–12946.

**Paper VI. High Performance All-Polymer Photodetector Comprising a Donor–Acceptor–Acceptor Structured Indacenodithiophene–Bithieno[3,4-*c*]Pyrroletetrone Copolymer.** Petri Murto, Zewdneh Genene, Cindy Montenegro Benavides, Xiaofeng Xu, Anirudh Sharma, Xun Pan, Oliver Schmidt, Christoph J. Brabec, Mats R. Andersson, Sandro F. Tedde, Wendimagegn Mammo, Ergang Wang, *ACS Macro Letters* **2018**, 7, 395–400.

## **Contribution Report**

**Paper I.** Equal contribution from P.M and A.M. Designed all the materials and performed the synthesis and characterization: NMR, MALDI-TOF, TGA, DSC, and CV. Performed the DFT calculations and part of the optical characterization at Chalmers. The optical measurements and device characterization was carried out by A.M. and A.Z. at UCL. Main author, wrote the first draft of the manuscript together with A.M. and revised it with all coauthors.

**Paper II.** Equal contribution from A.M. and P.M. Designed and synthesized the PIDT-TPD polymer and the BTT\* small molecule. PIDT-2TPD was synthesized by Z.G. at Addis Ababa University. Performed the characterization: NMR, MALDI-TOF, TGA, DSC, and CV, as well as the DFT calculations. The optical characterization and device fabrication was carried out by, and partially together with, A.M., A.Z., and G.C. at UCL. Wrote the first draft of the manuscript together with A.M. and revised it with all coauthors.

**Paper III.** Equal contribution from S.T. and P.M. Performed the synthesis of the polymers together with X.X. and characterized the polymers: NMR, TGA, and CV. Performed the DFT calculations. The optical characterization was done partially at Chalmers and partially by S.T. at Umeå University. The device fabrication was done by S.T. and C.L. at Umeå University. Wrote the first draft of the manuscript together with S.T. and revised it with all coauthors.

**Paper IV.** Equal contribution from P.M. and S.T. Designed all the materials and performed majority of the synthesis and characterization: NMR, MALDI-TOF, and CV. Performed the DFT calculations. The B<sub>R</sub> monomer was synthesized by X.X. at Chalmers and B.A.A. at Addis Ababa University. J.P. and B.B. contributed to the synthesis of the monomers and polymers at Chalmers. Optical characterization was done partially at Flinders University and partially by S.T. at Umeå University. The device fabrication was done by S.T., C.L., and A.S. at Umeå University and LunaLEC AB. Main author, wrote the first draft of the manuscript together with S.T. and revised it with all coauthors.

**Paper V.** Equal contribution from C.M.B. and P.M. Synthesized the PIDT-TPD polymer (medium  $M_n$  polymer in the paper). Performed the optical characterization and the NMR, CV, and AFM. Performed the TEM imaging together with K.B. and C.M.B. at Chalmers. Carried out the DMTA measurements together with A.S. and X.P. at Flinders University. The device fabrication was done by C.M.B. at Siemens Healthineers. Wrote the first draft of the manuscript together with C.M.B. and revised it with all coauthors.

**Paper VI.** Equal contribution from P.M., Z.G., and C.M.B. PIDT-2TPD was synthesized by Z.G. at Addis Ababa University. Performed the optical characterization and the NMR, CV, and AFM. Performed the DMTA measurements together with A.S. at Flinders University. The device fabrication was done by C.M.B. at Siemens Healthineers. Processed the device data together with C.M.B. Main author, wrote the first draft of the manuscript together with Z.G. and C.M.B. and revised it with all coauthors.

## **Publications Not Included in the Thesis**

**Paper A. Open-Circuit Voltage Modulations on All-Polymer Solar Cells by Side Chain Engineering on 4,8-Di(thiophen-2-yl)benzo[1,2-*b*:4,5-*b'*]dithiophene-Based Donor Polymers.** Birhan A. Abdulahi, Xiaofeng Xu, Petri Murto, Olle Inganäs, Wendimagegn Mammo, Ergang Wang, *ACS Applied Energy Materials* **2018**, *1*, 2918–2926.

**Paper B. Broad Spectrum Absorption and Low-Voltage Electrochromic Operation from Indacenodithieno[3,2-*b*]thiophene-Based Copolymers.** Kim Bini, Petri Murto, Sait Elmas, Mats R. Andersson, Ergang Wang, *Manuscript*.

**Paper C. On the Design of Host–Guest Light-Emitting Electrochemical Cells: Should the Emissive Guest be Physically Blended or Chemically Incorporated into the Host for Efficient Operation?** Shi Tang, Petri Murto, Jia Wang, Christian Larsen, Mats R. Andersson, Ergang Wang, Ludvig Edman, *Manuscript*.

**Paper D. Experimental Demonstration of Staggered CAP Modulation for Low Bandwidth Polymer-LED Based Visible Light Communications.** Paul Anthony Haigh, Alessandro Minotto, Petri Murto, Zewdneh Genene, Wendimagegn Mammo, Mats R. Andersson, Ergang Wang, Ioannis Papakonstantinou, Franco Cacialli, Izzat Darwazeh, *Manuscript*.

## Nomenclature

2T	2,2'-Bithiophene
2TPD	Bithieno[3,4- <i>c</i> ]pyrrole-4,4',6,6'-tetrone
2T <sub>R</sub>	3,3'-Ditetradecyl-2,2'-bithiophene
$\alpha$	Absorption coefficient
A	Acceptor
Abs or $A_\lambda$	Absorbance
AFM	Atomic force microscopy
AIE	Aggregation-induced emission
All-PPD	All-polymer photodetector
B or BT	Benzo[ <i>c</i> ][1,2,5]thiadiazole
BHJ	Bulk heterojunction
B <sub>R</sub>	5,6-Bis(dodecyloxy)benzo[ <i>c</i> ][1,2,5]thiadiazole
BTF	5,6-Difluorobenzo[ <i>c</i> ][1,2,5]thiadiazole
BTT	6-(2-Butyloctyl)-4,8-di(thiophen-2-yl)-[1,2,3]triazolo[4',5':4,5]benzo[1,2- <i>c</i> ][1,2,5]thiadiazole
BTT*	6-(2-Butyloctyl)-4,8-bis(5'-(2-butyloctyl)-[2,2'-bithiophen]-5-yl)-1 <i>H</i> -[1,2,3]triazolo[4',5':4,5]benzo[1,2- <i>c</i> ][1,2,5]thiadiazole
CMD	Concerted metalation–deprotonation
Cp	Cyclopentadienyl
CT	Charge-transfer state
CV	Cyclic voltammetry
D	Donor
$D^*$	Specific detectivity
dba	Dibenzylideneacetone
$\Delta E_p$	Peak potential difference
$\Delta E_{ST}$	Singlet–triplet energy gap
DFT	Density-functional theory
DMTA	Dynamic mechanical thermal analysis
DSC	Differential scanning calorimetry
$\varepsilon$	Extinction coefficient (absorptivity)
E or EDOT	3,4-Ethylenedioxythiophene

EA	Electron affinity
$E_B$	Electron–hole pair binding energy
$\eta_{ET}$	Energy transfer efficiency
$E_{fund}$	Fundamental energy gap
$E_g$	Energy gap
EL	Electroluminescence
$E_{opt}$	Optical energy gap
$E_{ox}$	Oxidation onset potential
$E_p^a$	Anodic peak potential
$E_p^c$	Cathodic peak potential
$E_{red}$	Reduction onset potential
$\eta_{Out}$	Emission outcoupling efficiency
$\eta_{Rec}$	Exciton formation efficiency
$\eta_{ST}$	Singlet–triplet exciton ratio
EQE or $\eta_{Ext}$	External quantum efficiency
F8BT	Poly(9,9-dioctylfluorene- <i>alt</i> -benzothiadiazole)
Fc/Fc <sup>+</sup>	Ferrocene/ferrocenium
GC/MS	Gas chromatography/mass spectrometry
GPC	Gel permeation chromatography
HOMO	Highest occupied molecular orbital
IC	Internal conversion
IDT	Indacenodithiophene
IDTT	Indacenodithieno[3,2- <i>b</i> ]thiophene
IP	Ionization potential
$i_p^a$	Anodic peak current
$i_p^c$	Cathodic peak current
IPES	Inverse photoemission spectroscopy
IQE or $\eta_{Int}$	Internal quantum efficiency
ISC	Intersystem crossing
ITO	Indium tin oxide
$J$	Current density
$J_d$	Dark current density
$J_{ph}$	Photocurrent density

$J-V$	Current density versus voltage
$J-V-R$	Current density and radiance versus voltage
$k_{ET}$	Energy transfer rate
$k_{nr}$	Nonradiative rate constant
$k_r$	Radiative rate constant
$\lambda$	Wavelength
$\lambda_{onset}$	Onset of absorption
LE	Local excited state
LEC	Light-emitting electrochemical cell
Li-Fi	Light fidelity
LUMO	Lowest unoccupied molecular orbital
MALDI-TOF	Matrix assisted laser desorption ionization-time of flight
$M_n$	Number-average molecular weight
$\mu_e$	Electron mobility
$\mu_h$	Hole mobility
NDI	Naphthalene diimide
NHE	Normal hydrogen electrode
NIR	Near-infrared
NMR	Nuclear magnetic resonance
OFET	Organic field-effect transistor
OLED	Organic light-emitting diode
OPD	Organic photodetector
OPV	Organic photovoltaic
P2TTPD	Poly[3,3'-ditetradecyl-2,2'-bithiophene-5,5'-diyl- <i>alt</i> -5-(2-ethylhexyl)-4 <i>H</i> -thieno[3,4- <i>c</i> ]pyrrole-4,6(5 <i>H</i> )-dione-1,3-diyl]
P3HT	Poly(3-hexylthiophene)
P4T	Poly[3,3'-ditetradecyl-2,2':5',2":5",2'''-quaterthiophene-5,5'''-diyl]
PC <sub>61</sub> BM	[6,6]-Phenyl-C <sub>61</sub> -butyric acid methyl ester
PD	Polydispersity index
PDI	Perylene diimide
PEDOT:PSS	Poly(3,4-ethylenedioxythiophene):poly(styrenesulfonate)
$\varphi$	Torsion angle

PIDT-2TPD	Poly[4,4,9,9-tetrakis(4-hexylphenyl)-4,9-dihydro- <i>s</i> -indaceno[1,2- <i>b</i> :5,6- <i>b'</i> ]dithiophene-2,7-diyl- <i>alt</i> -5,5'-bis(2-octyldodecyl)-4 <i>H</i> ,4' <i>H</i> -[1,1'-bithieno[3,4- <i>c</i> ]pyrrole]-4,4',6,6'(5 <i>H</i> ,5' <i>H</i> )-tetrone-3,3'-diyl]
PIDT-TPD	Poly[4,4,9,9-tetrakis(4-hexylphenyl)-4,9-dihydro- <i>s</i> -indaceno[1,2- <i>b</i> :5,6- <i>b'</i> ]dithiophene-2,7-diyl- <i>alt</i> -5-(2-ethylhexyl)-4 <i>H</i> -thieno[3,4- <i>c</i> ]pyrrole-4,6(5 <i>H</i> )-dione-1,3-diyl]
PIDTT	Poly[indacenodithieno[3,2- <i>b</i> ]thiophene-2,8-diyl]
PL	Photoluminescence
PLED	Polymer light-emitting diode
PLQY or $\Phi_f$	Photoluminescence quantum yield
Q	2,3-Diphenylquinoxaline
QF	6,7-Difluoro-2,3-diphenylquinoxaline
Redox	Reduction-oxidation
RISC	Reverse intersystem crossing
<i>R</i> (OLED/LEC)	Radiance
<i>R</i> (OPD)	Responsivity
<i>R</i> <sub>MAX</sub>	Maximum radiance
RMS	Root mean square
S	4,4-Bis(2-ethylhexyl)-4 <i>H</i> -silolo[3,2- <i>b</i> :4,5- <i>b'</i> ]dithiophene
S <sub>0</sub>	Ground state
SCLC	Space-charge-limited current
S <sub>n</sub>	Singlet excited state (n = 1, 2, etc.)
T	Thiophene
TADF	Thermally activated delayed fluorescence
TBAPF <sub>6</sub>	Tetrabutylammonium hexafluorophosphate
<i>T</i> <sub>c</sub>	Crystallization temperature
TCSPC	Time-correlated single-photon counting
$\tau_f$	Fluorescence lifetime
TEM	Transmission electron microscopy
TGA	Thermogravimetric analysis
THABF <sub>4</sub>	Tetrahexylammonium tetrafluoroborate
TIPS pentacene	6,13-Bis(triisopropylsilylethynyl)pentacene
<i>T</i> <sub>m</sub>	Melting temperature

$T_n$	Triplet excited state ( $n = 1, 2, \text{etc.}$ )
TPD	Thieno[3,4- <i>c</i> ]pyrrole-4,6-dione
TQ	2,3-Diphenyl-5,8-di(thiophen-2-yl)quinoxaline
TQF	6,7-Difluoro-2,3-diphenyl-5,8-di(thiophen-2-yl)quinoxaline
UPS	Ultraviolet photoelectron spectroscopy
VLC	Visible light communication
$V$	Voltage
$V_{ON}$	Turn-on voltage
VR	Vibrational relaxation
$X_{Ideal}$	Ideality factor



## Table of Contents

<b>Abstract</b> .....	iii
<b>List of Publications</b> .....	iv
<b>Contribution Report</b> .....	v
<b>Publications Not Included in the Thesis</b> .....	vi
<b>Nomenclature</b> .....	vii
<b>1. Introduction</b> .....	1
1.1. Optoelectronics, a History Perspective.....	1
1.2. Design Considerations, Aim and Outline of the Thesis .....	4
<b>2. Conjugated Materials and Optoelectronic Properties</b> .....	7
2.1. Definition and Design of Conjugated Molecules .....	7
2.2. Electrochemical Characterization .....	9
2.3. Characterization of the Light Absorption and Emission .....	12
<b>3. Organic Optoelectronic Devices</b> .....	19
3.1. Organic Light-Emitting Diodes .....	19
3.2. Light-Emitting Electrochemical Cells .....	20
3.3. Organic Photodetectors.....	21
<b>4. Synthesis of Conjugated Polymers and Small Molecules for NIR-OLEDs</b> .....	25
4.1. Random Copolymers Comprising BTT as the Emitter.....	26
4.1.1. Design Strategy .....	26
4.1.2. Material Synthesis and Characterization .....	26
4.1.3. Optical Properties and NIR-OLEDs Performance .....	29
4.2. BTT* Small Molecule:Polymer Blends.....	32
4.2.1. Small Molecule as the Emitter .....	32
4.2.2. Material Synthesis and Characterization .....	33
4.2.3. Optical Properties .....	36
4.2.4. NIR-OLEDs Performance .....	38
<b>5. Synthesis of Conjugated Polymers for NIR-LECs</b> .....	41
5.1. IDTT-Based Copolymer as the Single Emitter.....	41
5.1.1. Background and Motivation .....	41

5.1.2.	Polymer Design, Synthesis, and Characterization .....	42
5.1.3.	Performance of the NIR-LECs .....	46
5.2.	Random Copolymers Incorporating D–A–D Segments as the Emitter .....	49
5.2.1.	Design of the Random Copolymers .....	49
5.2.2.	Material Synthesis and Characterization .....	49
5.2.3.	Performance of the NIR-LECs .....	53
<b>6.</b>	<b>Application of Conjugated Polymers for OPDs .....</b>	<b>57</b>
6.1.	High-Speed OPDs Based on PIDT-TPD Donor Polymer .....	57
6.1.1.	Aim at High Performance .....	57
6.1.2.	Characterization of the PIDT-TPD/PCBM Blend .....	58
6.1.3.	Performance of the OPDs .....	60
6.2.	PIDT-2TPD as the Acceptor for All-PPDs .....	63
6.2.1.	The D–A–A Design Motif .....	63
6.2.2.	Characterization of the P3HT/PIDT-2TPD Blend .....	64
6.2.3.	Performance of the All-PPDs .....	66
<b>7.</b>	<b>Conclusion and Outlook .....</b>	<b>69</b>
<b>8.</b>	<b>Methods .....</b>	<b>73</b>
8.1.	Stille Coupling .....	73
8.2.	Direct Arylation .....	75
8.3.	DFT Calculation .....	76
8.4.	AFM and TEM .....	77
	<b>Acknowledgements .....</b>	<b>79</b>
	<b>Bibliography .....</b>	<b>81</b>
	<b>Appendix .....</b>	<b>95</b>

# 1. Introduction

What makes organic optoelectronics interesting is that they can be fabricated on flexible and stretchable plastic substrates,<sup>[1-3]</sup> or even on transparent cellulose paper,<sup>[4-6]</sup> using solution-based methods. This is relevant for wearable, implantable, and in vivo medical applications, such as light-mediated sensing of heart and respiration rate, blood pressure, glucose level, and oxygenation.<sup>[7-9]</sup> Organic semiconductors benefit from being mechanically conformable, like many plastics, but they are also soluble and this can be exploited in the slot-die coating, inkjet, or 3D printing of optoelectronics, which are thin, light-weight, and semi/fully transparent.<sup>[10-14]</sup> Scalable low-cost processing of such devices in multiple shapes and sizes from nanometer scale up to large-area screens and displays is attractive for a wide range of applications, some of which are introduced in the following section.

## 1.1. Optoelectronics, a History Perspective

The story of electroluminescent diodes dates back to the 1960s and different GaP, GaAsP, and GaAs semiconducting crystals, which were prepared at high temperatures, and which devices were driven at extremely high current densities up to the order of  $10^4$  A/cm<sup>2</sup>.<sup>[15-19]</sup> This meant that the lifetime of the diodes was short but, interestingly, they emitted light from the visible to the near-infrared (NIR, defined as wavelengths  $\lambda > 700$  nm) spectral range. Thereafter, first organic electroluminescent diodes were based on anthracene as a visible blue emitter,<sup>[20,21]</sup> and in 1987 Tang and VanSlyke<sup>[22]</sup> reported a novel light-emitting device, which is now known as an organic light-emitting diode (OLED). This early research has inspired the development of highly sophisticated molecules that emit light in different colors over the visible spectrum, and has enabled the commercialization of OLED displays, TV screens, and lighting applications. However, the NIR range has remained far less developed among the organic emitters, and one reason for that is the challenge for materials design set by the intrinsically decreasing emission efficiency when moving from shorter to longer wavelengths, in other words, when redshifting the emission. This issue will be discussed in more detail later in this thesis. The motivation for the design of functional NIR emitters is that their applications can be extended from (night-vision) displays to security,<sup>[23]</sup> light fidelity (Li-Fi) all-optical communication networks,<sup>[24-27]</sup> photodynamic/photothermal therapy,<sup>[28-30]</sup> and biosensing.<sup>[31,32]</sup> The 650–950 nm range is of particular interest for biomedical applications due to the semitransparency of skin and tissue to the light at this spectral region.<sup>[33]</sup>

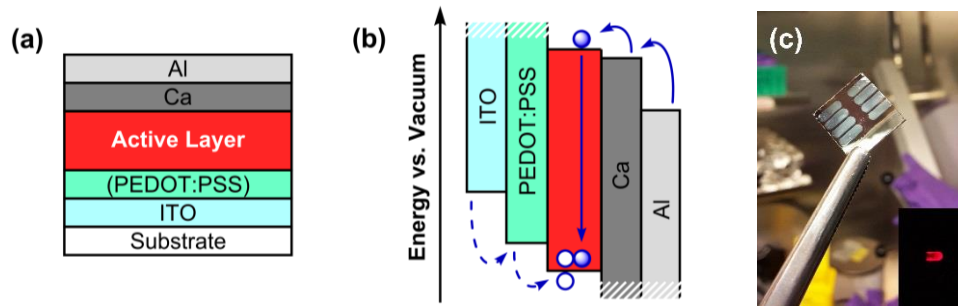


**Figure 1.1.** (a) Illustration of OLED device architecture. (b) Schematic energy diagram for the injection and recombination of electrons (filled circles) and holes (empty circles). (c) Photograph of a test device comprising eight OLEDs (showing the Al top contacts), as fabricated at the facilities of Prof. Cacialli at UCL. The inset in part c shows the emission from one of the OLEDs, as photographed from the bottom of the device in dark.

In an OLED, electrons are injected from the cathode and holes are injected from the anode, and the recombination and light emission occurs at the active layer, as illustrated in Figure 1.1. In the literature, polymer-based OLEDs are often differentiated with the naming polymer light-emitting diode (PLED), but since the general working mechanism is the same in both devices, they are simply referred to as OLEDs in this thesis. A typical OLED device is fabricated on a transparent substrate, which is either glass or plastic, comprising indium tin oxide (ITO) as the anode and poly(3,4-ethylenedioxythiophene):poly(styrenesulfonate) (PEDOT:PSS) as the hole injection layer. Ca/Al are deposited on top of the active layer as the cathode. Additional electron and hole blocking layers can be used to balance the charge transport in the device and thereby improve the charge recombination efficiency in the active layer.<sup>[34-37]</sup>

In 1995, Heeger et al.<sup>[38-40]</sup> included an additional electrolyte salt in a polymer-based active layer in a device called light-emitting electrochemical cell (LEC). Since then, LECs have been under constant development to obtain good long-term stability,<sup>[41-45]</sup> which has become a key feature that distinguishes LECs from other light-emitting devices. An LEC differs from OLED in that the electrolyte forms a p–n junction doping structure upon turning on the device, that is, in the electric field the cationic species drift toward the cathode forming a n-type doped region and the anionic species drift toward the anode forming a p-type doped region. The p–n junction contains the undoped electron–hole recombination zone, which is ideally formed in the middle of the active layer (Figure 1.2).<sup>[46,47]</sup> In a well-functioning LEC, the p–n junction ensures an efficient charge recombination without additional interlayers or low-work function

cathode metals, but the electrochemical stability of the active layer material plays an important role in the device performance, as discussed later in this thesis.

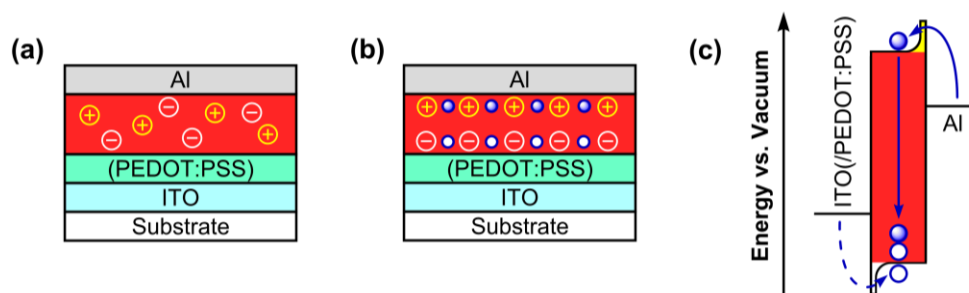


**Figure 1.2.** (a) LEC device architecture. (b,c) Schematic representation of the formation of the p–n junction doping structure during the initial turn-on process, and schematic energy level diagram illustrating the injection of electrons (filled circles) and holes (empty circles) through the energy barriers of the n-type doped (yellow) and p-type doped (white) regions.

The evolution of photoresponse devices is connected to the electroluminescent devices, and the early versions of photodetectors were based on similar Ga, Ge, and Si semiconductors.<sup>[48-51]</sup> The devices converted incident light into free charge carriers under an external reverse bias voltage, and thus the photocurrent was strongly dependent on the electric field. Introduction of the concept of heterojunction, based on two semiconductor materials (Ge/GaAs, Si/GaP, GaAs/SiOx, etc.) in a crystalline double-layer, allowed better control of the band structure and thereby more efficient separation of charge carriers at the interface of the two materials.<sup>[52-54]</sup> An organic-inorganic heterojunction,<sup>[55,56]</sup> and the development of modern bulk heterojunction (BHJ), based on fully organic semiconducting electron donor and electron acceptor, increased the interfacial area and charge separation efficiency in the photoactive layer,<sup>[57-59]</sup> as illustrated in Figure 1.3. Performance of organic photodetectors (OPDs) will be discussed in more detail later in this thesis. Although the charge separation was efficient at the BHJ donor–acceptor interface, charge transport was somewhat limited compared to the above mentioned crystalline semiconductors, mainly because of the disordered morphology of the BHJ. This issue has been improved with a morphological control and a range of donor and acceptor materials available today.<sup>[60-65]</sup> In the current view, one of the main advantages of OPDs is the possibility to tune their spectral response with the chemical structure of the photoactive layer, and thereby target different applications, such as visible light communication (VLC),<sup>[66]</sup> night vision,<sup>[67,68]</sup> photo and video imaging,<sup>[69-71]</sup> and biosensing.<sup>[72,73]</sup>

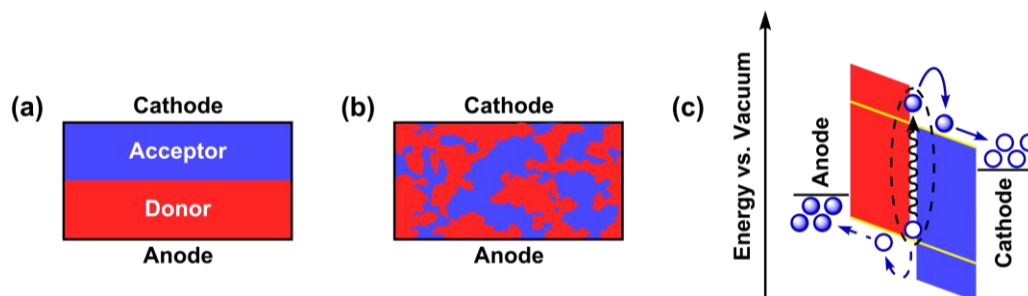


**Figure 1.3.** Schematic representation of an OPD comprising (a) heterojunction and (b) bulk heterojunction photoactive layer, and (c) the corresponding device operation at reverse bias: formation of the electron–hole pair (black dashed circle) via incident light absorption at the donor–acceptor interface (black wavy arrow) and separation of the electrons (filled circles) and holes (empty circles) into free charge carriers.

## 1.2. Design Considerations, Aim and Outline of the Thesis

Given the strong motivation for the use of solution-processable active layer materials in the optoelectronic devices, this thesis focuses solely on the synthesis of conjugated polymers and small molecules and their application for NIR-OLEDs, NIR-LECs, and OPDs for visible (red) detection. For NIR-OLEDs, the general approach is to use a wide energy gap polymer as the host matrix and a low energy gap molecule as the NIR emitter, which is either blended with the polymer or incorporated into the polymer backbone. Both approaches are to aim at high emission efficiency. However, the commercial polymer matrices are usually not ideal for NIR-OLEDs because of the mismatch of their energy levels and poor spectral overlap with the NIR molecules. The former is important for charge trapping at the NIR emitting sites and exciton formation specifically at their locations, whereas the latter is related to the efficiency of energy transfer from the host polymer to the NIR emitter. An interplay of these two mechanisms is ultimately connected to the NIR emission efficiency. For a functional NIR-OLED, one needs a host polymer that exhibits (i) good charge transport properties for low-voltage operation, (ii) suitable frontier orbital energy levels for charge injection selectively at the NIR molecule, (iii) high fluorescence efficiency, also in the solid state, and (iv) emission wavelength that overlaps with the absorption of the NIR molecule to facilitate an efficient energy transfer. With these criteria in hand, the remaining questions are:

- What is the most feasible approach to mix the NIR emitter into the polymer matrix, that is, by blending or copolymerization?

- How much does the selection of host polymer impact the NIR performance, and are there true alternatives for the well-known commercial polymer matrices?

For the application of polymeric NIR emitters for LECs, it is of great importance to study if conjugated polymers can improve the commonly poor NIR-LEC performance via (i) good electrochemical stability, (ii) balanced electrochemical p-type and n-typed doping capacities and (iii) compatibility with the electrolyte salt for a well-behaving p–n junction formation, and (iv) good long-term device stability, also in ambient air. Thus, two questions arise:

- Can the NIR light-intensity be improved with the polymer approach, in comparison to the previously reported materials, by fulfilling the above form-factor requirements?
- What is the optimal type of polymer emitter, that is, should the active layer consist of a single NIR-emissive polymer or can the inclusion of a wide-gap host and a low-gap NIR emitter deliver better performance in the strongly doped driving conditions?

The applications of emissive polymers are not limited to light-emitting devices but they can be also useful for light-harvesting applications, such as OPDs in this thesis. Well-functioning polymer emitters commonly exhibit good electron- or hole-dominated mobilities or ambipolar charge transport properties. Therefore, they can be used either as electron donor or electron acceptor materials in a conversion of light into electrons and holes in the BHJ, and extraction of the charge carriers in an electric field. Considering applications for example in imaging and light communication, an OPD should ideally deliver a low dark current, high detectivity, and high frequency response, in other words, detect light from the noise even at low intensities and simultaneously operate at high speeds. A question arises:

- What type of emissive polymer can be used as an active material to fulfill the OPD device requirements – is an efficient emitter also a strong absorber?

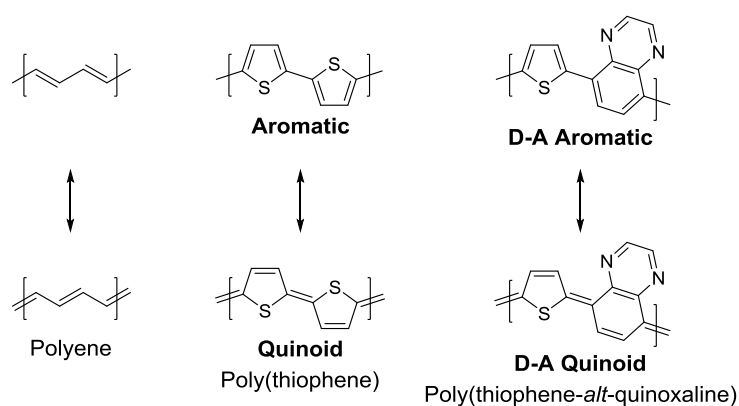
The general considerations for the materials design and synthesis in this thesis are covered in Chapter 2. The same chapter also introduces the critical characteristics that are studied and optimized for the materials. These are the energy, wavelength, and efficiency of the absorption and emission processes, the reversibility and stability of the electrochemical oxidation (p-type doping) and reduction (n-type doping) processes, and the frontier orbital energy levels. The different device parameters are introduced in Chapter 3, in consideration of the requirements from a materials design perspective. Chapter 4 brings the preceding chapters into the context of NIR emitters and summarizes the study on NIR-OLEDs and how the device performance

can be improved significantly with materials design, covering papers I and II. Introduction of polymeric NIR emitters for LEC devices in Chapter 5 improves the general understanding of electrochemical doping in the active layer, ultimately resulting in an intense NIR emission, covering papers III and IV. Chapter 6 demonstrates that light-emitting polymers can be used for the fabrication of highly functional OPDs, whose performance is comparable to that of the conventional inorganic photodetectors. The efficiency of charge carrier separation and charge extraction both play an important role in the device performance. These processes are studied with polymer design and morphological control, covering papers V and VI. Overall, solution-processing allows relatively easy and low-cost device fabrication procedure, but poses special requirements for the materials design, both physical and mechanical, which are discussed and effectively fulfilled in this thesis.

## 2. Conjugated Materials and Optoelectronic Properties

This chapter gives a brief overview of different types of conjugated molecules, their structural design, electrochemical properties, and light absorption and emission characteristics. These properties are relevant in that they can be tuned with changes in the chemical structure, thereby defining the performance of the materials in different electronic and photonic applications.

### 2.1. Definition and Design of Conjugated Molecules



**Scheme 2.1.** Chemical and resonance structures of different types of conjugated polymers.

As studied in organic chemistry, in a molecule with at least two adjacent  $sp^2$  hybridized carbon atoms the  $sp^2$  hybrid orbitals form a single ( $\sigma$ ) bond, whereas the overlap of the non-hybrid p-orbitals contribute to a double ( $\pi$ ) bond between the carbon atoms.<sup>[74]</sup> In an extended molecular structure, the double bond electrons can diffuse (delocalize) along the neighboring p-orbitals, which is referred to as a conjugated system. Scheme 2.1 shows a simple conjugated polymer structure, a polyene, which consists of an undefined number of alternating single bonds and double bonds. Since the  $\pi$ -electrons are shared along the entire polymer backbone, the double bonds can “flip” freely between the carbon atoms, and this is drawn as a resonance between the two structures. Both of these mesomeric forms are energetically identical.<sup>[75]</sup> The polymer can also consist of a series of cyclic conjugated (aromatic) carbon rings, or other than carbon atoms containing heteroaromatic structures, such as the sulfur atom containing thiophenes in poly(thiophene). The thiophene rings are connected by  $\sigma$ -bonds to obey the rule of alternating double bonds. Different from the planar and rigid  $\pi$ -bonds, the  $\sigma$ -bonds can rotate freely along their axis. This allows certain freedom for the polymer backbone to twist between the repeating thiophene units. In the case of poly(thiophene), the resonance results in the double bonds being flipped between the thiophenes, known as a quinoid structure, which restricts the molecular

motion and planarizes the polymer backbone.<sup>[76,77]</sup> This added stability means that the two resonance structures (aromatic and quinoid) are no longer energetically comparable.

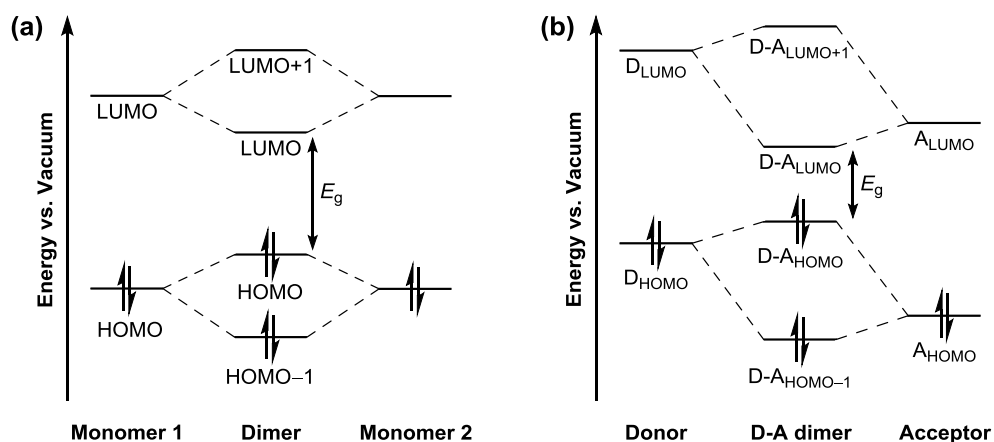


**Figure 2.1.** Energy level diagram of (a) an imaginary dimer comprising two identical monomers and (b) a D–A structured dimer comprising a donor and an acceptor monomer.

In a conjugated molecule, say, a dimer that comprises two monomers (Figure 2.1a), the  $\pi$ -electrons of the molecular orbitals of both monomers are shared in the new molecular orbitals of the dimer. Depending on the spatial overlap of the wavefunctions of the non-hybrid p-orbitals (the ones that are involved in the  $\pi$ -bond of the two monomers), they can either form a low-energy bonding molecular orbital or a high-energy antibonding molecular orbital.<sup>[74]</sup> The  $\pi$ -electrons from both monomers fill the lower-energy (bonding,  $\pi$ ) molecular orbitals, leaving the higher-energy (antibonding,  $\pi^*$ ) molecular orbitals unoccupied.<sup>[76,78]</sup> Thus, the naming highest occupied molecular orbital (HOMO) and lowest unoccupied molecular orbital (LUMO) and, accordingly, HOMO–1 and LUMO+1, to describe the electron occupation and relative energy of the orbitals. For organic semiconductors, HOMO and LUMO are the two most relevant orbitals, since their energy positioning (relative to the vacuum level) define the energy that is needed to remove or add an electron at the molecule, respectively, and their separation, the energy gap ( $E_g$ ), is also related to the energies of the optical transitions.

By means of materials design, the  $E_g$  can be decreased by stabilizing the quinoid structure over the aromatic form,<sup>[79,80]</sup> but introduction of different electron donor and electron acceptor monomers is an even more versatile approach.<sup>[75,81]</sup> A donor can be described as a molecule with high-lying HOMO and LUMO energy levels, whereas an acceptor exhibits low-lying energy levels, as illustrated in Figure 2.1b.<sup>[82]</sup> Covalent bonding of these two monomers results in the  $\pi$  and  $\pi^*$  orbitals of the donor–acceptor (D–A) structured dimer being shifted in energy,

given the contribution from two differential monomers. Importantly, the selection of the donor and acceptor (and their corresponding energy levels) determine the HOMO and LUMO levels of the D–A dimer, effectively decreasing its  $E_g$  in comparison to the example in Figure 2.1a. The D–A approach<sup>[83]</sup> and its multiple variations, such as D–A–A, D–A<sub>1</sub>–D–A<sub>2</sub>, D–A–D, A–D–A, and so on,<sup>[84–89]</sup> allow almost unlimited possibilities not only for the tuning of the HOMO and LUMO and the  $E_g$  values, but also for changing the electrochemical and optical properties of the molecule. The conjugation length is another factor that affects the orbital energies. The  $E_g$  can be systematically decreased by extending the conjugation, that is, by adding more of the energetically split  $\pi$  and  $\pi^*$  orbitals, which result in the HOMO and LUMO approaching each other.<sup>[90]</sup> Although this is effective only to a certain extent,<sup>[91–93]</sup> the  $E_g$  is usually smaller for polymers than for similarly structured small molecules (monomers, dimers, etc.).<sup>[94–97]</sup>

## 2.2. Electrochemical Characterization

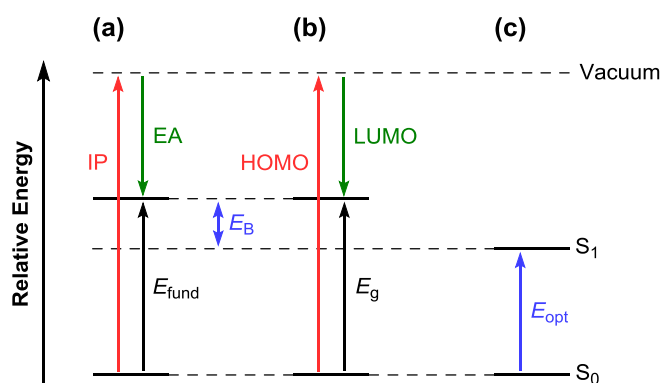


**Figure 2.2.** Schematic representation of (a) the fundamental energy levels, and (b) the electrochemically and (c) optically accessible energy levels of an imaginary molecule.

The IUPAC definition for  $E_g$  is “the energy difference between the bottom of the conduction band and the top of the valence band in a semiconductor”,<sup>[98]</sup> which describes the conventional inorganic semiconductor crystals. In the case of conjugated molecules, this can be rephrased as the difference in energy needed to remove an electron from the HOMO in gas phase, the vertical ionization potential (IP), and the energy gained by adding an electron to the LUMO in gas phase, the vertical electron affinity (EA).<sup>[99,100]</sup> These transitions are illustrated in Figure 2.2a. The fundamental energy gap ( $E_{\text{fund}}$ ) between the IP and EA can be estimated via density-functional theory (DFT) calculations,<sup>[101,102]</sup> albeit with a great deal of approximations,<sup>[103–106]</sup> or measured experimentally with ultraviolet photoelectron spectroscopy (UPS) and inverse photoemission spectroscopy (IPES) techniques.<sup>[107–109]</sup> However, in the solid state, which is

the state of interest for organic semiconductors, differential molecular orientations (disorder) and intermolecular interactions ( $\pi$ - $\pi$  stacking and polarization)<sup>[100]</sup> both influence the overall energy structure of the material. Therefore, the measured values (in the solid state) may be considerably different from the  $E_{\text{fund}}$ .

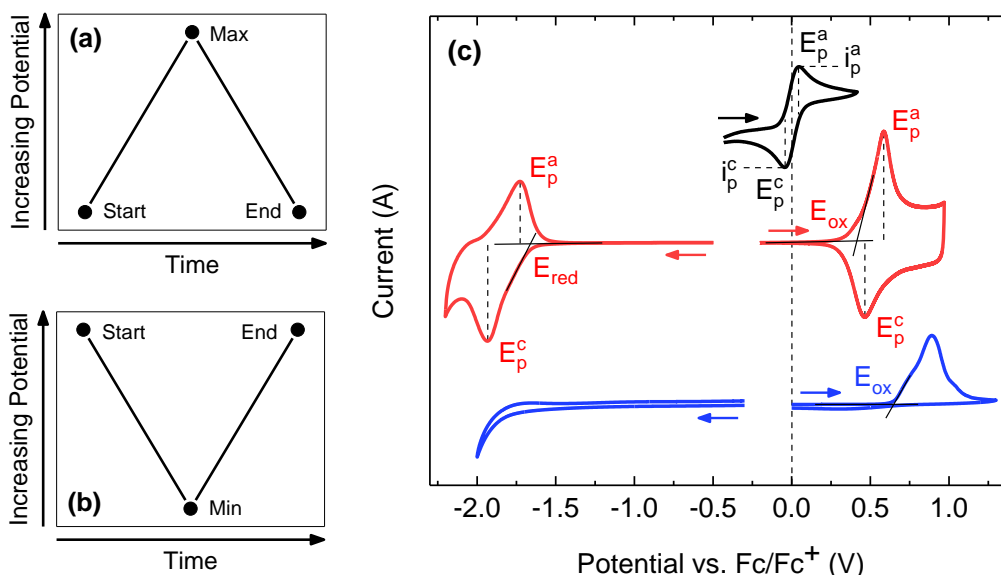


**Figure 2.3.** Linear (a) forward and (b) reverse potential scans. (c) CV traces of a reversible  $\text{Fc}/\text{Fc}^+$  redox couple (black line), a quasi-reversible polymer (red line), and an irreversible polymer (blue line), all at a scan rate of 100 mV/s. Determination of the oxidation ( $E_{\text{ox}}$ ) and reduction ( $E_{\text{red}}$ ) onset potentials, the anodic ( $E_{\text{p}}^{\text{a}}$ ) and cathodic ( $E_{\text{p}}^{\text{c}}$ ) peak potentials, and the anodic ( $i_{\text{p}}^{\text{a}}$ ) and cathodic ( $i_{\text{p}}^{\text{c}}$ ) peak currents. The arrows indicate the scan direction.

Cyclic voltammetry (CV) is a practical method for the estimation of the HOMO and LUMO energy levels via electrochemical doping, that is, by removing an electron from the molecule (oxidation, p-type doping) or by adding an electron to the molecule (reduction, n-type doping), respectively.<sup>[110-112]</sup> These electron transfer reactions can be studied by depositing the material on a working electrode surface as a solid-state thin film, and then immersing it in a supporting electrolyte solution (or alternatively dissolving the material in the electrolyte solution). A 0.1 M solution of tetrabutylammonium hexafluorophosphate ( $\text{TBAPF}_6$ ) in anhydrous acetonitrile is a commonly used electrolyte.<sup>[113]</sup> Conveniently, polar acetonitrile does not usually dissolve the films of conjugated polymers and small molecules. The CV data is collected by applying a positive (forward, Figure 2.3a) or negative (reverse, Figure 2.3b) linear potential scan to the electrode. At a certain pre-set voltage, the scan is switched to an opposite direction at the same

scan rate. An anodic wave appears upon oxidation of the material on the forward scan, and a cathodic wave appears during the reverse scan, as illustrated in Figure 2.3c.<sup>[114]</sup>

For a redox couple exhibiting fast single electron transfer, referred to as a reversible couple (Figure 2.3c, black line), (i) separation of the anodic ( $E_p^a$ ) and cathodic ( $E_p^c$ ) peak potentials, i.e.,  $\Delta E_p = |E_p^a - E_p^c|$ , is 57 mV, (ii) the anodic ( $i_p^a$ ) and cathodic ( $i_p^c$ ) peak currents are approximately the same, thus  $|i_p^a/i_p^c| = 1$ , (iii) the position of the peak potentials ( $E_p^a$ ,  $E_p^c$ ) remain constant regardless the scan rate, but (iv) the peak currents ( $i_p^a$ ,  $i_p^c$ ) are proportional to the square root of the scan rate,<sup>[115]</sup> i.e., they increase with increasing scan rate.<sup>[114,116]</sup> For a quasi-reversible electrochemical reaction (Figure 2.3c, red line), the oxidation and reduction are still relatively fast, but a certain energy barrier for the electron transfer requires a higher applied potential for the oxidation/reduction to occur. Therefore, the value of  $\Delta E_p$  becomes larger than 57 mV, changing as a function of the scan rate, and the peak currents are no longer proportional to the square root of the scan rate. For a slow or unstable electrochemical reaction, referred to as an irreversible redox couple (Figure 2.3c, blue line), CV trace lacks the reverse reaction completely (that is, during the scan at the opposite direction of the forward or reverse scan).<sup>[117]</sup> Chemical reversibility refers to stability of the material during oxidation/reduction, and whether or not it can be re-reduced/re-oxidized.<sup>[118]</sup>

It is important to note that the oxidation and reduction of a conjugated polymer (or small molecule) at the electrode surface leads to conformational reorganization,<sup>[112]</sup> such as changes between the aromatic and quinoid resonance structures.<sup>[80]</sup> Therefore, the redox properties are characterized from the oxidation ( $E_{ox}$ ) and reduction ( $E_{red}$ ) onset potentials (see Figure 2.3c).  $E_{ox}$  describes the lowest energy needed to remove an electron from the HOMO,<sup>[119]</sup> and  $E_{red}$  refers to the energy of adding an electron to the LUMO,<sup>[120]</sup> which are observed as increasing anodic and cathodic currents in the CV traces, respectively. The HOMO and LUMO can be assessed by measuring the onset potentials. However, the CV method does not provide direct indication of their energy in the vacuum scale (as in the case of IP and EA). It necessitates the use of a reference redox couple with a known, standard potential.  $[\text{Fe}(\text{Cp})_2]/[\text{Fe}(\text{Cp})_2]^+$  couple, known as ferrocene/ferrocenium ( $\text{Fc}/\text{Fc}^+$ ) couple, is a common standard with a redox potential of 0.63 V against the normal hydrogen electrode (NHE) in acetonitrile at 25 °C,<sup>[121]</sup> and the NHE in turn has an electrode potential of -4.5 V in the vacuum scale.<sup>[115]</sup> This allows an indirect evaluation of the HOMO and LUMO energies by measuring the  $E_{ox}$  and  $E_{red}$  versus the  $\text{Fc}/\text{Fc}^+$  redox couple at 0 V, respectively, and by using the following equations:

$$E_{\text{HOMO}} = -(E_{\text{ox}} + 5.13) \text{ (eV)} \quad (2.1)$$

$$E_{\text{LUMO}} = -(E_{\text{red}} + 5.13) \text{ (eV)} \quad (2.2)$$

With these approximations, it is evident that the electrochemically accessible values of the HOMO and LUMO energies in the vacuum scale, or the  $E_g$ , are not directly comparable to the fundamental IP and EA in the gas phase, nor to the  $E_{\text{fund}}$ . However, they do give an excellent indication of the p-type and n-type doping processes (i.e., hole and electron injection), their energies, and the electrochemical reversibility and stability, which are highly relevant for the performance of the materials in the optoelectronic devices.

### 2.3. Characterization of the Light Absorption and Emission

The characterization techniques in the previous section did not take into account the electron–hole pair binding energy ( $E_B$ ).<sup>[122]</sup> Upon absorption of a photon (i.e., excitation) an electron–hole pair (i.e., exciton) is formed.  $E_B$  describes the additional energy required to overcome the attractive Coulomb force and dissociate the electron and hole into free charge carriers.<sup>[123,124]</sup> Thus, the lowest accessible vertical excitation, the optical energy gap ( $E_{\text{opt}}$ ), is generally lower than the electrochemically measured  $E_g$  (or the  $E_{\text{fund}}$ ), as schematically illustrated in Figure 2.2c.<sup>[100,125]</sup>  $E_{\text{opt}}$  is obtained experimentally from the low-energy absorption onset ( $\lambda_{\text{onset}}$ ) of the material, either in solution or solid-state thin film, given the Planck relation:<sup>[126]</sup>

$$E_{\text{opt}} = h\nu = hc/\lambda \approx 1240/\lambda_{\text{onset}} \text{ (eV)} \quad (2.3)$$

where  $h$  is Planck constant ( $6.626 \times 10^{-34}$  J s, or  $4.135 \times 10^{-15}$  eV s),<sup>[127]</sup>  $\nu$  is the frequency,  $c$  is the speed of light in vacuum ( $2.998 \times 10^8$  m/s), and  $\lambda$  is the wavelength. Estimation of  $\lambda_{\text{onset}}$  in nanometers ( $10^{-9}$  m) thus relates to the  $E_{\text{opt}}$  in eV, as shown in Figure 2.4.<sup>[128]</sup> Interpretation of the rest of the absorption spectrum is less straightforward. Where  $E_{\text{opt}}$  describes the vertical excitation from the ground state ( $S_0$ ) to the lowest-energy singlet excited state ( $S_1$ ), the overall absorption of conjugated molecules is a sum of transitions from the  $S_0$  state to the different electrically and vibrationally excited ( $S_1$ ,  $S_2$ , etc.) states.<sup>[74,126,129]</sup> This leads to a broadening of the absorption band, as shown in Figure 2.4 and further schematically illustrated in Figure 2.5. The energy differences between the vibrational levels (Figure 2.5a, grey lines) are, in general, smaller than those of the electronic levels (Figure 2.5a, black lines). Therefore, the classical electronic transitions ( $S_0 \rightarrow S_1$ ,  $S_0 \rightarrow S_2$ , etc.) require the high energy of UV-visible

photons, or that of the injected electrons, while the vibrational transitions can be induced with low-energy infrared, or even NIR photons.<sup>[74]</sup>

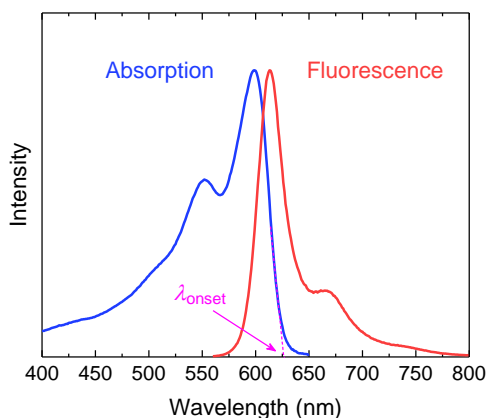


**Figure 2.4.** Absorption and PL spectra of an imaginary conjugated polymer.

Absorption of light by the molecule can be assessed with Lambert–Beer law, which states that the light passing through the sample is diminished by three physical factors: (i) the amount of absorbing material that the light must travel through, i.e., its concentration, (ii) the distance the light must travel through the sample, i.e., the path length, and (iii) the probability that the photon of a given energy is absorbed, i.e., the absorption coefficient of the sample. Then, if an incident light of an intensity of  $I_0$  passes through the sample, a certain (lower) intensity of  $I_t$  is transmitted through. The law assumes that the proportion of light absorbed by the molecule is independent of the magnitude of  $I_0$ . Thus, if the sample (solution or thin film) is homogeneous, the probability of light absorption is linearly dependent on the intensity, and each successive layer of the sample absorbs an equal fraction of light across a finite length scale. This means that the magnitude of  $I_t$  decreases exponentially with increasing path length, or with increasing concentration (for solution). The relation of  $I_0$  to  $I_t$  is defined as absorbance (Abs, or  $A_\lambda$ ):<sup>[74,126]</sup>

$$A_\lambda = \log(I_0/I_t) = \varepsilon c l \quad (2.4)$$

where  $\varepsilon$  is the molar absorptivity (i.e., extinction coefficient) with units  $\text{M}^{-1} \text{cm}^{-1}$  (or  $\text{L g}^{-1} \text{cm}^{-1}$ ),  $c$  is the solution concentration in M (or g/L), and  $l$  is the path length in centimeters. The constant  $\varepsilon$  depends on the material, describing its ability to absorb light. The absorption spectra of conjugated molecules are usually measured over a wavelength range, as in Figure 2.4, either in a solution of low concentration (in a quartz cuvette with 1 cm path length) or as a thin film with thickness of  $\sim 100 \text{ nm}$ .<sup>[130-132]</sup> In the latter case, Equation (2.4) becomes:<sup>[133]</sup>

$$A_\lambda = \alpha l \quad (2.5)$$

where  $\alpha$  describes the absorption coefficient of the material in thin film, with a unit  $\text{cm}^{-1}$ , and  $l$  is the film thickness (i.e., path length) in centimeters. The absolute value of  $\alpha$  (or  $\epsilon$ ) depends strongly on the wavelength, and is therefore reported as a plot versus wavelength, or as a value connected to a specific wavelength (typically that of the absorption peak maximum).

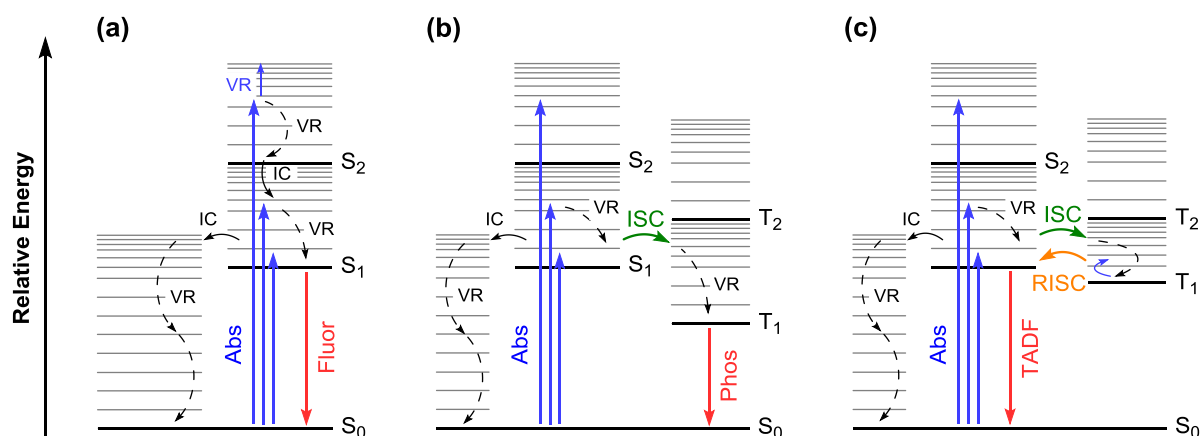


**Figure 2.5.** Jablonski diagram of an imaginary molecule, illustrating the low-lying energy levels involved in the excitation of an electron via absorption of a photon, some nonradiative relaxation pathways (black arrows), and radiative relaxation as (a) fluorescence, (b) phosphorescence, and (c) thermally activated delayed fluorescence.

Fluorescence spectroscopy measures the emitted photons in relation to the absorbed ones, which emission is generally referred to as photoluminescence (PL). Conjugated molecules can exploit the energy of excited electrons as radiative relaxation back to the S<sub>0</sub> state (apart from the specific case of exciton dissociation in the BHJ, see Chapter 1). Figure 2.5a represents a conjugated molecule, whose S<sub>0</sub> state electron is optically excited to the low-energy S<sub>n</sub> (where  $n = 1, 2$ , etc.) electronic state or vibronic state. Countless possibilities of internal conversion (IC) and vibrational relaxation (VR) to the lower energy levels ultimately lead to a relaxation from the S<sub>1</sub> state to different electronic and vibronic S<sub>0</sub> state energy levels. The latter process is termed fluorescence. Similarly to the absorption process discussed above, the combination of different energy transitions to the S<sub>0</sub> state leads to a broadening of the emission band (see Figure 2.4). Various nonradiative decay processes can take place, such as vibronic coupling of the S<sub>0</sub> and S<sub>1</sub> states, as schematically illustrated on the left side of Figure 2.5a, or intersystem crossing (ISC) to a lower-lying triplet excited (T<sub>n</sub>) state and further nonradiative relaxation to the S<sub>0</sub> state (not included in Figure 2.5a). These undesired transitions decrease the fluorescence efficiency, which is defined as photoluminescence quantum yield (PLQY, or  $\Phi_f$ ):<sup>[126,129,134]</sup>

$$\Phi_f = k_r / (k_r + k_{nr}) = N_{\text{emitted}} / N_{\text{absorbed}} \quad (2.6)$$

where the  $k_r$  is the radiative rate constant, and  $k_{nr}$  is the nonradiative rate constant describing the above mentioned dark decay processes.  $\Phi_f$  can be obtained experimentally by measuring the relative number of the absorbed and emitted photons,  $N_{\text{absorbed}}$  and  $N_{\text{emitted}}$ , respectively, in comparison to a dye with a known, standard  $\Phi_f$ ,<sup>[135]</sup> while the absolute values of  $N_{\text{absorbed}}$  and  $N_{\text{emitted}}$  can be measured with an integrating sphere.<sup>[136,137]</sup> The latter method is desired due to its accuracy and applicability for both solution and thin film samples.

The average time a molecule remains excited before spontaneous emission via relaxation from the  $S_1$  state to the  $S_0$  state is termed fluorescence lifetime ( $\tau_f$ ):<sup>[129]</sup>

$$\tau_f = 1 / (k_r + k_{nr}) \quad (2.7)$$

which is typically in the order of  $10^{-9}$  s for fluorescent molecules (for comparison,  $S_n \rightarrow S_1$  IC and VR processes are even faster, in the order of  $10^{-10}$ – $10^{-14}$  s).<sup>[126,134]</sup>  $\tau_f$  can be measured experimentally with a time-correlated single-photon counting (TCSPC) technique.<sup>[138]</sup> Thus,  $k_r$  and  $k_{nr}$  can be derived from Equations (2.6) and (2.7) as following:

$$k_r = \Phi_f (k_r + k_{nr}) = \Phi_f (1/\tau_f) = \Phi_f / \tau_f \quad (2.8)$$

$$k_{nr} = 1/\tau_f - k_r \quad (2.9)$$

which allows a direct evaluation of the two competing processes in a fluorophore.

In further discussion of optical excitation and emission processes, it is worth taking a closer look into the electronic spin states. An electron can be described as having an intrinsic angular momentum, a spin quantum number of  $s = 1/2$ , with the notion that it does not behave like a negatively charged particle rotating around its axis. Instead, the alignment of the spin (a vector along a reference direction, an arbitrarily chosen axis) is identified as a spin magnetic quantum number  $m_s = +1/2$  or  $-1/2$ .<sup>[74,139]</sup> These two possible values of  $m_s$  are commonly represented as spin-up, or  $\uparrow$ , and spin-down, or  $\downarrow$ , respectively, as for example in Figure 2.1. If there are multiple electrons to be taken into account, the total spin angular momentum quantum number (the resultant spin) is given by  $S = s_1 + s_2, s_1 + s_2 - 1, \dots, |s_1 - s_2|$ , where  $s_i$  is the spin of  $i$ th electron. Considering two coupled electrons in a molecule,  $S$  can be either 1 or 0, and there are four possibilities for the arrangement of their spin configurations, given by the multiplicity  $M = 2S + 1$ , one corresponding to singlet state ( $M = 1$ ) and three corresponding to triplet state ( $M = 3$ ).<sup>[139,140]</sup> In fact, multiplicity tells the number of allowed values of the total spin

magnetic quantum number  $M_s = S, S - 1, \dots, -S$  for a given value of  $S$ , in other words, the possible orientations (spin vectors in space) that the total spin can adopt.<sup>[74,101,139]</sup>

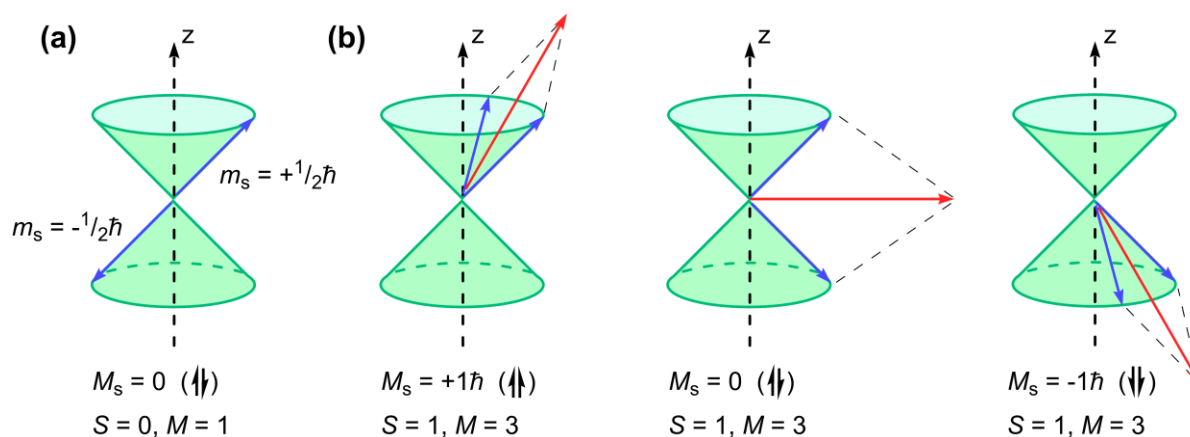


**Figure 2.6.** Schematic representation of the electron spin ( $m_s = \pm 1/2\hbar$ ). Individual electron spins are shown as vectors (blue arrows) lying in cones along the z-axis and the total spin is shown as a vector (red arrow) lying between two coupled electrons. (a) A singlet has zero total spin angular momentum ( $S = 0$ ): whenever one spin vector lies on its cone, the other points to an opposite direction, cancelling the overall spin. (b) A triplet has three ways of achieving a nonzero total spin angular momentum ( $S = 1$ ): the spin vectors lie either in the same cone ( $M_s = \pm 1\hbar$ ) or in opposite cones but in phase ( $M_s = 0$  along the z-axis).

In Figure 2.6, the individual spins  $m_s$  and their resultant  $M_s$  are shown as vectors precessing about an arbitrarily chosen z-axis. In the case of  $S = 0, M = 1$ , there is only one possible spin orientation,  $M_s = 0$ , thus the naming singlet: the electron spins are paired (opposite/antiparallel) and there are no net spin. When  $S = 1, M = 3$ , there are three possible spin orientations,  $M_s = +1, 0$ , or  $-1$ , and thus the naming triplet: the two electrons are unpaired (parallel/in phase) and the net spin  $S = 1$  in all cases.<sup>[74,101,139]</sup>

The above description gives an intrinsic singlet–triplet exciton formation ratio ( $\eta_{ST}$ ), often termed “spin statistics”,<sup>[74,141,142]</sup> since the same spin vectors apply to the excited states.<sup>[140,143]</sup> However, virtually all conjugated molecules exhibit a singlet ground state configuration, i.e., all electrons are paired, and absorption of a photon results in excitation from the  $S_0$  state to the corresponding  $S_n$  state with no change in the electron spin.<sup>[74,139]</sup> This is known as spin-allowed transition. The ISC process allows the occupation of the triplet excited  $T_n$  states, and ultimately the fraction of excitons located at the singlet state is 25%, while 75% of the excitons are formed as triplets. Relaxation from excited  $T_1$  state to  $S_0$  ground state requires the spin of the electron

to flip or rephase, and is therefore spin-forbidden.<sup>[74,139]</sup> Moreover,  $k_r$  for the  $T_1 \rightarrow S_0$  transition is relatively low, in the order of  $10^1$ – $10^3$   $s^{-1}$ , whereas  $k_{nr}$  for the triplet exciton is significantly higher, typically in the range of  $10^5$ – $10^6$   $s^{-1}$ .<sup>[126,144-146]</sup> This means that the nonradiative decay dominates the triplet state, i.e., the triplet excitons are dark, thereby intrinsically limiting the emission of the fluorescent molecules to the radiative  $S_1 \rightarrow S_0$  transition. Despite the fact that  $\eta_{ST}$  is given by default, a low  $k_{nr}$  (via assumed, slow  $S_1 \rightarrow S_0$  IC and  $S_n \rightarrow T_n$  ISC processes) and a high  $k_r$  (via fast, radiative  $S_1 \rightarrow S_0$  relaxation) can improve the PLQY of a fluorescent dye up to 100%.<sup>[147,148]</sup> This and many additional factors, such as (i) backbone planarity and rigidity in connection to vibrational and rotational energy losses, (ii)  $\pi$ – $\pi$  interactions and aggregation, and (iii) spatial overlap between the  $S_1$  state electron and hole wavefunctions ultimately define the emission properties, as discussed in the later chapters.

Introduction of a (heavy) transition metal to the conjugated structure induces strong spin–orbit coupling between the singlet and triplet states, known as heavy atom effect, allowing a fast  $S_n \rightarrow T_n$  ISC process and spin-forbidden radiative relaxation from the  $T_1$  excited state to the  $S_0$  ground state as phosphorescence.<sup>[144,145,149,150]</sup> This process is illustrated in Figure 2.5b. Phosphorescent materials can utilize larger amount of excitons than the fluorescent ones, but  $k_r$  for  $T_1 \rightarrow S_0$  transition is still somewhat lower than that for the  $S_1 \rightarrow S_0$  transition due to the spin flip necessary in the former case.<sup>[126]</sup> The low decay rate of phosphorescent emitters may result in exciton quenching, saturation, and triplet–triplet annihilation, which are detrimental to the performance of light-emitting devices.<sup>[150-152]</sup> However, different Pt and Ir complexes have been reported to exhibit  $k_r$  up to the order of  $10^6$   $s^{-1}$  or even higher, which importantly exceed the typical  $k_{nr}$  of triplet excitons.<sup>[153-158]</sup>

The singlet–triplet energy gap ( $\Delta E_{ST}$ ) can be substantially large if the ground state HOMO and LUMO wavefunctions overlap, e.g., in a nearly coplanar D–A–D structured molecule, as the electron configuration is generally maintained at the excited states, referred to as locally excited states (LE). This is often the case in highly fluorescent molecules. In contrast, spatial separation of the HOMO and LUMO wavefunctions by the design of orthogonal donor and acceptor units leads to charge-transfer excitation (CT) character and small  $\Delta E_{ST}$ .<sup>[159,160]</sup> The latter has been used for the transfer of dark triplet excitons back to the radiative singlet state via reverse intersystem crossing (RISC), ultimately for the attainment of emission as delayed fluorescence. This emission mechanism is known as thermally activated delayed fluorescence (TADF),<sup>[161-164]</sup> which name comes from the original understanding that the RISC process is

mediated by thermal energy to raise the triplet excitons to a vibrational level that corresponds energetically to the singlet state, as presented in Figure 2.5c. However, thermal energy and the simplified Jablonski diagram do not provide full picture of the TADF mechanism. It involves vibronic coupling between the lowest local excitation triplet state ( $^3\text{LE}$ ) and the lowest charge-transfer triplet state ( $^3\text{CT}$ ) to promote spin-orbit coupling and spin flip to the lowest charge-transfer singlet ( $^1\text{CT}$ ) state.<sup>[165-171]</sup> The key difference to the fluorescent (and phosphorescent) molecules is that the TADF mechanism allows harvesting of up to 100% of the dark triplet excitons as higher energy radiative singlet excitons, thereby surpassing the 25% singlet exciton yield (and the 75% triplet exciton yield) without the inclusion of heavy metals.<sup>[172-174]</sup> TADF emitters benefit from higher yield of emissive excitons than the fluorescent or phosphorescent ones, but decay rate of the delayed fluorescence is somewhat lower than that of the fluorescent ones due to the involvement of the long-lived triplet excitons. The rate of the RISC process ( $k_{\text{RISC}}$ ) is critical for the TADF lifetime, and delayed fluorescence is generally attainable thanks to the substantially higher  $k_{\text{RISC}}$  ( $10^6$ – $10^7$  s<sup>-1</sup> or even above) compared to the  $k_r$  and  $k_{nr}$  of the triplet states.<sup>[175]</sup>

All the three emission mechanisms described above (and shown in Figure 2.5) have their specific challenges when  $E_g$  (and thereby  $E_{\text{opt}}$ ) is decreased, due to vibronic coupling between the ground state and the different excited states. Organic (metal-free) fluorescent emitters bear some important benefits from an application point of view, which are discussed in detail in the following chapters.

### 3. Organic Optoelectronic Devices

This chapter describes the application of conjugated materials as semiconductors for different optoelectronic devices: organic light-emitting diodes, light-emitting electrochemical cells, and organic photodetectors. The parameters that define the device performance are discussed with some key considerations, keeping in mind that the design of materials for these applications are discussed in depth in the later chapters.

#### 3.1. Organic Light-Emitting Diodes

The positioning of HOMO and LUMO levels of the active material define the recombination site of the injected holes and electrons, and the concomitant generation of radiative photons as electroluminescence (EL), as schematically represented in Figure 1.1 (Chapter 1).<sup>[176-178]</sup> The overall efficiency of this process can be characterized as an external quantum efficiency (EQE, or  $\eta_{\text{Ext}}$ ) of the OLED, that is, the number of emitted photons ( $N_{\text{ph,out}}$ ) divided by the number of injected charges ( $N_{\text{el,in}}$ ):<sup>[150,179]</sup>

$$\eta_{\text{Ext}} = N_{\text{ph,out}}/N_{\text{el,in}} = \Phi_f \times \eta_{\text{ST}} \times \eta_{\text{Rec}} \times \eta_{\text{Out}} = \eta_{\text{Int}} \times \eta_{\text{Out}} \quad (3.1)$$

where  $\Phi_f$  is the PLQY of the emitter, given by Equation (2.6), and  $\eta_{\text{ST}} = 0.25$  for fluorescent emitters, which obey the same spin selection rule as discussed in the case of optical excitation in Chapter 2.3. The key difference between optical and electrical excitation is, however, that in the latter case both singlet excitons and dark triplet excitons can be formed directly at the electron and hole captures.<sup>[141,143,145]</sup>  $\eta_{\text{Rec}}$  is the charge balance factor, i.e., exciton formation efficiency. It describes the fraction of recombining charge carriers relative to the total number of injected carriers. In an ideal case, all injected electrons and holes recombine and  $\eta_{\text{Rec}} = 1$ . However, the charge balance depends strongly on the current density, and imbalanced charge transport and saturation of the emissive sites at high currents can decrease  $\eta_{\text{Rec}} \ll 1$ . A low decay rate of the emitter is disadvantageous for the performance of the device, as the emitter is saturated already at low current densities. This is observed as EQE roll-off when the current density is increased, thus strongly limiting the device operation.<sup>[150,180-183]</sup> The high decay rates of fluorescent emitters typically allow operation at relatively high currents with little EQE roll-offs. The above three factors together describe the internal quantum efficiency (IQE, or  $\eta_{\text{Int}}$ ) of the device, which can be described as the number of generated photons (but not leaving the device) per the number of injected charges.<sup>[150,179]</sup>

The remaining factor,  $\eta_{\text{Out}}$ , is the optical outcoupling efficiency, i.e., the fraction of photons passing through the substrate, anode, and possible interlayers relative to the photons generated in the active layer.  $\eta_{\text{Out}}$  is typically  $\sim 0.2$  due to waveguiding in the glass substrate and different device layers and reflections at the interfaces.<sup>[184,185]</sup> Majority of the photons are either trapped inside the substrate/device or emitted from the edges of the device.<sup>[37]</sup> In a fluorescent OLED, the theoretical maximum EQE is therefore limited to  $\sim 5\%$ .<sup>[179]</sup> As observed,  $\eta_{\text{Out}}$  is a significant source of efficiency loss, and various engineering approaches have been applied to improve the light outcoupling. This is usually done by minimizing the waveguiding effect with different nanostructures,<sup>[186]</sup> microcavity structures,<sup>[187,188]</sup> and microlenses in the device,<sup>[189,190]</sup> which extract the trapped light out of the device.<sup>[191,192]</sup>

Another way to characterize the OLED performance is the current efficiency (cd/A), which represents the ratio of luminance to the applied current density. Luminous efficiency (lm/W) describes the ratio of luminous flux to the electric power input. Both of these parameters take into account the sensitivity of human eye to different wavelengths of visible light, known as photopic response, with a maximum sensitivity at 555 nm.<sup>[150,178,179,193]</sup> The current efficiency and the luminous efficiency are not ideal quantities for OLEDs emitting in the NIR region, for which EQE is commonly used.<sup>[150]</sup> Moreover, since luminance (often referred to as brightness, in  $\text{cd/m}^2$ ) is related to the photopic response and emission in the visible spectral range, radiance ( $R$ , in  $\text{mW/cm}^2$ ) is more practical measure for the intensity of NIR emission.

A plot of current density and radiance versus voltage ( $J$ – $V$ – $R$ ) is used for further evaluation of the device performance: current density ( $J$ , in  $\text{mA/cm}^2$ ), i.e., the ratio of current to the area of the device, and radiance are measured with respect to an increasing applied voltage ( $V$ , V). Turn-on voltage ( $V_{\text{ON}}$ ) describes the minimum voltage to turn on the device, that is, to reach certain increase of radiance (or current) from the baseline.<sup>[37,89,194]</sup>

### 3.2. Light-Emitting Electrochemical Cells

The performance of LECs is characterized largely with the same parameters as described for OLEDs in the previous section. However, in an LEC the electrolyte ions form the p-type and n-type doped regions in the active layer, and in these regions the electric field can be extremely high.<sup>[195]</sup> This results in bending of the energy levels near the electrode/active layer interfaces, as schematically illustrated in Figure 1.2 (Chapter 1). When the applied voltage is large enough to overcome the energy barrier, injection of electrons and holes will take place. The p–n doping

process can be described as the injected electrons being stabilized by uncompensated cationic electrolyte species at the cathode side of the active layer and the injected holes being stabilized by uncompensated anionic electrolyte species at the anode side, thus the naming n-type and p-type doped regions, respectively.<sup>[195-197]</sup> Because of this stabilization, it is possible to inject a large number of charge carriers into the active layer. The two doped regions grow in time and eventually contain the electron–hole recombination zone, given that the doping is balanced, in the middle of the active layer and far from the exciton quenching electrodes.<sup>[44,198-200]</sup>

When the LEC is driven with a constant current density, the formation of the p–n junction doping structure is observed as increasing radiance (or luminance) and decreasing voltage with time during the initial turn-on process. A well-functioning device thus reaches the steady-state operation rapidly. The time to reach certain radiance is reported as the turn-on time.<sup>[201-203]</sup> At the steady-state operation, the p–n junction ensures efficient recombination of electrons and holes in the active layer, and  $\eta_{\text{Rec}} = 1$  also at high current densities.<sup>[46,204-206]</sup> The result may be that the electrolyte ions separate completely at the electrode/active layer interface during the continuous long-term operation, which deteriorates the p–n doping structure, and is observed as decreasing radiance (or luminance).<sup>[43,206-209]</sup> One way to circumvent this is to apply a pulsed or alternating current, which limits the motion of the electrolyte ions.<sup>[210,211]</sup> It is desirable that the active layer itself ensures a stable p–n junction by containing the ions, through the design of the active material and the electrolyte, and allows the operation also under constant current.

### 3.3. Organic Photodetectors

In an OPD, the photogenerated free charge carriers are driven to their respective electrodes by the alignment of the HOMO and LUMO energy levels of the donor and acceptor materials (an internal built-in potential) and even more by the external reverse bias, as represented in Figure 1.3 (Chapter 1).<sup>[59,212-214]</sup> EQE describes the fraction of the incident photons that contribute to the photocurrent, which is measured as the number of photogenerated charges at the electrodes ( $N_{\text{el,out}}$ ) divided by the number of incident photons ( $N_{\text{ph,in}}$ ) at a given wavelength:

$$\text{EQE} = N_{\text{el,out}}/N_{\text{ph,in}} \quad (3.2)$$

Responsivity ( $R$ , in A/W) is a measure of sensitivity of an OPD to light (in the conversion of optical power to electrical current), which can be characterized as the ratio of photocurrent density under illumination ( $J_{\text{ph}}$ , A/cm<sup>2</sup>) to the incident light intensity ( $L_{\text{Light}}$ , W/cm<sup>2</sup>) as:<sup>[59,215]</sup>

$$R = J_{\text{ph}}/L_{\text{Light}} \quad (3.3)$$

It may not be obvious from Equation (3.3) that responsivity varies with the wavelength of the incident light. An alternative expression for responsivity can be derived from EQE as:<sup>[212,213]</sup>

$$R = \text{EQE} \times \lambda q/hc \quad (3.4)$$

where  $\lambda$  is the wavelength,  $q$  is the elementary charge ( $1.602 \times 10^{-19}$  C),<sup>[127]</sup>  $h$  is the Planck constant ( $6.626 \times 10^{-34}$  J s), and  $c$  is the speed of light ( $2.998 \times 10^8$  m/s). Equation (3.4) shows how EQE relates to the responsivity. It is important to obtain high EQE for the attainment of high responsivity. In general, the responsivity can be increased by ramping up the reverse bias, since a higher electric field increases the charge collection efficiency.<sup>[61,215]</sup>

Noise equivalent power (NEP, W) is the minimum optical power that an OPD distinguishes from the noise, that is, an incident light power that generates a photocurrent equal to the noise current ( $i_n$ , in A):<sup>[59,215,216]</sup>

$$\text{NEP} = i_n/R = \sqrt{(A\Delta f)}/D^* \quad (3.5)$$

where  $A$  is the surface area of the device in  $\text{cm}^2$ ,  $\Delta f$  is the electrical bandwidth in Hz, and  $D^*$  is the specific detectivity in  $\text{cm Hz}^{1/2} \text{W}^{-1}$  (Jones).

On the other hand, specific detectivity describes the sensitivity of an OPD in relation to the surface area, the frequency bandwidth, and the noise current, which can be described as:

$$D^* = \sqrt{(A\Delta f)}/\text{NEP} = R\sqrt{(A\Delta f)}/i_n \quad (3.6)$$

The literature commonly describes three different sources of noise that contribute to  $i_n$ : (i) shot noise (or dark current noise) due to statistical fluctuation of the current when operating in the biased mode, (ii) Johnson noise (or thermal noise) due to random thermal motion of the charge carriers, and (iii) Flicker noise, which is inversely proportional to the frequency, whereas the other two are frequency independent.<sup>[59,212,213]</sup> In a typical OPD operation, under reverse bias, the shot noise from dark current is assumed to have the dominant contribution.<sup>[13,72]</sup> Therefore,  $i_n = (2qI_d\Delta f)^{1/2}$  and  $D^*$  can be calculated as following:<sup>[212-214,217]</sup>

$$D^* = R\sqrt{A}/\sqrt{(2qI_d)} = R/\sqrt{(2qJ_d)} \quad (3.7)$$

where  $I_d$  is the dark current in A and  $J_d$  is the dark current density in  $\text{A}/\text{cm}^2$ . The latter form of Equation (3.7) is convenient for the characterization of specific detectivity, since responsivity can be obtained from EQE using Equation (3.4). Measurement of current density at increasing

applied reverse bias (a  $J$ – $V$  plot) in dark and under illumination reveal the values of  $J_d$  and  $J_{ph}$  at a chosen voltage, respectively. Equation (3.7) shows that  $D^*$  is determined not only by the responsivity (photocurrent) but also by the noise (dark current).<sup>[13,218]</sup> The BHJ should ideally deliver as low  $J_d$  as possible, since it is a major limiting factor for the detectivity. Additional electron and hole blocking layers can be used to increase the barrier for charge injection from the anode and cathode, respectively, thereby reducing the dark current under reverse bias. The thickness of the BHJ layer is another factor that affects the dark current. A thicker film usually exhibits lower  $J_d$ , but the thickness also influences the EQE and the responsivity of the device, often contrary to the desired change in dark current.<sup>[61,212,217,219-221]</sup>



## 4. Synthesis of Conjugated Polymers and Small Molecules for NIR-OLEDs

The major challenges in the design of efficient NIR emitters are (i) aggregation quenching of the emission in solid state, (ii) pronounced coupling of the excited state and the ground state vibronic energy levels toward decreasing energy gap, known as the “energy gap law”,<sup>[222,223]</sup> and (iii) intrinsic limitation of the yield of emissive excitons from the singlet excited state. A number of strategies have been introduced to overcome these challenges and to improve the performance of organic (metal-free) compounds in the NIR range.<sup>[224,225]</sup> Aggregation-induced emission (AIE) enhances the solid-state emission yield by restricting intramolecular motion (rotation and/or vibration) of the emitter.<sup>[226-228]</sup> Ledwon et al.<sup>[229]</sup> reported a top-performing AIE-active benzothiadiazole small molecule and an OLED emitting at 688 nm. TADF harvests the commonly dark triplet excitons in organic compounds (Chapter 2.3).<sup>[164,168,230-234]</sup> In recent years, examples of TADF emitters and various TADF-AIE hybrid systems have been reported to exceed a peak wavelength of 700 nm and an EQE of ~10%.<sup>[235-241]</sup> In such triplet harvesting compounds the exciton recombination dynamics typically fall in the hundreds of nanoseconds or even in the microsecond range. This limits the operational bandwidth when integrated in devices for telecommunication. Fluorescent polymers and small molecules are preferred for Li-Fi applications,<sup>[24,26]</sup> since the fluorescence lifetime of these materials is typically in the order of few nanoseconds or less, allowing data transmission rates up to Gb/s.

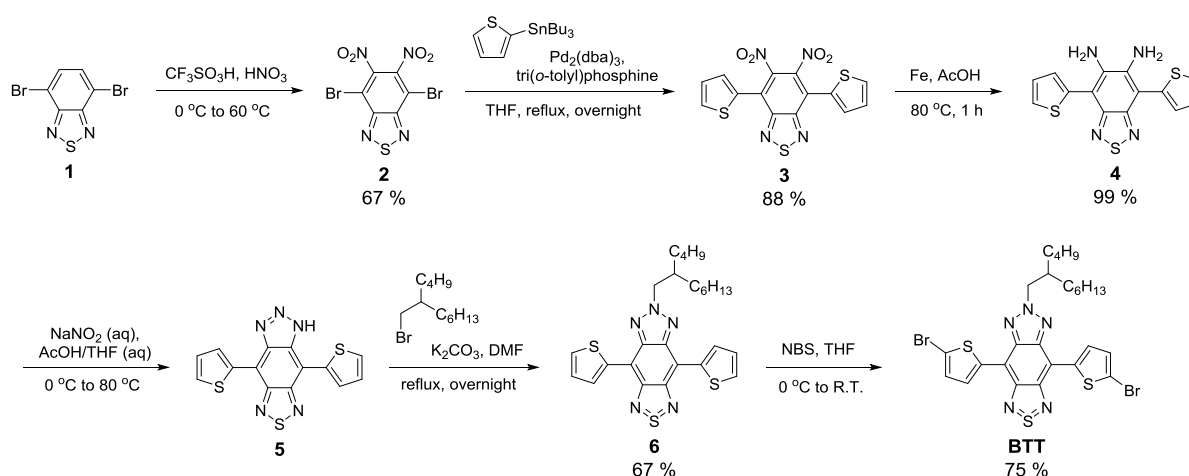
To redshift the emission of a fluorophore into the NIR region, one needs a planar structure with strong electron donating and accepting moieties. Such planar structures benefit from the concomitant extended conjugation and decreased energy gap but, at the same time, suffer from strong intermolecular  $\pi$ - $\pi$  stacking, which is known as aggregation. Therefore, the NIR emitter is usually diluted in a solid-state polymer or small molecule matrix, referred to as a host/guest system.<sup>[88,165,242]</sup> The host matrix should physically separate the emitters from each other to avoid strong aggregation, yet allow efficient energy transfer and charge trapping at the NIR emissive sites for an ideal OLED performance. In this chapter, two different approaches are discussed with the aim of designing organic host and guest materials for an efficient NIR emission, covering papers I and II.

## 4.1. Random Copolymers Comprising BTT as the Emitter

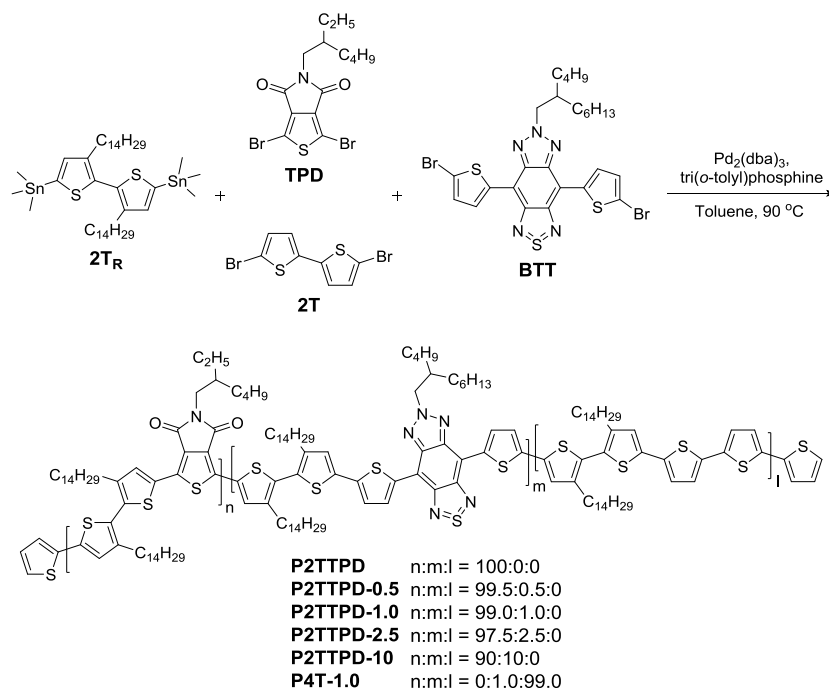
### 4.1.1. Design Strategy

Phase separation of the host matrix and the NIR emitter may become a significant problem in the host/guest type OLEDs. Diluting the emitter within a host polymer backbone can be an ideal way to obtain a solution-processable homogeneous blend and prevent the NIR molecules forming phase separated aggregates.<sup>[194,243]</sup> The design of host polymer and guest emitter generally requires (i) spectral overlap of the host emission and guest absorption to ensure efficient energy transfer, (ii) careful optimization of the host and guest band alignment to allow charge injection and trapping specifically at the NIR sites, and (iii) suitable energy levels with regard to the electrodes and interlayer materials available for device fabrication. In this study, two wide gap polymers were chosen as host matrices: poly[3,3'-ditetradecyl-2,2'-bithiophene-5,5'-diyl-*alt*-5-(2-ethylhexyl)-4*H*-thieno[3,4-*c*]pyrrole-4,6(5*H*)-dione-1,3-diyl] (P2TTPD) and poly[3,3'-ditetradecyl-2,2':5',2'':5'',2'''-quaterthiophene-5,5'''-diyl] (P4T). The amount of NIR emitter is highly related to the performance of the OLEDs and the optimum concentration needs to be studied for each new system. The low-gap NIR molecule 6-(2-butyloctyl)-4,8-di(thiophen-2-yl)-[1,2,3]triazolo[4',5':4,5]benzo[1,2-*c*][1,2,5]thiadiazole (BTT, Scheme 4.1 and 4.2) was copolymerized into the host polymer backbone with the concentration varying from 0.5 to 10%. In all cases, the NIR emitter was dispersed in the host polymer backbone, allowing cost-efficient fabrication of the devices from a single active layer material.

### 4.1.2. Material Synthesis and Characterization



**Scheme 4.1.** Synthesis of the BTT monomer.



**Scheme 4.2.** Synthesis of the random copolymers.

The BTT monomer was synthesized via a six-step synthesis route, starting from nitration of **1** in excess of fuming nitric acid to obtain **2** (Scheme 4.1). This type of nitration necessitates the use of fuming triflic acid as the solvent, since the reaction in concentrated sulfuric acid instead resulted in a mono-nitrated compound. Pd-catalyzed Stille coupling introduced the thiophene donor groups on molecule **3**. For the ring-closing reaction, the nitro groups were reduced with iron powder in acetic acid. A simple post-reaction procedure by extraction with diethyl ether ensured full removal of the iron and yielded the diamine **4**, which was used directly to the next step due to the instability of similar aromatic diamines in air. Alkylation of the triazole **5** in basic conditions yielded compound **6**, with the side chain on the central nitrogen atom as the major product. The good selectivity at the central nitrogen atom, with respect to the previously published procedures,<sup>[244-247]</sup> is probably driven by the steric hindrance between the thiophenes and the bulky side chain. In fact, the branched 2-butyloctyl side chain was selected to avoid strong aggregation of the NIR emissive sites in the solid state. The final bromination step and purification with column chromatography yielded BTT as the NIR monomer.

The polymers were synthesized by varying the amount of the commercial 2,2'-bithiophene (2T) and 3,3'-ditetradecyl-2,2'-bithiophene (2T<sub>R</sub>) donor monomers and 5-(2-ethylhexyl)-4H-thieno[3,4-c]pyrrole-4,6(5H)-dione (TPD) and BTT acceptor monomers in Pd-catalyzed Stille polycondensation polymerization (Scheme 4.2). For simplicity, both 2T and 2T<sub>R</sub> are referred

to as 2T in the polymer abbreviations. P2TTPD, P2TTPD-0.5, P2TTPD-1.0, P2TTPD-2.5, and P2TTPD-10 contain 0, 0.5, 1.0, 2.5, and 10% of BTT in the polymer backbone, based on the initial molar feed. Similarly, P4T-1.0 contain 1% of BTT. Characterization of the exact molar ratios is demanding, especially in the case of low ( $\leq 2.5\%$ ) BTT concentration. However, it is noteworthy that matrix assisted laser desorption ionization-time of flight (MALDI-TOF) technique has been successfully applied for the characterization of small differences in the chemical structures of other copolymers.<sup>[248,249]</sup> In this study, the number-average molecular weights ( $M_n$ ) of the polymers were comparable, 10.2 kg/mol (polydispersity index, PD 1.9) for P2TTPD, 9.2 kg/mol (2.0) for P2TTPD-0.5, 10.8 kg/mol (1.9) for P2TTPD-1.0, 10.4 kg/mol (1.8) for P2TTPD-2.5, and 16.7 kg/mol (1.7) for P2TTPD-10, as characterized with analytical gel permeation chromatography (GPC). The  $M_n$  increased to 33.4 kg/mol (2.2) for P4T-1.0, probably due to better reactivity of the brominated sites of the electron donating 2T compared to the electron withdrawing TPD. The polymers showed good thermal stability in thermogravimetric analysis (TGA), and the degradation onset temperature was  $>380$  °C in all cases. Differential scanning calorimetry (DSC) measurements did not reveal any detectable peak in the temperature range of 0–350 °C, although DSC is not very sensitive method for the detection thermal transitions of conjugated polymers.

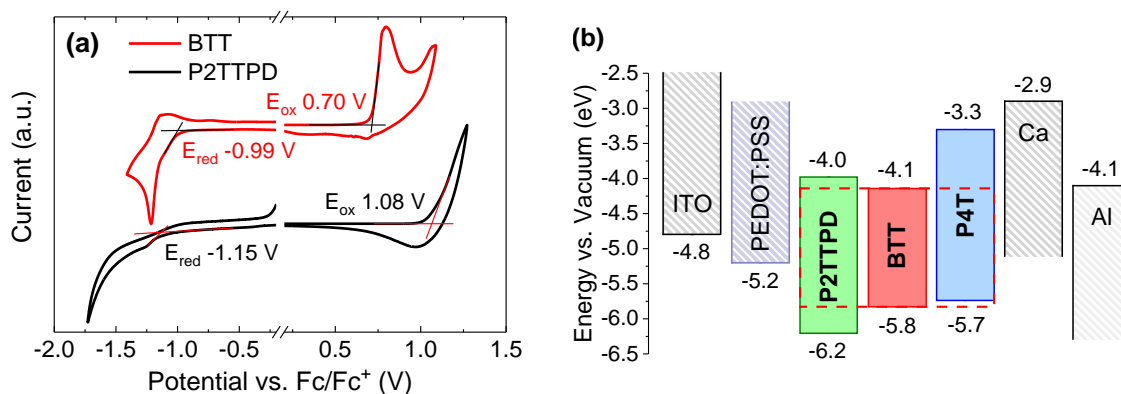


**Figure 4.1.** (a) CV traces of P2TTPD polymer and BTT monomer. (b) NIR-OLED device architecture and energy levels of P2TTPD and P4T host polymers and BTT monomer.

Electrochemical properties of the polymers and the BTT monomer were studied with CV measurements. P2TTPD host polymer showed irreversible oxidation and reduction processes when measured at a scan rate of 100 mV/s (Figure 4.1a). However, it was possible to determine the HOMO and LUMO energy levels from the oxidation and reduction onset potentials, respectively. As shown in Figure 4.1b, both HOMO and LUMO of P2TTPD were deeper than

the previously reported values for a similarly structured polymer without any side chains on the 2T donor ( $-5.4/-3.1$  eV).<sup>[250]</sup> Tail-to-tail alkylation of the 2T moiety in an analogous polymer lowered the LUMO to  $-4.0$  eV,<sup>[251]</sup> which is in line with that of P2TTPD. The low-lying HOMO of P2TTPD is ascribable to the head-to-head side chains, which induce torsion to the polymer backbone and somewhat reduce the effective conjugation. The backbone torsion was further confirmed by DFT calculations in paper I. Significantly, the HOMO and LUMO of BTT were encompassed by those of the P2TTPD host, as indicated by the red dashed line in Figure 4.1b. This type of band alignment should allow charge injection specifically at the NIR emissive BTT sites. In case of P4T host polymer, the HOMO was up-lying by 0.1 eV compared to BTT. The addition of TPD to the P2TTPD backbone not only affected the LUMO but also lowered the HOMO level, so that the host polymer would not function as charge trap or inhibit charge transport to BTT.

#### 4.1.3. Optical Properties and NIR-OLEDs Performance

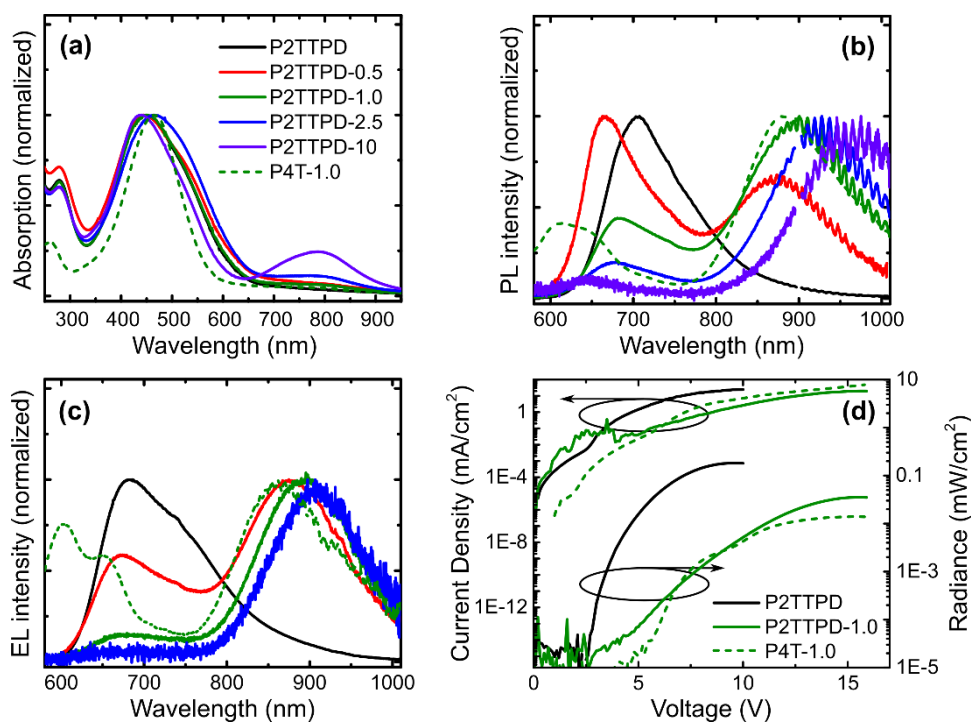


**Figure 4.2.** Normalized (a) absorption and (b) PL spectra of the copolymer thin films (100 nm, excitation with a 450 nm laser diode). (c) EL spectra measured at 9 V (P2TTPD), 15 V (P2TTPD-0.5), and 16 V (P2TTPD-1.0, P2TTPD-2.5, P4T-1.0). (d) NIR-OLED device characteristics: current density and radiance versus voltage. The device area is 3.5 mm<sup>2</sup>.

Absorption spectra of the polymers in thin films are shown in Figure 4.2a. The absorption profiles of the BTT containing polymers largely represent those of the P2TTPD and P4T host, peaking at 450 nm and 465 nm, respectively, but an additional absorption band is observed at ~790 nm. The low-energy band is ascribable to the NIR emitter, as its intensity increases with increasing BTT feed. P2TTPD shows a PL peak maximum at 708 nm (Figure 4.2b). By taking into account the ratio between the photons emitted and the photons absorbed, a PLQY of 20% was calculated for P2TTPD. This is excellent value for a polymer emitter, given that most of the emission passes the NIR range at  $\lambda > 700$  nm. The long PL wavelength of the host provided almost complete spectral overlap with the absorption of BTT, which should deliver efficient energy transfer in the BTT containing polymers. NIR emission was obtained already at 0.5% BTT feed but the residual peak from the host still dominated the PL of P2TTPD-0.5. This suggests that the energy transfer was not complete. The residual red emission from the host appears blueshifted with respect to P2TTPD, as the low-energy tail was efficiently quenched by the BTT moiety. Better spectral purity was obtained with higher BTT feed in P2TTPD-1.0, P2TTPD-2.5, and P2TTPD-10 but the increased concentration of BTT led to aggregation of the emitter, which was observed as redshift of the NIR PL from 874 nm to 897, 924, and 945 nm, respectively. Strong aggregation is detrimental to the OLED performance, which is well-known for conjugated systems in general and in the specific case of NIR emitters.<sup>[194,252-254]</sup> It was surprising that the PL of P4T-1.0 was comparable to P2TTPD-1.0, despite the poor spectral overlap between the P4T host emission and the BTT guest absorption.

The NIR-OLED device architecture is shown in Figure 4.1b. ITO/PEDOT:PSS was used as the anode and Ca/Al as the cathode. The active layer comprised one of the polymers and the thickness was optimized to 100 nm by spin-coating. The EL spectra are shown in Figure 4.2c and the results of the device performance are summarized in Table 4.1. P2TTPD exhibits an EL maximum at 690 nm (the operation of this device is shown in Figure 1.1c). The 20 nm blueshift with respect to the PL spectrum might be due to differential electronic processes in the active layer,<sup>[255]</sup> or thermochromism, i.e. decrease of the conjugation length upon a slight temperature raise when an electric current is applied.<sup>[256]</sup> Nevertheless, the EL remained unchanged and mostly in the NIR when the bias voltage was varied by  $\pm 5$  V. The device reached an EQE of 0.49% and average maximum radiance ( $R_{MAX}$ ) of 0.19 mW/cm<sup>2</sup>, which are good values for a polymer emitter in such long wavelength region. The device exhibited  $V_{ON}$  at 2.4 V (Figure 4.2d), which is exceptionally low for conjugated polymers.<sup>[194,257-259]</sup>

**Table 4.1.** Summary of the NIR-OLED performance.

polymer	BTT (%)	$V_{ON}$ (V)	$R_{MAX}$ (mW/cm <sup>2</sup> )	EQE (%)	EL peak (nm)
P2TTPD	0	2.4 ± 0.3	0.19	0.49 ± 0.12	690
P2TTPD-0.5	0.5	4.3 ± 0.3	0.13	0.15 ± 0.01	680, 880
P2TTPD-1.0	1	4.3 ± 0.6	0.07	0.08 ± 0.05	684, 896
P2TTPD-2.5	2.5	6.4 ± 1.3	0.02	0.010 ± 0.001	909
P2TTPD-10	10	4.6 ± 0.5	0.001	0.004 ± 0.001	930
P4T-1.0	1	4.7 ± 0.5	0.02	0.06 ± 0.01	604, 864

When BTT was added to the polymer backbone, the residual host emission was quenched more efficiently in the OLEDs compared to the PL experiments, and the NIR peak from BTT dominated the EL in all concentrations. This indicates the importance of the band alignment of the low-gap NIR emitter in the charge transport and charge trapping at these sites, which effectively leads to exciton formation at their locations. The device based on P2TTPD-0.5 as the emitter delivered an EQE of 0.15% and radiance of 0.13 mW/cm<sup>2</sup>. The emission from the host became more prominent at increased bias voltage. This indicates that the EL from BTT saturated at lower voltage compared to the P2TTPD host and increased the rate of exciton formation and recombination at the higher energy sites. An increased amount of BTT in P2TTPD-1.0 resulted in a vanishingly small fraction of emission coming from the host and virtually pure NIR EL peaking at 896 nm. However, the EQE dropped to 0.08% together with the radiance of 0.07 mW/cm<sup>2</sup>. Further increase of the BTT concentration redshifted the EL above 900 nm, without any detectable emission from the host, but also brought the EQE further down to 0.004% (for P2TTPD-10). The decrease of EQE can be attributed to the aggregation quenching of the emission at increased BTT content, as in the case of PL. Although the EQE values may appear low in comparison to visible light emitters, P2TTPD-0.5 and P2TTPD-1.0 are among the best performing polymers emitting at ~900 nm.<sup>[194,243,258,260]</sup> P4T-1.0 exhibits an EL maximum at 864 nm, which is 30 nm blueshifted compared to P2TTPD-1.0. It is evident that the visible emission component from the host was significantly higher and blueshifted in P4T-1.0 as compared to P2TTPD-1.0. Although the EQE of 0.06% was comparable to that of P2TTPD-1.0, the actual portion of NIR emission from P4T-1.0 was at least 30% lower than that obtained from P2TTPD-1.0. This can be attributed to a less efficient charge transfer onto the NIR emitter in P4T-1.0. Pure NIR emission was obtained only when the energy and charge

transfer together allowed efficient energy funneling and charge trapping at the low-gap BTT sites in P2TTPD-1.0.

To conclude, random copolymers comprising P2TTPD as the host and BTT as the emitter represent the few organic active materials for NIR-OLEDs that emit in the 900 nm region. Copolymerization allows solution-processing of devices from a single active material, which is beneficial for the fabrication of low-cost, flexible, and non-toxic biocompatible electronics. Although copolymers should ensure a homogeneous chemical structure in the active layer, they may contain structural defects that affect the device performance. Specifically, by taking into account the small loading of BTT emitter in the P2TTPD backbone and the limited length of the polymer chains ( $\leq 20$  repeating units), statistically only a few of the polymer chains contained a NIR emitter. Hence, the shorter wavelength PL from P2TTPD-1.0 must originate not only from the host polymer segments that were too far from the BTT centers to allow intrachain energy transfer, but also from polymer chains that were purely that of the P2TTPD host and similarly far from the BTT sites to allow interchain energy transfer. Despite the incomplete energy transfer, the host emission was quenched almost completely in the EL spectra, as the injected charges could migrate more easily from one chain to another, ultimately favoring exciton formation and recombination at the low-gap sites. Further study revealed that low  $V_{ON}$  and pure NIR emission could be obtained only by using P2TTPD as the host, thanks to the combination of energy and charge transfer that allowed exciton formation selectively at the BTT sites.

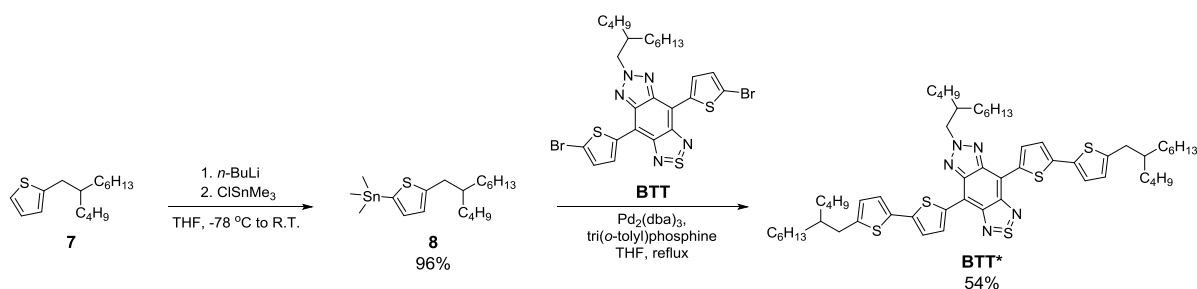
## 4.2. BTT\* Small Molecule:Polymer Blends

### 4.2.1. Small Molecule as the Emitter

As discussed in the previous chapter, dilution of the NIR emitter into a host matrix is crucial for optimum device performance. Although copolymerization is an efficient way to separate the NIR molecules in the host matrix without causing phase separation, organic small molecule emitters can benefit from (i) control of the exact amount of the emitter in blend with the host matrix, (ii) precise tuning of the molecular orbital energy levels with respect to the host, and (iii) careful purification of the NIR molecule. Therefore, it was highly appealing to extend the study on BTT further and modify the structure to obtain a solution-processable small molecule NIR emitter. Poly(9,9-dioctylfluorene-*alt*-benzothiadiazole) (F8BT) has often been used as a standard host polymer in NIR-OLEDs, despite its poor spectral overlap with the dyes.<sup>[89,261,262]</sup>

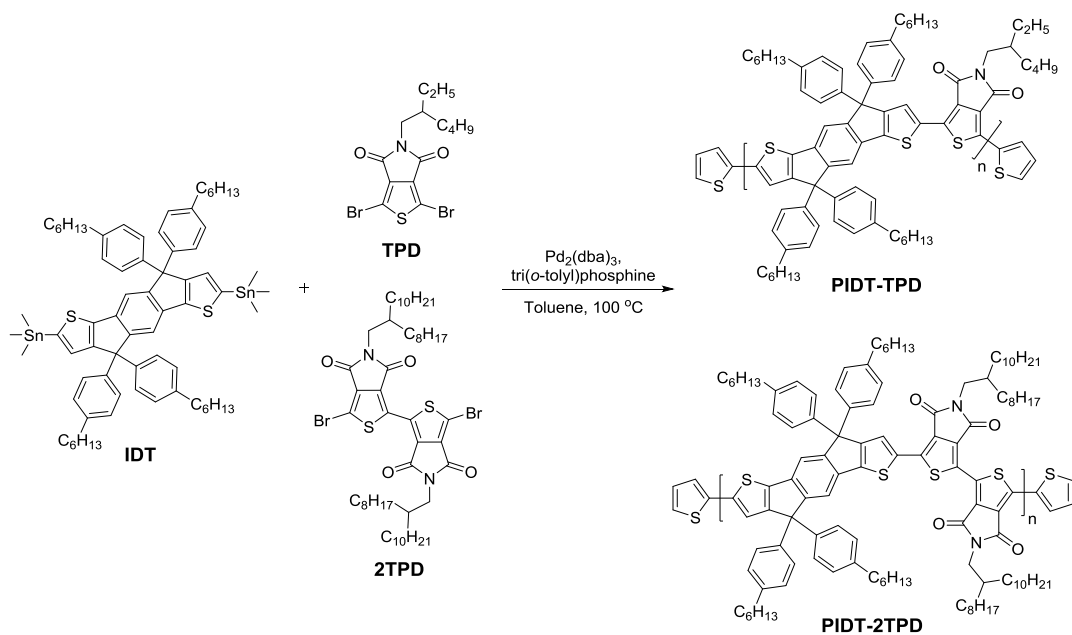
Clearly, the host polymer should be selected so as to allow spectral overlap between the host photoluminescence and the NIR dye absorption, as well as good charge transport properties for charge recombination selectively at the NIR sites. In this study, a BTT-based NIR molecule and two new tailor-fit host polymers are synthesized and characterized for excellent NIR-OLEDs performance.

#### 4.2.2. Material Synthesis and Characterization



**Scheme 4.3.** Synthesis of the BTT\* small molecule.

The previously used BTT monomer was modified to obtain 6-(2-butyl-4-octyl)-4,8-bis(5'-(2-butyl-4-octyl)-[2,2'-bithiophen]-5-yl)-1*H*-[1,2,3]triazolo[4',5':4,5]benzo[1,2-*c*][1,2,5]thiadiazole (BTT\*) small molecule (Scheme 4.3). The commercial 2-butyl-4-octyl substituted thiophene **7** was functionalized with a trimethylstannyl group to obtain compound **8**. BTT\* was obtained in a satisfactory yield via Stille coupling and multiple column chromatography purifications. As a design motif, the additional thiophenes were introduced to decrease the energy gap of the D–A–D structured molecule and thus further redshift its emission into the NIR region. The branched side chains were selected on the central BTT acceptor and the thiophene donors to ensure good solubility and miscibility with the host polymer matrices.



**Scheme 4.4.** Synthesis of the PIDT-TPD and PIDT-2TPD host polymers.

The PIDT-TPD and PIDT-2TPD host polymers were synthesized via Stille coupling of indacenodithiophene (IDT) donor and thieno[3,4-*c*]pyrrole-4,6-dione (TPD) or bithieno[3,4-*c*]pyrrole-4,4',6,6'-tetrone (2TPD) acceptor monomers, respectively (Scheme 4.4). The *p*-hexylphenyl substituents were added on IDT to reduce the polymer chain aggregation, as the bulky groups align somewhat perpendicular to the planar IDT backbone.<sup>[263,264]</sup> Likewise, the 2-octyldodecyl side chains on 2TPD were selected for good solubility and steric hindrance to prevent strong aggregation. From the two polymers, higher  $M_n$  was obtained for PIDT-2TPD (55.7 kg/mol, PD 2.4) as compared to PIDT-TPD (26.3 kg/mol, PD 2.1) due to the long side chains attached on 2TPD. TGA indicated that both the PIDT-TPD and PIDT-2TPD host polymers and BTT\* molecule exhibited high thermal stability, without significant weight loss until  $400\text{ }^\circ\text{C}$ . The polymers did not show any detectable thermal transition on DSC measurements. For BTT\*, two distinctive phase transitions were observed, corresponding to exothermic crystallization ( $T_c$ ) at  $-1\text{ }^\circ\text{C}$  and endothermic melting ( $T_m$ ) of the crystallized phase at  $87\text{ }^\circ\text{C}$ . These transitions were not observed in the blends with PIDT-TPD and PIDT-2TPD host polymers.

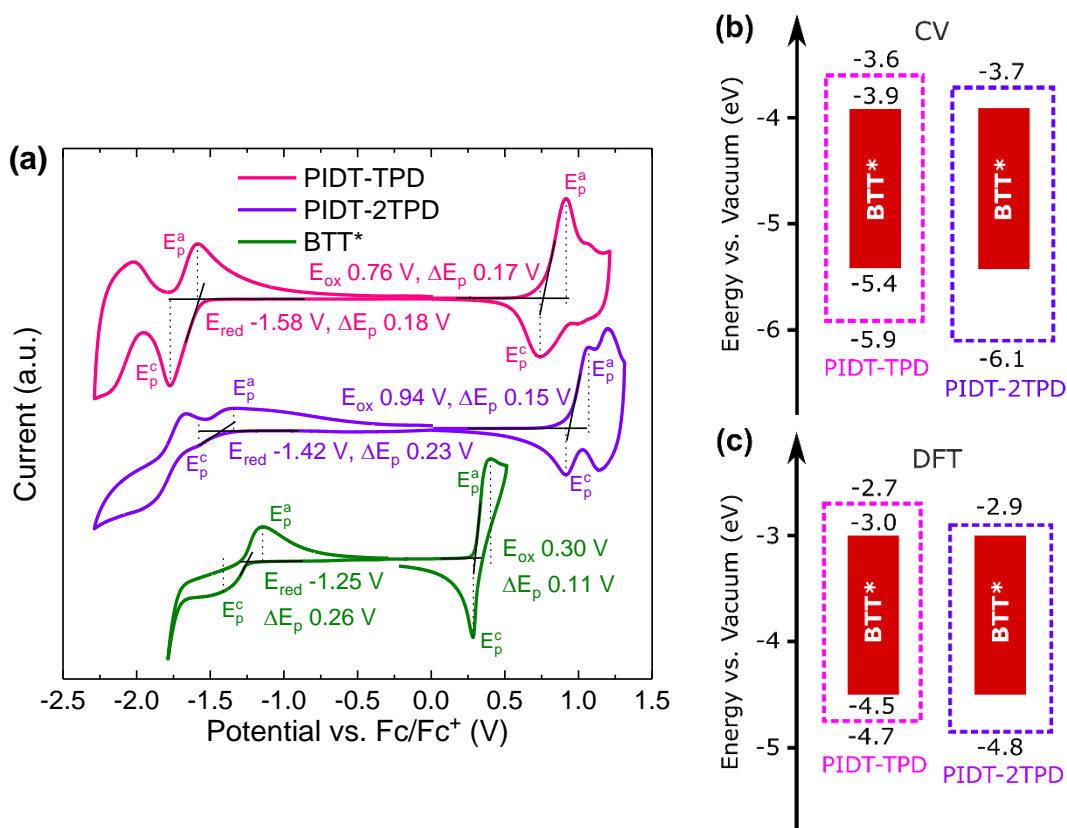


**Figure 4.3.** (a) CV traces of PIDT-TPD and PIDT-2TPD host polymers and BTT\* molecule and the corresponding (b) CV and (c) DFT-calculated HOMO and LUMO energy levels.

Both density-functional theory (DFT) calculations and CV measurements were employed to study the electronic properties of the two host polymers and BTT\* molecule (see Chapter 8.3 for detailed DFT methodology). The calculated HOMO and LUMO energy levels are shown in Figure 4.3c, where the dashed boxes illustrate the energy gap of PIDT-TPD and PIDT-2TPD and the solid box that of BTT\*. The calculations suggest that the energy gap of BTT\* is fully contained in either of the two host polymers. This was fully supported by the results from CV (Figure 4.3b), despite the numerical discrepancies between the DFT calculations in ideal gas phase and the CV measurements in solid-state thin films. Both PIDT-TPD and PIDT-2TPD exhibited good electrochemical stability and quasi-reversible oxidation and reduction processes, as the  $\Delta E_p$  values deviated slightly from a fully reversible redox couple at a scan rate of 100 mV/s (Figure 4.3a). The HOMO and LUMO of BTT\* increased by 0.40 and 0.26 eV, respectively, compared to the previously discussed BTT monomer. This corresponds to a 0.14 eV reduction of the energy gap, as expected from the extended conjugation of the BTT\* backbone. Further DFT calculations on BTT\*, in paper II, showed

that the electron and hole wavefunctions exhibit partial overlap at the lowest excited singlet  $S_1$  state, which suggests sufficient singlet exciton yield in the molecule.<sup>[105,265,266]</sup>

### 4.2.3. Optical Properties

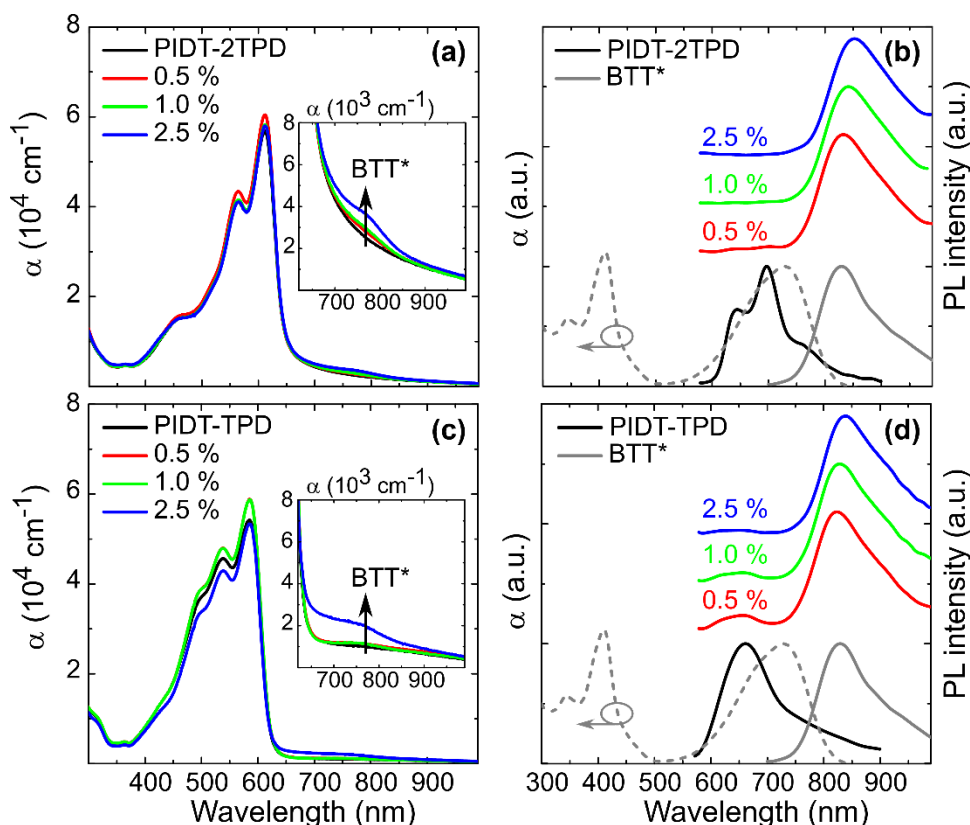


**Figure 4.4.** (a,c) Absorption of the host polymers and blends containing 0.5, 1.0, and 2.5% of BTT\* in thin films (100 nm). (b,d) PL spectra of the corresponding films (excitation with a 520 nm laser diode). Grey lines represent the absorption (dashed) and PL (solid) of BTT\* in toluene solution. PL of BTT\* measured by using excitation with a 670 nm laser diode.

Absorption and PL spectra of the two polymers and blends incorporating 0.5, 1.0, and 2.5% of BTT\* in thin film, and BTT\* in dilute toluene solution, are shown in Figure 4.4. BTT\* exhibited two absorption bands in solution peaking at 410 and 730 nm (grey dashed line). The entire PL spectrum of BTT\* was in the NIR ( $>700$  nm), with a PLQY of 29%, which is among the highest values reported for a metal-free NIR emitter.<sup>[135]</sup>

The absorption spectra of PIDT-2TPD and PIDT-TPD films peaked at 620 and 580 nm, respectively. Increasing the amount of BTT\* in the blends was observed as another NIR absorption band at  $\sim 750$  nm, as indicated by the insets in Figure 4.4a,c. PL of PIDT-2TPD and PIDT-TPD peaked at 700 and 660 nm (black line in Figure 4.4b,d), respectively, which means

that both polymers offered almost complete spectral overlap with the absorption of BTT\*, and that is especially good if compared to the commonly used host polymers like F8BT.<sup>[89,261,262]</sup> PIDT-2TPD exhibited a PLQY of 18%, which an excellent value for a polymer emitter considering that half of the photons are emitted in the NIR, as discussed for P2TTPD in the previous chapter. PIDT-TPD exhibited a lower PLQY of 5%. However, the spectral overlap ensured that the PL of the blends with both hosts peaked at 830 nm, which is consistent with the PL of BTT\* in solution. The fraction of photons that emitted in the NIR was 95% for the 0.5% blends, with an overall PLQY of 17 and 18% for PIDT-2TPD and PIDT-TPD blend, respectively. The spectral purity increased to 99% for the 1.0% blends, with PLQY remaining >15%. Importantly, such PLQY values are the highest reported for a metal-free emitter (either singlet or triplet harvesting) in the solid state and emitting in this long spectral range.<sup>[241]</sup>

It is interesting that both blends with 0.5% BTT\* showed similar PLQYs, despite the very different PLQYs of the two host polymers. Assuming that the PLQY of BTT\* in the blends (if only BTT\* is excited) is same as that in the solution, 29%, a host-to-guest energy transfer efficiency (i.e., quantum yield,  $\eta_{ET}$ ) can be calculated as a ratio of the fluorescence efficiency of the blend and BTT\* in solution, that is,  $\eta_{ET} = \Phi_{f,blend}/\Phi_{f,BTT^*}$ . This gives  $\eta_{ET}$  of 56% and 59% for PIDT-2TPD and PIDT-TPD blends, respectively. In fact,  $\eta_{ET}$  describes the fraction of photons absorbed by the host and further transferred to the BTT\* guest, which fraction is given by:<sup>[129]</sup>

$$\eta_{ET} = k_{ET}/(k_{ET} + 1/\tau_{f,host}) \quad (4.1)$$

where  $k_{ET}$  is the energy transfer rate and  $\tau_{f,host}$  is the fluorescence lifetime of the host. The latter was  $0.5 \times 10^{-9}$  s for PIDT-2TPD and  $0.8 \times 10^{-9}$  s for PIDT-TPD, which values were obtained from TCSPC measurements in paper II. With Equation (2.7),  $\eta_{ET}$  can be described as:

$$\eta_{ET} = k_{ET}/(k_{ET} + k_{r,host} + k_{nr,host}) \quad (4.2)$$

where, using Equation (2.8),  $k_{r,host}$  of  $0.36 \times 10^9$  s<sup>-1</sup> and  $0.062 \times 10^9$  s<sup>-1</sup> were calculated for PIDT-2TPD and PIDT-TPD, respectively. Equation (2.9) then gives  $k_{nr,host}$  of  $1.64 \times 10^9$  s<sup>-1</sup> and  $1.24 \times 10^9$  s<sup>-1</sup> for the two respective polymers. Alternatively, the energy transfer efficiency can be calculated from the fluorescence lifetime of the host polymer in the absence ( $\tau_{f,host}$ ) and in the presence of BTT\* ( $\tau_{f,host:BTT^*}$ ):<sup>[129]</sup>

$$\eta_{ET} = 1 - (\tau_{f,host:BTT^*}/\tau_{f,host}) \quad (4.3)$$

and, accordingly, the energy transfer rate can be calculated under these same conditions:

$$k_{\text{ET}} = (1/\tau_{f,\text{host:BTT}^*}) - (1/\tau_{f,\text{host}}) \quad (4.4)$$

Then, as calculated using Equations (4.3) and (4.4),  $k_{\text{ET}}$  was  $\sim 2.5 \times 10^9 \text{ s}^{-1}$  for PIDT-2TPD blend and  $\sim 1.8 \times 10^9 \text{ s}^{-1}$  for PIDT-TPD blend. Importantly,  $k_{\text{ET}}$  was about 1.5 times higher than  $k_{\text{nr}}$  with both host polymers, which explains the similar PLQYs of the two blends: the energy transfer process effectively competes with the nonradiative processes, thereby overcoming the significantly lower  $k_r$  of PIDT-TPD compared to that of PIDT-2TPD.

#### 4.2.4. NIR-OLEDs Performance

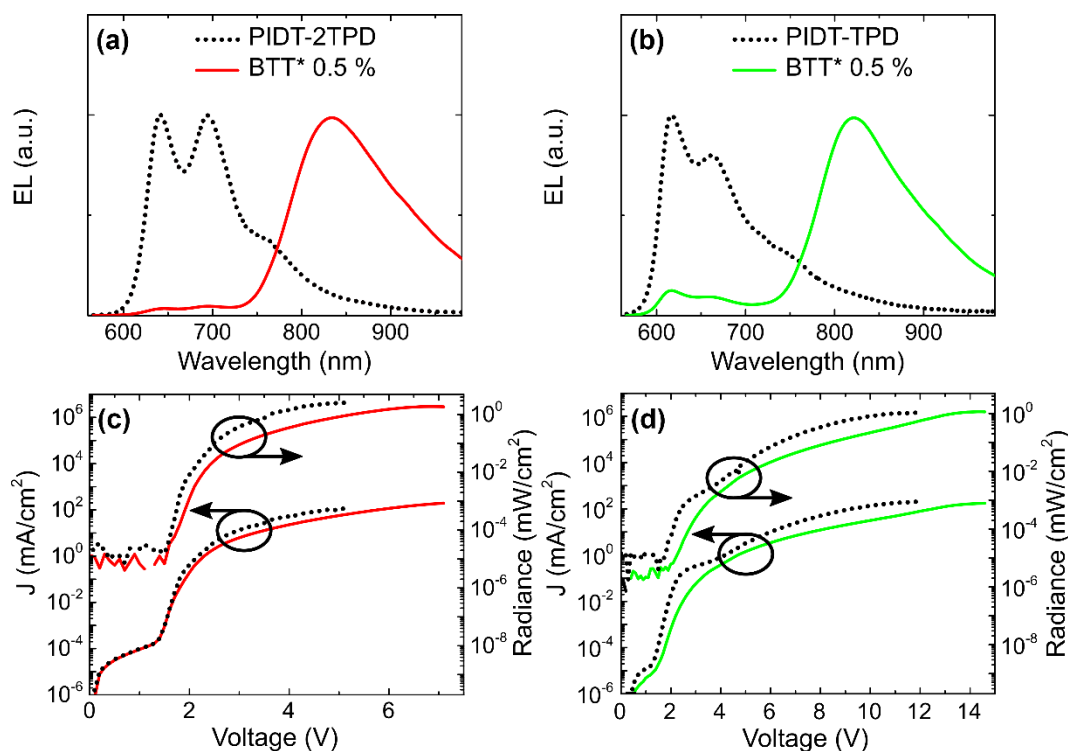


**Figure 4.5.** (a,b) EL spectra and (c,d)  $J$ - $V$ - $R$  of the NIR-OLEDs incorporating PIDT-2TPD, PIDT-TPD, and 0.5% blends of BTT\*. EL spectra measured at 4 V (PIDT-2TPD devices) and 10 V (PIDT-TPD devices).

NIR-OLEDs were fabricated from the PIDT-2TPD and PIDT-TPD host polymers and 0.5, 1.0, and 2.5% BTT\* blends by spin-coating, using ITO/PEDOT:PSS anodes and Ca/Al cathodes. EL spectra of the devices incorporating the two host polymers and the 0.5% blends as the active layer are shown in Figure 4.5. The emission of neat PIDT-2TPD and PIDT-TPD devices were far in the red/NIR range, with approximately half and one third of the photons emitting in the NIR, respectively. The percentage of emission in the NIR for different devices are summarized in Table 4.2. PIDT-2TPD exhibited an ultra-low  $V_{\text{ON}}$  of 1.7 V, which is slightly

lower than that of PIDT-TPD at 1.9 V, thus strongly indicating that the additional TPD group affords optimum charge transport and injection properties in the host matrix. Notably, the EL spectra of PIDT-2TPD device was measured at lower bias (4 V) compared to PIDT-TPD device (10 V). PIDT-2TPD device also exhibited a high radiance of 2.3 mW/cm<sup>2</sup> and one of the highest EQEs (1.55 %) obtained from a red/NIR-emitting metal-free polymer, as reported by Adachi et al.<sup>[241]</sup>

The best NIR performance was obtained with a blend of PIDT-2TPD and 0.5% of BTT\*. The EL peaked at 840 nm, with a maximum EQE of 1.16% (average 1.09%) and radiance of 1.55 mW/cm<sup>2</sup>. Remarkably, the device showed very little EQE roll-off and it could be operated at currents up to 200 mA/cm<sup>2</sup> while maintaining the EQE above 0.5%. Efficient energy and charge transfer in the blend facilitated almost complete quenching of the emission of PIDT-2TPD by the BTT\* molecule and virtually pure (98%) EL in the NIR. The average radiative turn-on voltages of the blend devices remained the same as that of the neat PIDT-2TPD device (1.7 V) at all concentrations, confirming that most charge injection/transport occurred via the host polymer. Such values are the best reported for a purely organic (metal-free) NIR-OLED emitting above 800 nm,<sup>[241]</sup> thanks to the new PIDT-2TPD matrix, which delivered optimum spectral overlap and charge transport properties in blend with BTT\*.

**Table 4.2.** Summary of the NIR-OLED performance.

active layer	$V_{ON}$ (V)	$R_{MAX}$ (mW/cm <sup>2</sup> )	EQE (%)	EL in NIR (%)
PIDT-2TPD	1.7 ± 0.1	2.3 ± 0.5	1.55 ± 0.10	46
0.5% BTT*	1.7 ± 0.1	1.5 ± 0.4	1.09 ± 0.05	98
1.0% BTT*	1.7 ± 0.1	1.3 ± 0.3	0.88 ± 0.04	98
2.5% BTT*	1.7 ± 0.1	0.3 ± 0.1	0.87 ± 0.06	99
PIDT-TPD	1.9 ± 0.1	0.9 ± 0.2	0.36 ± 0.02	34
0.5% BTT*	2.0 ± 0.2	1.4 ± 0.3	0.48 ± 0.01	94
1.0% BTT*	1.8 ± 0.1	1.7 ± 0.3	0.43 ± 0.03	96
2.5% BTT*	2.3 ± 0.1	0.3 ± 0.1	0.31 ± 0.11	96

The PIDT-TPD blend devices exhibited turn-on voltages close to that of the neat host (Table 4.2), indicating that also in this case the device performance was influenced by the host matrix. However, in comparison to PIDT-2TPD devices, the PIDT-TPD devices showed less efficient quenching of the host emission and significantly lower EQE of 0.36%. The EQE

improved upon addition of the BTT\* molecule (for 0.5 and 1.0% blends) but remained below 0.5%. By considering the lower PLQY of PIDT-TPD host (5%) compared to PIDT-2TPD host (18%), the difference in the device performance is probably due to a higher density of nonradiative charge/exciton recombination centers or traps in the PIDT-TPD host compared to the PIDT-2TPD host.

In summary, NIR-OLEDs emitting at 840 nm with unprecedented EQEs exceeding 1.15% were obtained only through the design of a new matrix polymer PIDT-2TPD and a highly fluorescent NIR molecule BTT\* (PLQY 29%). PIDT-2TPD exhibits significantly improved characteristics if compared to previously reported matrices, such as F8BT, which has been a commonly used host for a number of NIR-OLEDs, despite its poor spectral overlap with the NIR molecule. For comparison, P2TTPD (see Chapter 4.1) was also used as a host in blend with BTT\*. P2TTPD provided good spectral overlap with BTT\* and pure NIR PL peaking at 840 nm, but the devices showed a complete lack of emission from BTT\* and the EL resembled that of the host. This is probably due to a relatively slow energy transfer in EL (the only active in PL) being overruled by charge trapping at P2TTPD and thereby dominant radiative and/or nonradiative decay from the host. Although such processes would require detailed study on the fluorescence lifetimes to assess the decay rates of the blend, similar observation with the random copolymers comprising small amount of BTT emitter (Chapter 4.1.3) further suggests that only the intrachain energy transfer and charge trapping was sufficient to ensure NIR EL. In contrast, PIDT-2TPD host and BTT\* molecule delivered highly functional devices, which are solution processable, emitting above 800 nm in the NIR, and the active layer is free of heavy/toxic metals. These properties are combined with the ability to operate the devices at high currents, while maintaining high EQEs and  $V_{ON}$  as low as 1.7 V, making the NIR-OLEDs appealing for application in light communication and wearable/biocompatible electronics.

## 5. Synthesis of Conjugated Polymers for NIR-LECs

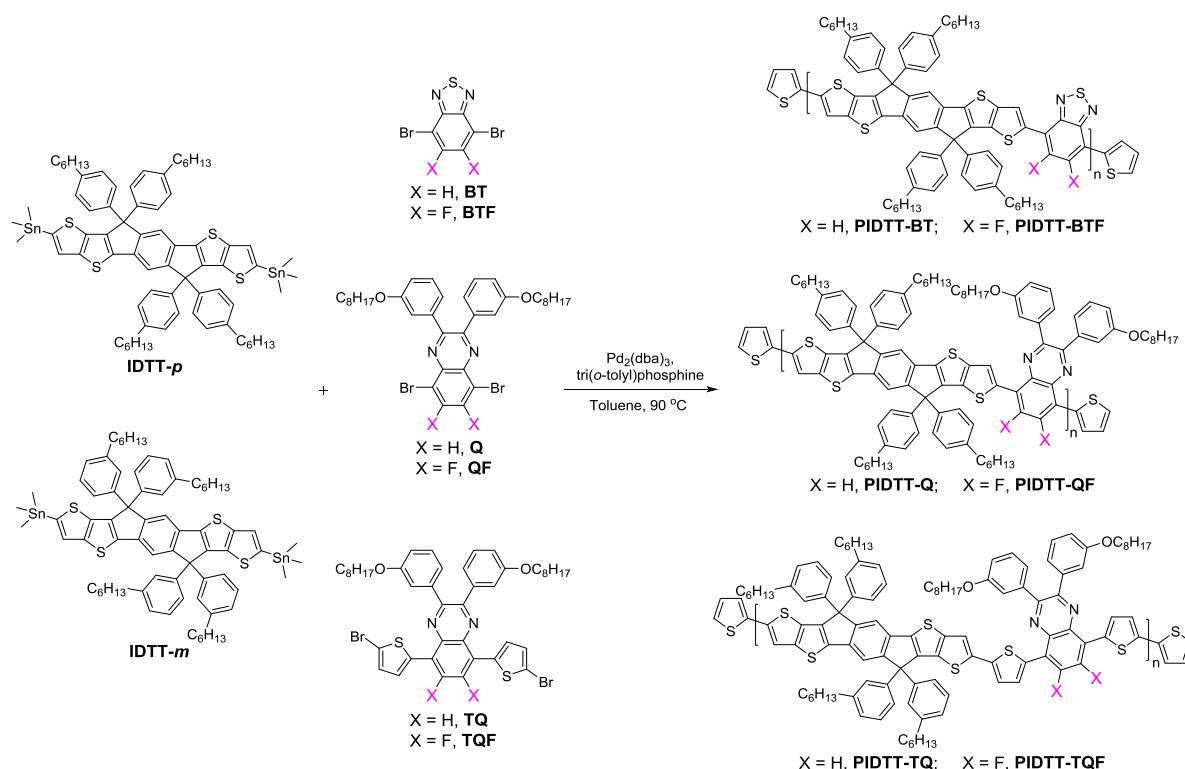
The previous chapter covered two different approaches to obtain efficient NIR emission in the solid state for high-performance NIR-OLED devices. An LEC differs from OLED in that the active layer contains an additional electrolyte salt, often referred to as an ionic liquid, which allows the device fabrication without the low-work function cathode metals that tend to be air-sensitive.<sup>[47,267,268]</sup> Such devices are attractive in that they can deliver high performance and high stability at low voltage and low fabrication cost through solution-processing.<sup>[10,269]</sup> In this chapter, polymeric NIR emitters are designed on the basis of donor–acceptor interactions in the polymer backbone for balanced redox processes and good electrochemical stability, as well as compatibility with the electrolyte for an ideal NIR-LEC performance, covering papers III and IV.

### 5.1. IDTT-Based Copolymer as the Single Emitter

#### 5.1.1. Background and Motivation

LEC offers a simplified device structure with the active layer sandwiched between two air-stable electrodes, which is ideal for scalable fabrication methods.<sup>[46,270,271]</sup> Despite this, only a few reports have been published so far on functional NIR-LECs. Pal et al.<sup>[272]</sup> used an Ir-complex as the emitter, which exhibited EL peaking at 705 nm with a relatively high radiance of 0.47 mW/cm<sup>2</sup>. The device performance was boosted with a 1 kHz pulsed driving current. Similarly, Pertegás et al.<sup>[273]</sup> applied a 1 kHz pulsed current to obtain a stable radiance of 0.17 mW/cm<sup>2</sup> peaking at 700 nm from a metal-free cyanine dye. Importantly however, for portable battery-driven applications the high-frequency power mode is not practical.<sup>[210]</sup> Bideh and Shahroosvand<sup>[203]</sup> obtained a luminance of 742 cd/m<sup>2</sup> at 690 nm from an LEC comprising a Ru-complex as the emitter, by driving the device at a constant current density of 222.4 mA/cm<sup>2</sup> (see Chapter 3.1 for different light intensity units). Unfortunately, the operational lifetime of the device was less than 20 min. It is highly desirable to design metal-free emitters for stable NIR performance. In this regard, copolymers comprising indacenodithieno[3,2-*b*]thiophene (IDTT) as the electron-rich donor, coupled with different electron-deficient acceptors, are synthesized and characterized for NIR-LEC devices, which show good operational stability – also under ambient air.

## 5.1.2. Polymer Design, Synthesis, and Characterization



Scheme 5.1. Synthesis of the IDTT-based copolymers.

The polymers were synthesized using monomers that were either commercially available or previously synthesized at Chalmers.<sup>[274-276]</sup> The polymerizations were carried out via Stille polycondensation of *p*-/*m*-hexylphenyl-substituted indacenodithieno[3,2-*b*]thiophene (IDTT-*p*/*m*) donor with one of the six acceptor monomers, as shown in Scheme 5.1 and listed below, to obtain six different D–A structured copolymers.

- PIDTT-BT: IDTT-*p* + benzo[*c*][1,2,5]thiadiazole (BT)
- PIDTT-BTF: IDTT-*p* + 5,6-difluorobenzo[*c*][1,2,5]thiadiazole (BTF)
- PIDTT-Q: IDTT-*p* + 2,3-diphenylquinoxaline (Q)
- PIDTT-QF: IDTT-*p* + 6,7-difluoro-2,3-diphenylquinoxaline (QF)
- PIDTT-TQ: IDTT-*m* + 2,3-diphenyl-5,8-di(thiophen-2-yl)quinoxaline (TQ)
- PIDTT-TQF: IDTT-*m* + 6,7-difluoro-2,3-diphenyl-5,8-di(thiophen-2-yl)quinoxaline (TQF)

**Table 5.1.** Physical and electrochemical characterization of the polymers.

polymer	$M_n$ (kg/mol)	PD	torsion, DFT ( $\varphi$ )	$E_g$ , DFT (eV)	$E_{opt}$ (eV)	$E_g$ , CV (eV)
PIDTT-BT	102.2	5.0	0.3	1.84	1.78	1.86
PIDTT-BTF	11.8	2.5	0.2	1.84	1.78	1.83
PIDTT-Q	33.2	2.9	6.8	1.99	1.80	2.04
PIDTT-QF	14.1	2.2	7.0	2.01	1.80	2.10
PIDTT-TQ	97.0	5.7	13.8	2.00	1.82	2.01
PIDTT-TQF	152.4	2.7	12.3	1.98	1.82	2.07

The IDTT donor was endowed with the bulky substituents to improve solubility and reduce  $\pi$ - $\pi$  stacking of the polymers in solid state, with the latter being associated with the undesired emission quenching, as discussed in previous chapter. BT and BTF are the smallest acceptors in this study, and they are distinguished by the replacement of two H atoms by two F atoms in the latter (colored pink in Scheme 5.1). Similarly, the two H atoms in Q and TQ acceptors are replaced by two F atoms in QF and TQF. The electron-withdrawing F atoms were expected to downshift the energy structure of the polymers and affect the intra/intermolecular hydrogen bonding. The bulky *m*-octyloxyphenyl substituents in Q, QF, TQ, and TQF were expected to introduce steric hindrance between the donor and acceptor, which would result in rotation of the polymer backbone and reduction of the  $\pi$ - $\pi$  stacking. Furthermore, the effect of proximity of the donor and acceptor units was studied with the two thiophene spacers in TQ and TQF. Lastly, the alkyl side chains of the hexylphenyl substituents on IDTT were changed from para to meta-position in PIDTT-TQ and PIDTT-TQF, since previous studies have shown that such side chain engineering can further reduce the polymer chain aggregation.<sup>[264,277]</sup>

Molecular weights of the polymers are listed in Table 5.1. The variation in  $M_n$  is probably due to the lower reactivity of the fluorinated BTF and QF acceptors in the Stille coupling with respect to their non-fluorinated counterparts BT and Q. The low reactivity can be due to steric reasons or possible competitive non-dissociative coordination of the F atoms to the Pd-catalyst (see Scheme 8.1, Chapter 8.1 for the generic catalytic cycle). Although this assumption cannot be directly supported by dedicated studies on Pd-catalyzed coupling reactions of fluorinated molecules,<sup>[278-280]</sup> the thiophene spacers in TQ and TQF seemed to cancel out such reactivity difference entirely. Nevertheless, it is important to note that all six polymers featured sufficient viscosity in solution for the deposition of uniform and pinhole-free thin films by spin-coating.

DFT calculations were employed to study the backbone torsion, the HOMO and LUMO energy levels, and the corresponding energy gaps of the polymers. The detailed methodology is described in Chapter 8.3. The addition of F atoms to the acceptor systematically downshifted the HOMO and LUMO levels by  $\sim 0.1$  eV, as expected, but it was not possible to discern any further effect on the polymer characteristics. Instead, the acceptor unit has a significant effect on the polymer conformation. The calculated backbone torsion ( $\varphi$ ) of the polymers are listed in Table 5.1. The BT and BTF acceptors both resulted in a highly coplanar conformation, whereas the Q and QF acceptors introduced torsion to the polymer backbone, and the TQ and TQF acceptors resulted in even larger torsion of  $12\text{--}14^\circ$ . Extensive calculations in paper III demonstrated that such backbone torsion indeed is a result of steric hindrance induced by simultaneous alkylation of the hexylphenyl substituents at the meta-position on IDTT, inclusion of the *m*-octyloxyphenyl substituents on the acceptor, and introduction of the thiophene spacers between the donor and the acceptor.

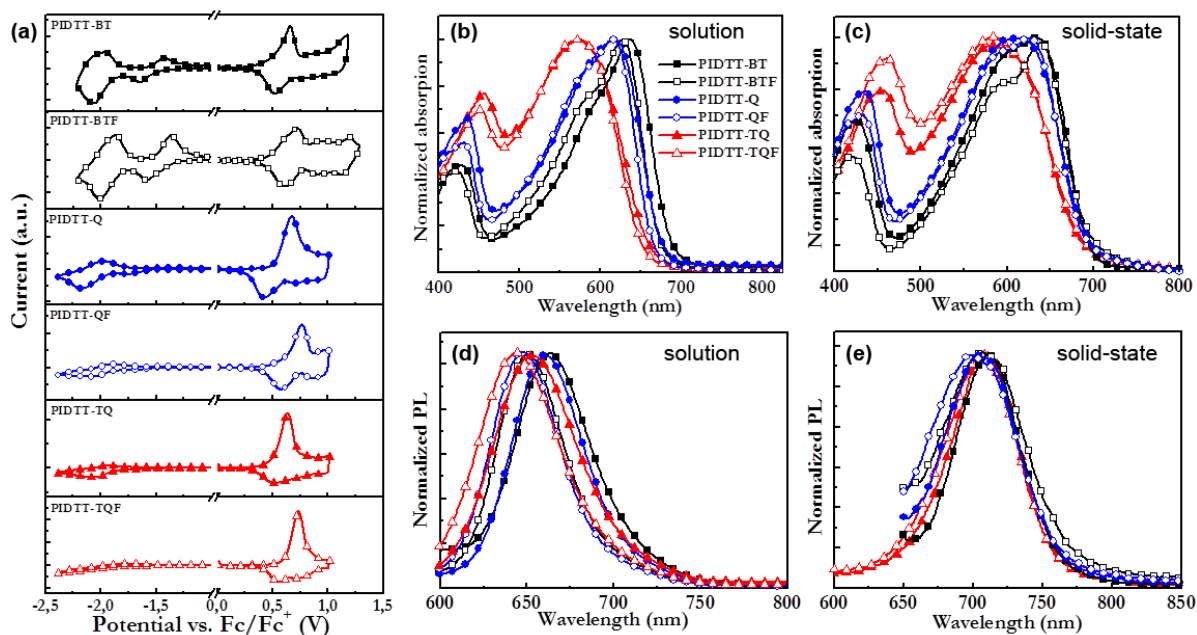


**Figure 5.1.** (a) CV traces of the IDTT-based copolymers at a scan rate of 100 mV/s. Absorption spectra of the polymers (b) in dilute toluene solution and (c) in solid-state thin film (80 nm). The corresponding PL spectra (d) in solution and (e) thin film. PL was measured by using a 540 nm excitation beam.

CV measurements were done out to study the electrochemical properties of the synthesized copolymers. As can be seen from Figure 5.1, all polymers exhibited reversible/quasi-reversible electrochemical oxidation (i.e., p-type doping), while the reduction (i.e., n-type doping) varied

substantially depending on the selection of the acceptor. PIDTT-BT and PIDTT-BTF featured most balanced p-type and n-type doping processes, while the capacity for n-type doping was markedly weaker in PIDTT-TQ and PIDTT-TQF. It is evident that the n-type doping capacity was, in general, weaker for the F-substituted polymers, as compared to the H-substituted ones. The CV results were in good agreement with the DFT calculations, as the addition of F atoms to the acceptor downshifted both the HOMO and LUMO of the polymers by ~0.1 eV (Figure 5.2a) and the energy gaps derived from DFT and CV were essentially identical (Table 5.1). Both DFT and CV indicated that PIDTT-BT and PIDTT-BTF exhibited the lowest energy gaps in this study, which is desirable regarding long-wavelength emission in the NIR.

The absorption and PL of the polymers in solution and thin film are presented in Figure 5.1b–e. In general, the addition of F atoms to the acceptor had a negligible effect on the absorption in both states. The only exception was PIDTT-BTF, which showed a slightly more structured absorption than PIDTT-BT, probably as a result of the increased ordering through hydrogen bonding. The PIDTT-BT/PIDTT-BTF pair exhibited the most redshifted absorption, as expected from the DFT calculations and CV characterization. The  $E_{\text{opt}}$  were determined from the low-energy absorption onsets in thin film, and the data are summarized in Table 5.1.

PIDTT-BT and PIDTT-Q exhibited the most redshifted emission in solution, as compared to the other four polymers, but the PL redshifted by ~50 nm in going from solution to thin film in all cases. This implies that some degree of aggregation was common in the solid state. The polymers featured relatively high PLQYs in solution, in the range of 14–34%, with the general observation being that the F-substituted polymers exhibited higher PLQYs compared to their H-substituted counterparts. However, the PLQYs dropped drastically in thin films, as the PIDTT-BT/PIDTT-BTF pair exhibited the lowest PLQYs of 0.9 and 0.4%, respectively, and the PIDTT-TQ/PIDTT-TQF pair the highest at 3.6% (Table 5.2). Such PL quenching further suggests that polymer chain aggregation was prominent in the solid state. Interestingly, the relative change in PLQY was smallest for PIDTT-TQ/PIDTT-TQF and largest for PIDTT-BT/PIDTT-BTF, which is in good agreement with the fact that aggregation-induced quenching of the PL increases with increasing planarity of the conjugated backbone.

## 5.1.3. Performance of the NIR-LECs

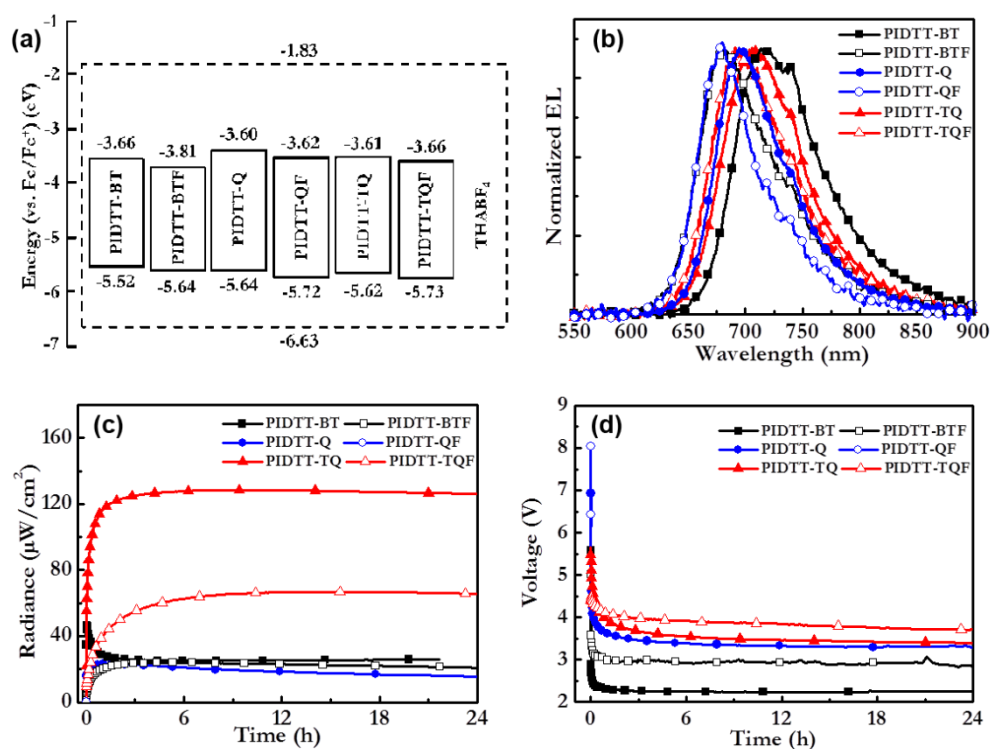


**Figure 5.2.** (a) Energy levels of the polymers and electrochemical window of THABF<sub>4</sub> electrolyte (dashed line), as derived from CV. (b) EL spectra of the NIR-LECs comprising the polymer:THABF<sub>4</sub> blend as the active layer. Temporal evolution of (c) the radiance and (d) the voltage of the same devices during one day of continuous operation. The devices were driven with a constant current density of  $J = 74.5 \text{ mA}/\text{cm}^2$ .

The NIR-LEC device characteristics are shown in Figure 5.2. The active layer was optimized by blending the NIR polymer and an electrolyte salt tetrahexylammonium tetrafluoroborate (THABF<sub>4</sub>) in 10:1 ratio (thickness 80 nm), which was sandwiched between the air-stable ITO/PEDOT:PSS anode and the Al cathode contact. For a stable LEC performance, it is fundamental that the electrolyte is electrochemically inert within the potential range of the p-type and n-type doping of the emissive polymer. Therefore, the HOMO and LUMO energy levels of the polymers are presented in Figure 5.2a with respect to the electrochemical stability window of THABF<sub>4</sub>, as derived from CV measurements, showing that the polymers can be electrochemically doped without interference from the electrolyte.

EL of the devices are peaked between 681–706 nm (Figure 5.2b, Table 5.2), which is 5–25 nm blueshifted with respect to their corresponding thin-film PL. The general observation is

that the F-substituted polymers exhibit blueshifted EL, by ~20 nm, as compared to their H-substituted counterparts. Figure 5.2c,d represent the typical characteristics of the NIR-LECs, i.e., the temporal evolution of the radiance and voltage during driving with a constant current density of  $J = 74.5 \text{ mA/cm}^2$ . All devices displayed well-functioning LEC operation, which can be seen as an increase of radiance and decrease of voltage with time during the initial turn-on process when the p–n junction doping structure is formed in the active layer. This is consistent with the fact that all polymers can be both p-type and n-type doped, albeit with differential doping capacities (Figure 5.1a), and that the active layer constituents were electrochemically stable. PIDTT-TQ delivered the highest radiance of  $0.13 \text{ mW/cm}^2$  (or  $129 \text{ }\mu\text{W/cm}^2$ , Table 5.2) at an EQE of 0.10%. The peak radiance was obtained at 705 nm and a steady-state driving voltage of 3.4 V. Thus far, this is the highest radiance reported for a metal-free NIR-LEC driven with a constant bias.

Results of the LECs performance are summarized in Table 5.2. The H-substituted polymers invariably delivered higher performance compared to the F-substituted ones, despite the fact that the PLQY in solid state was relatively independent of the substitution. The differential device performance is probably due to the polar character of the F-substituted polymers, which affected the compatibility with the THABF<sub>4</sub> electrolyte, and the hydrogen bonding induced by the F atoms, which hindered the electrolyte ion ingress during the p–n doping. Nevertheless, all NIR-LECs exhibited good stability. The radiance and voltage of PIDTT-TQ was essentially constant during one day of continuous operation under N<sub>2</sub> atmosphere (Figure 5.2c,d). The radiance output of a corresponding nonencapsulated device only dropped by 27% during one day of continuous operation under ambient air (reported in paper III).

**Table 5.2.** Optical properties and NIR-LEC device performance.

polymer	PLQY, film (%)	$R_{\text{MAX}}$ ( $\mu\text{W/cm}^2$ )	EQE (%)	$X_{\text{Ideal}}$ (factor)	EL peak (nm)
PIDTT-BT	0.87	47	0.038	0.88	706
PIDTT-BTF	0.42	24	0.018	0.85	681
PIDTT-Q	1.96	23	0.018	0.18	695
PIDTT-QF	2.75	16	0.009	0.07	679
PIDTT-TQ	3.60	129	0.10	0.56	705
PIDTT-TQF	3.59	67	0.050	0.28	690

The EQE of an LEC can be described by the following equation:

$$\text{EQE} = \eta_{\text{Rec}} \times \eta_{\text{ST}} \times \Phi_f \times \eta_{\text{Out}} \times X_{\text{Ideal}} \quad (5.1)$$

where  $\eta_{\text{Rec}}$  is the exciton formation efficiency,  $\eta_{\text{ST}}$  is the fraction of excitons formed as singlets, by spin statistics,<sup>[141,142]</sup>  $\Phi_f$  is the PLQY of the emissive polymer (Table 5.2), and  $\eta_{\text{Out}}$  is the outcoupling efficiency of the device, as described in Chapter 3.1 and Equation (3.1). Then, the additional losses due to various nonradiative decay processes, e.g., exciton–polaron, exciton–exciton, exciton–electrolyte, and exciton–electrode quenching, are presented by an ideality factor ( $X_{\text{Ideal}}$ ). The exciton quenching may be unfavorably induced by the high density of polarons in the p-type and n-type doping regions,<sup>[281]</sup> whereas exciton–exciton interactions can be expected as a large number of excitons is formed in the recombination zone. Impurities and defects in the active layer, related to quenching by the electrolyte and the electrodes, may cause further reduction of the radiative fraction.<sup>[208,282]</sup>

The  $X_{\text{Ideal}}$  of the devices were assessed to better understand the quality of the p–n junction doping structure. A well-functioning LEC ensures a stable recombination zone between the p-type and n-type doping regions and  $\eta_{\text{Rec}}$  close to unity,<sup>[282]</sup> which is confirmed by the stable device characteristics in Figure 5.2c,d. Thus, by setting  $\eta_{\text{Rec}}$  and  $\eta_{\text{ST}}$  to 1 and 0.25, respectively, and assuming that  $\eta_{\text{Out}}$  through the glass substrate/ITO anode is  $\sim 0.2$ ,<sup>[184,185]</sup> the  $X_{\text{Ideal}}$  could be calculated and the results are summarized in Table 5.2. Interestingly, the highest radiance and EQE were measured for PIDTT-TQ and PIDTT-TQF, but the highest  $X_{\text{Ideal}}$  was calculated for the devices comprising PIDTT-BT and PIDTT-BTF as the emitter. The latter two polymers exhibited the most balanced p- and n-type doping processes in the CV measurements, as shown in Figure 5.1a. Balanced electrochemical doping can be anticipated to result in a centered p–n junction in the NIR-LECs,<sup>[283]</sup> resulting in a minimal quenching of the excitons by the above discussed processes. The more balanced p- and n-type doping also explains the higher  $X_{\text{Ideal}}$  of the H-substituted polymers over their F-substituted counterparts. Obviously, an optimum NIR emitter should exhibit balanced electrochemical doping capacity for high  $X_{\text{Ideal}}$  and high solid-state PLQY for high-intensity emission.

In this study, polymeric NIR emitters were applied to LECs for the first time. A detailed study on IDTT-based donor–acceptor copolymers revealed that the choice of acceptor strongly affected the PLQY, solid-state aggregation, and electrochemical doping of the polymers. All these factors directly influenced the device performance. PIDTT-TQ delivered a record-high radiance of  $0.13 \text{ mW/cm}^2$  at 705 nm, while the device was operated at a low voltage of 3.4 V.

The excellent stability of the devices, also under ambient air, clearly highlights the benefits of using polymer-based emitters in NIR-LECs.

## 5.2. Random Copolymers Incorporating D–A–D Segments as the Emitter

### 5.2.1. Design of the Random Copolymers

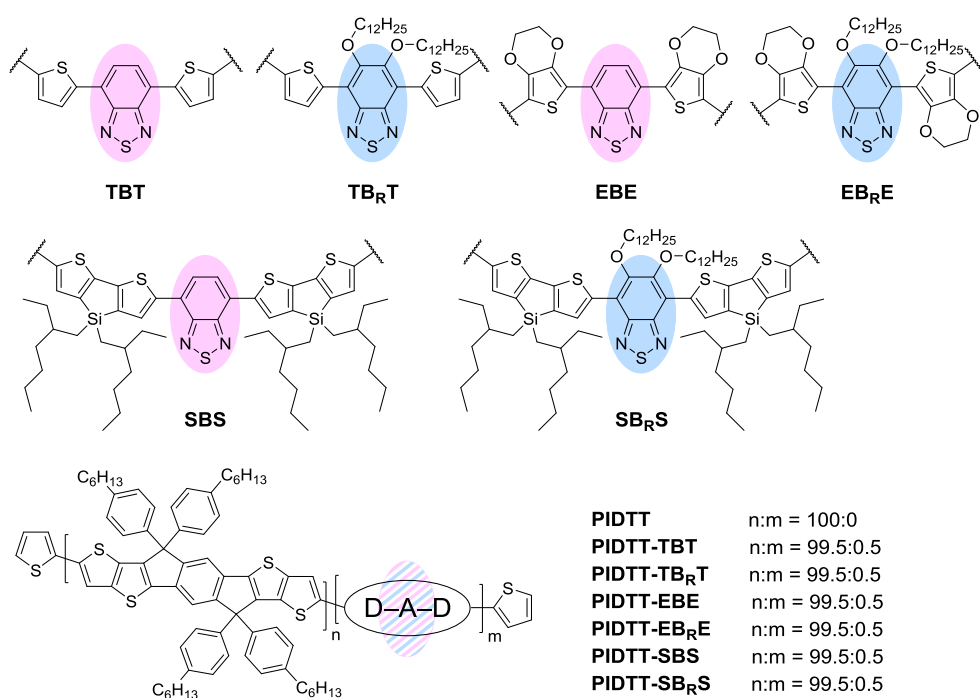
One significant observation in the previous chapter was that the solid-state PLQY of a NIR-emissive polymer could be improved by introducing thiophene spacers between the donor and acceptor units. On the other hand, the combination of IDTT donor and BT acceptor delivered balanced electrochemical doping processes, and thereby high  $X_{\text{Ideal}}$  from the NIR-LECs, with the emission peaking slightly beyond 700 nm. This chapter seeks to combine these properties, so as to obtain more intense and red-shifted emission, by using the same IDTT donor and BT acceptor but incorporating different electron-rich spacer units: either a small thiophene (T), a polar 3,4-ethylenedioxythiophene (E), or a large 4,4-bis(2-ethylhexyl)-4*H*-silolo[3,2-*b*:4,5-*b'*]dithiophene (S). Alkyloxy side chains were also introduced to the BT acceptor, giving rise to a total of six different donor–acceptor–donor (D–A–D) segments. Unlike the alternating copolymers in Chapter 5.1, in this case the D–A–D segments were incorporated only in a low concentration (0.5%) into the IDTT host polymer backbone, as guest emitters. Motivated by the earlier work in Chapter 4, dilution of the NIR emissive centers within the polymer matrix is expected to reduce the aggregation-induced luminescence quenching.

### 5.2.2. Material Synthesis and Characterization

The chemical structures and abbreviations of the six different D–A–D segments are presented in the upper and middle part of Scheme 5.2. For the central acceptor was employed either BT (indicated by purple color) or its 5,6-bis(dodecyloxy)-substituted analogue (indicated by blue color), here abbreviated as B and B<sub>R</sub>, respectively. The three donor units T, E, and S were selected on the merit of their differential electron-donating strength and conformation when coupled with the acceptors,<sup>[82]</sup> which is expected to tune the D–A–D emission wavelength.

The detailed synthesis routes for the D–A–D segments are presented in Scheme A1 of the Appendix. The key step involved coupling of the donor (T, E, or S) with the 4,7-dibromo-substituted acceptor (B or B<sub>R</sub>). EBE and EB<sub>R</sub>E were synthesized in satisfactory yields by direct arylation coupling reaction, using pivalic acid as an additive, thanks to the high reactivity of

the E donor at the 2- and 5-positions.<sup>[284-288]</sup> To prevent copolymerization with the acceptor monomer, the E donor monomer was used in excess. However, the remaining starting material could be collected by column chromatography and reused. Similar reaction conditions resulted in significantly lower yields for the other four D–A–D structures, and they were instead synthesized via Pd-catalyzed Stille coupling of the acceptor (B or B<sub>R</sub>) and the monostannylated (T or S) donor monomer. DFT calculations in paper IV indicated that five of the D–A–D segments (TBT, TB<sub>R</sub>T, EBE, SBS, and SB<sub>R</sub>S) featured a flat conformation with a small average torsion angle of  $\varphi = 0\text{--}8^\circ$  between the donor and acceptor units, while EB<sub>R</sub>E displayed a highly twisted conformation with  $\varphi = 47^\circ$ .



**Scheme 5.2.** Chemical structures of the D–A–D units and the corresponding copolymers.

The chemical structures and abbreviations of the polymers are presented in the lower part of Scheme 5.2. Poly[indacenodithieno[3,2-*b*]thiophene-2,8-diyl] (PIDTT) host is anticipated to facilitate an efficient charge transport due to its planar backbone,<sup>[289-291]</sup> and DFT calculations in paper IV further confirmed an average torsion of  $\varphi = 10^\circ$  between the IDTT repeating units. PIDTT was synthesized via Pd-catalyzed Stille polycondensation of the bis(trimethylstannyl)-substituted IDTT monomer and dibromo-substituted IDTT monomer, as shown in Scheme A2 of the Appendix. The random copolymers incorporating the six different guest emitters were synthesized by replacing small amount of the dibromo-substituted IDTT monomer with the dibromo-substituted D–A–D monomer, so as to include 0.5% of D–A–D

in the polymer, based on the initial molar feed. All of the synthesized polymers featured high  $M_n > 100$  kg/mol (Table 5.3), which is highly relevant in terms of ensuring that majority of the polymer chains contained a D–A–D emitter (see Chapter 4.1.3 for related discussion).

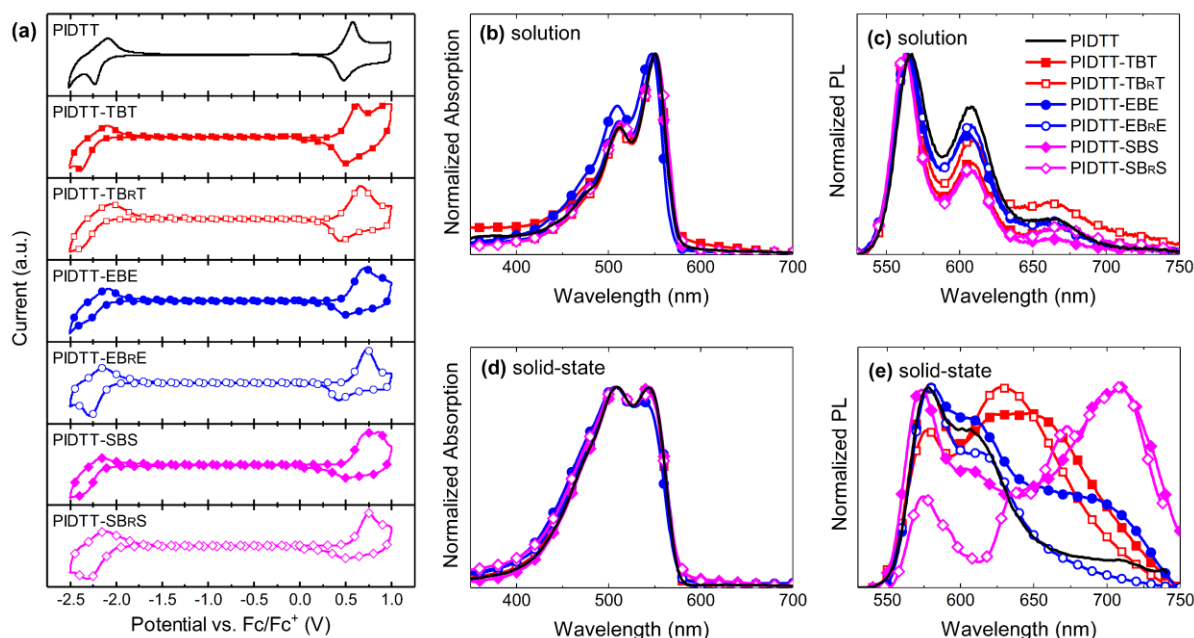


**Figure 5.3.** (a) CV traces of the polymers at a scan rate of 100 mV/s. (b) Absorption and (c) PL spectra of the polymers in dilute toluene solution. The corresponding (d) absorption and (e) PL spectra in thin film (100 nm). PL was measured with a 510 nm excitation beam.

Electrochemical properties of the individual D–A–D monomers and the copolymers were studied by CV measurements, and the results of the latter are shown in Figure 5.3a. The CV-derived energy gaps of the D–A–D segments were invariably lower than that of the PIDTT homopolymer (2.55 eV). Therefore, exciton recombination is anticipated to occur selectively at the low-gap emitter in the random copolymers. The SBS and SBRS monomers exhibited the lowest energy gaps of 2.11 and 2.35 eV, respectively. The CV of the random copolymers incorporating the D–A–D segments (colored lines) resembled that of the PIDTT homopolymer (black line), as expected, since the polymers were composed 99.5% of IDTT host and only 0.5% of the guest emitter. Nevertheless, all of the polymers displayed reversible/quasi-reversible oxidation and reduction processes, thereby indicating balanced p-type and n-type doping capacities. Space-charge-limited current (SCLC) mobility measurements in paper IV demonstrated that PIDTT featured two orders of magnitude higher hole mobility ( $5.5 \times 10^{-4}$  cm<sup>2</sup> V<sup>-1</sup> s<sup>-1</sup>) than electron mobility ( $1.4 \times 10^{-6}$  cm<sup>2</sup> V<sup>-1</sup> s<sup>-1</sup>).

Absorption spectra of PIDTT and the random copolymers in solution and solid-state thin films are presented in Figure 5.3b,d, respectively. The absorption profiles of the copolymers were essentially identical to that of the PIDTT homopolymer in both solution and solid state, which is ascribable to low D–A–D concentration. The major difference was the 0–0 transition at ~550 nm being more prominent than the 0–1 transition at ~510 nm in solution, whereas in the solid state the two peaks appeared similar in magnitude.

PL of the corresponding solutions and thin films are shown in Figure 5.3c,e, respectively. PL spectra of the copolymers were highly reminiscent of that of PIDTT homopolymer in solution (Figure 5.3c), although the PLQY increased slightly, from 47% (for PIDTT) to 50–57% (for the copolymers) upon incorporation of the guest emitter. Assuming that the polymer chains were well-separated in the dilute solution, the lack of additional low-energy PL peak clearly implies that the intramolecular energy transfer to the D–A–D emitter within a single polymer chain was inefficient.

The PL behavior was markedly different when going from solution to the solid-state (Figure 5.3e). PIDTT displayed slightly less structured PL in the solid state, as compared to the PL in solution, and the PLQY dropped from 47% in solution to 2.8% in thin film (Table 5.3). The latter observation must be related to significant intermolecular interactions in the solid state, which is consistent with the DFT calculations, as PIDTT adopts a flat conformation that allows dense and ordered stacking in the solid state. Four of the random copolymers (PIDTT-TBT, PIDTT-TB<sub>R</sub>T, PIDTT-SBS, and PIDTT-SB<sub>R</sub>S) featured a drastic change in the PL shape and smaller drop in the PLQY during the transition from solution to solid state. It is likely that the random copolymers experience similar significant intermolecular interactions and stacking in the solid state as the PIDTT homopolymer. However, the differential PL spectra and the higher PLQY in the solid state indicate that the close-packing of the polymers opened a new channel for intermolecular energy transfer from the IDTT host to the low-gap D–A–D sites. The PL of PIDTT-EBE and PIDTT-EB<sub>R</sub>E were more reminiscent of the PL of the PIDTT homopolymer, especially in the case of the latter polymer, which can be explained by the observation that the EB<sub>R</sub>E segment adopts a highly twisted conformation. Presumably, the twisted structure is not compatible with the flat PIDTT backbone, and consequently the host-to-guest energy transfer is suppressed also in the solid state. In terms of NIR emission, it is notable that PIDTT-SBS and PIDTT-SB<sub>R</sub>S delivered the most redshifted PL in the solid state, peaking at 709 nm. This is consistent with the lowest CV energy gaps measured for the SBS and SB<sub>R</sub>S monomers.

## 5.2.3. Performance of the NIR-LECs

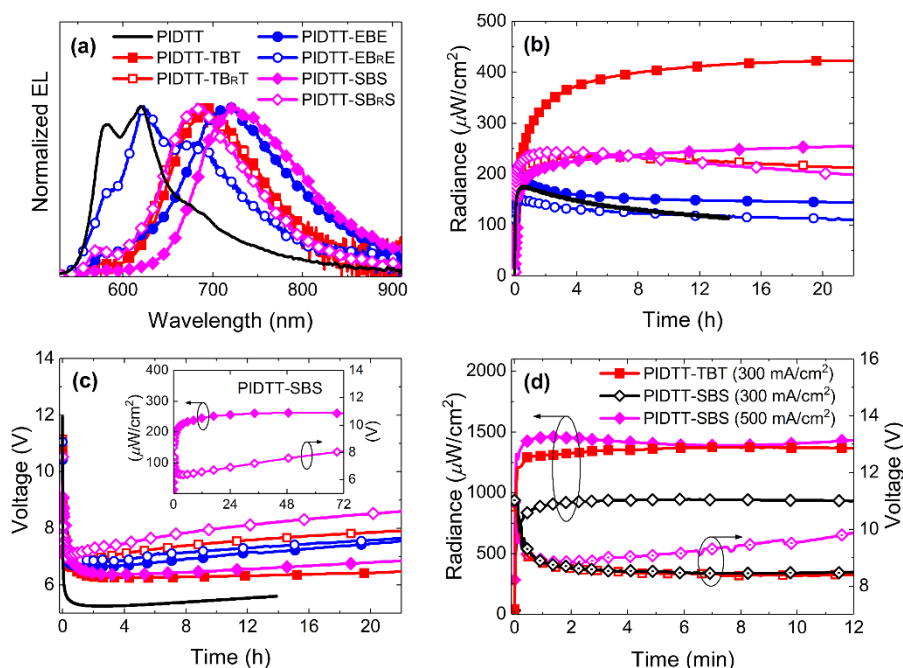
**Table 5.3.** Physical properties and NIR-LEC device performance.

polymer	$M_n$ (kg/mol)	PD	PLQY, film (%)	$J$ (mA/cm <sup>2</sup> )	turn- on (s)	$R_{MAX}$ ( $\mu$ W/cm <sup>2</sup> )	EQE (%)	EL peak (nm)
PIDTT	137.5	3.1	2.8	74.5	27	177	0.12	580, 620
PIDTT- TBT	208.9	2.9	6.6	74.5	116	422	0.30	694
				300	2	1372	0.24	694
PIDTT- TB <sub>R</sub> T	235.4	2.6	9.4	74.5	195	235	0.18	692
PIDTT- EBE	102.8	3.2	2.8	74.5	7	208	0.17	720
PIDTT- EB <sub>R</sub> E	108.6	3.8	3.0	74.5	20	152	0.11	621, 675
PIDTT- SBS	140.3	3.7	4.4	74.5	540	263	0.21	725
				300	2	944	0.19	724
				500	1	1458	0.17	725
PIDTT- SB <sub>R</sub> S	207.1	2.6	5.4	74.5	3	248	0.18	690

The NIR-LEC device characteristics are summarized in Table 5.3 and further illustrated in Figure 5.4. The active layer comprised a blend of the polymer and the THABF<sub>4</sub> electrolyte, sandwiched between ITO/PEDOT:PSS anode and Al cathode. The devices were optimized for efficient and strong NIR emission, and the best performance was obtained with an electrolyte concentration of 5 w-% and an active layer thickness of 100 nm.

Figure 5.4a presents the steady-state EL spectra of the devices, when driven with a constant current density of  $J = 74.5$  mA/cm<sup>2</sup>. The PIDTT device displayed an EL spectrum that is highly reminiscent of the solid-state PL spectrum (Figure 5.3e), peaking at 620 nm, but with a tail extending far in the NIR region. From the random copolymers, only PIDTT-EB<sub>R</sub>E exhibited an EL spectrum (open blue circles) that is dominated by the emission from IDTT host. This can be rationalized by that the twisted conformation of the EB<sub>R</sub>E segment hindered both the energy transfer from the host to the guest emitter and the direct charge trapping at the low-gap EB<sub>R</sub>E sites. The five other random copolymers featured highly redshifted and featureless EL

spectra, as compared to their corresponding PL in the solid state, and more than 50% of the photons were emitted in the NIR region. The device based on PIDTT-SBS exhibited the most redshifted EL peaking at 725 nm, as expected from the lowest energy gap measured for the SBS monomer. Interestingly, also PIDTT-EBE featured a similar EL centered at 720 nm. The general observation is that the high-energy emission component peaking below 600 nm, as observed for all polymers in the solid-state PL (Figure 5.3e), was almost completely quenched in the EL spectra. This indicates that charge trapping at the NIR-emissive D–A–D segment must have been efficient during the LEC operation, with the only exception being the PIDTT-EB<sub>R</sub>E device. Such good spectral purity with only 0.5% D–A–D feed can be addressed to the planar conformation of the five guest units (TBT, TB<sub>R</sub>T, EBE, SBS, and SB<sub>R</sub>S) and to the high  $M_n$  of the polymers that ensured incorporation of the emitter in majority of the polymer chains. Moreover, the EL remained unchanged throughout the measurement period, i.e., 14 h for the PIDTT device and 24–72 h for the other devices.



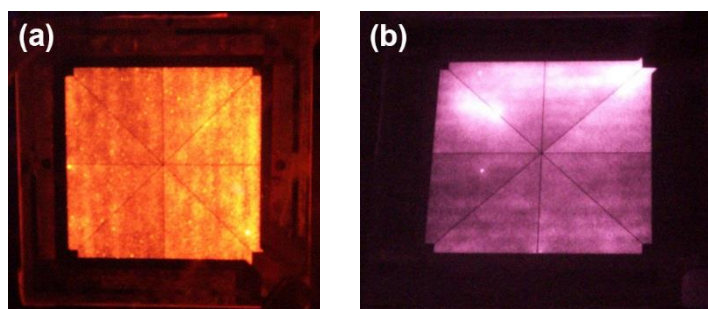
**Figure 5.4.** (a) EL spectra of the NIR-LECs comprising the polymer:THABF<sub>4</sub> blend as the active layer, driven with a constant current density of  $J = 74.5 \text{ mA/cm}^2$ . Temporal evolution of (b) the radiance and (c) the voltage of the same devices during the first day of continuous operation. The inset in (c) displays the extended operation of the PIDTT-SBS device. (d) The temporal evolution of the PIDTT-TBT and PIDTT-SBS devices at a higher current density.

Figure 5.4b,c presents the increase of radiance and decrease of voltage of the LECs during the initial turn-on process, thereby confirming that all polymers can be p- and n-type doped and that the p–n junction is formed *in situ* in the active layer. The turn-on time to a radiance of  $100 \mu\text{W}/\text{cm}^2$  was only a few seconds for the PIDTT-EBE, PIDTT-EB<sub>RE</sub>, and PIDTT-SB<sub>RS</sub> devices, while the other three NIR-LECs turned on in a minute range (Table 5.3). However, a second-fast turn-on could be obtained for all devices simply by ramping up the drive current. LECs with a 10 w-% electrolyte concentration were also tested in paper IV, and the devices in general exhibited faster turn-on, but they consistently showed a lower radiance and EQE than those reported in Table 5.3. This is probably due to an increased exciton–polaron quenching (see the related discussion in Chapter 5.1.3). For a general interest, OLEDs comprising the same NIR-emissive polymers without the electrolyte were fabricated, with the device structure of ITO/PEDOT:PSS/polymer/Ca/Al. These OLEDs invariably featured a lower radiance and EQE compared to the LECs, presumably because of the hole-dominated transport within the IDTT host, which led to a positioning of the recombination zone close to the cathode, and thus severe exciton–electrode quenching. Such defects were effectively eliminated in the optimized LECs, where the p- and n-type doping regions contained the excitons to the p–n junction.

In terms of NIR performance, the highest radiance of  $0.42 \text{ mW}/\text{cm}^2$  (or  $422 \mu\text{W}/\text{cm}^2$ , Table 5.3) and EQE of 0.30% at  $J = 74.5 \text{ mA}/\text{cm}^2$  was obtained from the PIDTT-TBT device, while the PIDTT-TB<sub>RT</sub>, PIDTT-SBS, and PIDTT-SB<sub>RS</sub> devices also delivered impressive radiances of  $\sim 0.25 \text{ mW}/\text{cm}^2$  at the same current. Thanks to the electrochemical stability of the polymers, it was possible to increase the current and record very high radiance values of  $1.4 \text{ mW}/\text{cm}^2$  at  $J = 300 \text{ mA}/\text{cm}^2$  from the PIDTT-TBT device and  $1.5 \text{ mW}/\text{cm}^2$  at  $J = 500 \text{ mA}/\text{cm}^2$  from the PIDTT-SBS device (Figure 5.4d). These are the highest radiance values reported from metal-free NIR-LECs.

Overall, copolymers based on the B acceptor delivered higher radiances at lower voltages than the copolymers comprising the dodecyloxy-substituted B<sub>R</sub> acceptor. Incorporation of the T and S donor units in the copolymer improved the device performance over the copolymers bearing the E donor. The most efficient NIR-LECs were also observed to be the most stable during a long-term operation. As shown in the inset of Figure 5.4c, the radiance output from the PIDTT-SBS device remained constant at  $0.26 \text{ mW}/\text{cm}^2$  during three days of continuous operation at a  $J = 74.5 \text{ mA}/\text{cm}^2$ . The device also exhibited a close to unity  $X_{\text{Ideal}}$  of 0.95, as

calculated by using Equation (5.1) in the previous chapter, which further indicates a stable and well-balanced doping structure.



**Figure 5.5.** Photograph of a ( $6.7 \times 6.7$  cm) large-area NIR-LEC comprising PIDTT-SBS during emission, recorded (a) with no filter and (b) through a  $\lambda < 800$  nm cutoff filter.

One major advantage of polymer-based NIR emitters is that they are highly fit for a scalable and low-cost solution processing. Motivated by this, a large-area NIR-LEC of a size of  $6.7 \times 6.7$  cm ( $\sim 45$  cm<sup>2</sup>) was fabricated by spray-coating under ambient air,<sup>[10,292]</sup> using a blend of PIDTT-SBS and THABF<sub>4</sub> as the active material at a thickness of 200 nm. Emission of the device, as driven by a low constant voltage of 4.5 V, is shown in Figure 5.5a. In Figure 5.5b, the same device is photographed through a cutoff filter that allows only wavelengths longer than 800 nm to pass through. The low-voltage driven large-area NIR-LEC featured a strong and uniform emission peaking at 725 nm.

In summary, random copolymers comprising IDTT as the host and six different D–A–D units as the guest emitter featured balanced electrochemical p- and n-type doping capacities, which ensured functional NIR-LEC operation with *in situ* p–n junction doping formation. The intermolecular energy transfer and direct charge trapping at the emitter functioned efficiently, given that the emitter was compatible with the planar host polymer backbone. An optimized LEC based on PIDTT-SBS as the emitter featured a fast turn-on and good long-term stability, a low voltage of 6 V, strong NIR emission peaking at 725 nm with a radiance of 1.5 mW/cm<sup>2</sup>, and a stable EQE of 0.2% also at high currents. Importantly, PIDTT-SBS was also applicable to a solution-based fabrication of a large-area NIR-LEC.

## 6. Application of Conjugated Polymers for OPDs

It is important and appealing to study the characteristics and possible applications of the newly synthesized materials in a broad perspective. For example, the matrix polymers used in light-emitting devices commonly show excellent charge transport properties, which is of significant importance also in the light-harvesting applications. In OPDs, the photogenerated charges are extracted in the external bias, and charge transport in the active layer ultimately defines the response rate of the device.<sup>[64,293,294]</sup> Conjugated polymers are attractive photoactive materials for OPDs, since their spectral response and transport properties can be tuned with subtle changes in the polymer structure, depending on the target application.<sup>[69,70]</sup> PIDT-TPD and PIDT-2TPD delivered good performance in NIR-OLEDs, as discussed in Chapter 4.2, but the two polymers showed very different optical and electronic properties. In this chapter, PIDT-TPD and PIDT-2TPD are used in two different types of OPD devices, both delivering high performance, and covering papers V and VI.

### 6.1. High-Speed OPDs Based on PIDT-TPD Donor Polymer

#### 6.1.1. Aim at High Performance

The frontier orbital energy levels and absorption wavelength of D–A structured polymers are commonly tuned by changing the backbone planarity and conjugation structure, and a range of different electron-rich donor and electron-deficient acceptor units have been developed for this purpose.<sup>[75,81,295]</sup> In general, polymers incorporating IDT as the donor have shown strong light absorption and high charge mobilities in organic photovoltaic (OPV) and organic field-effect transistor (OFET) applications.<sup>[296-300]</sup> The rigid and planar backbone of the IDT-based polymers ensured strong intermolecular interactions in the solid state, which further facilitated high charge mobilities. Hence, PIDT-TPD was considered a promising candidate for solution-based fabrication of fast-response OPDs as well.

Previously, OPDs have been reported with high 3 dB bandwidth cutoff frequencies up to 50 MHz in the visible and NIR regions, but the dark current density  $J_d$  values at high reverse bias were not lower than the order of  $10^{-6}$  A/cm<sup>2</sup> (i.e.,  $\mu$ A/cm<sup>2</sup>).<sup>[66,72,301]</sup> Although the  $J_d$  of OPDs has been further reduced down to the order of  $10^{-9}$  A/cm<sup>2</sup> (i.e., nA/cm<sup>2</sup>),<sup>[64,293,294]</sup> the EQEs of the devices were not higher than 30%. The  $J_d$  and EQE are the two main factors that limit the sensitivity of the OPDs. Therefore, it is of crucial importance for the copolymers that

they deliver high performance by keeping simultaneously a low  $J_d$ , high EQE, and high speed even at low irradiance power. These are the ideal properties for imaging and communication applications. Apart from the polymer structure, also the BHJ morphology plays an important role in the device performance. An interpenetrating network of the donor and acceptor material should ensure efficient exciton dissociation and successful charge extraction at the electrodes. The BHJ morphology is greatly affected by the donor/acceptor blend ratio, concentration, and interactions of the two materials with each other.<sup>[62,302]</sup> In this study, PIDT-TPD is used as the donor and [6,6]-phenyl-C<sub>61</sub>-butyric acid methyl ester (PC<sub>61</sub>BM) as the acceptor, which blend delivered high-performing OPDs in terms of low  $J_d$ , high EQE, and high cutoff frequency.

### 6.1.2. Characterization of the PIDT-TPD/PCBM Blend

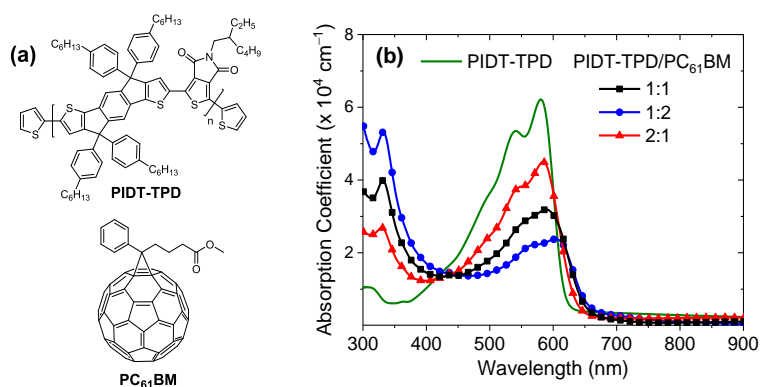


**Figure 6.1.** (a) Chemical structures of PIDT-TPD and PC<sub>61</sub>BM. (b) Absorption coefficients of the neat polymer and PIDT-TPD/PC<sub>61</sub>BM blends, as measured in thin films.

PIDT-TPD was synthesized according to the procedure described earlier in Chapter 4.2, and collected with a  $M_n$  of 27.0 kg/mol (PD 2.7), referred to as a medium  $M_n$  polymer in paper V. Figure 6.1 shows the chemical structures of PIDT-TPD and PC<sub>61</sub>BM, as well as the absorption coefficient versus wavelength curves of the neat polymer (green line) and PIDT-TPD/PC<sub>61</sub>BM blends in 1:1 (black squares), 1:2 (blue circles), and 2:1 (red triangles) ratio. For PIDT-TPD, an  $E_{opt}$  of 2.0 eV was estimated from the low-energy onset of absorption in thin film. The polymer exhibited a peak maximum at 580 nm, but addition of PC<sub>61</sub>BM to the blend revealed another absorption band peaking at 332 nm. All blends exhibited a complementary absorption ranging from 300 to 650 nm, but the relative contribution of PIDT-TPD and PC<sub>61</sub>BM to the absorption spectrum varied according to their respective concentration.

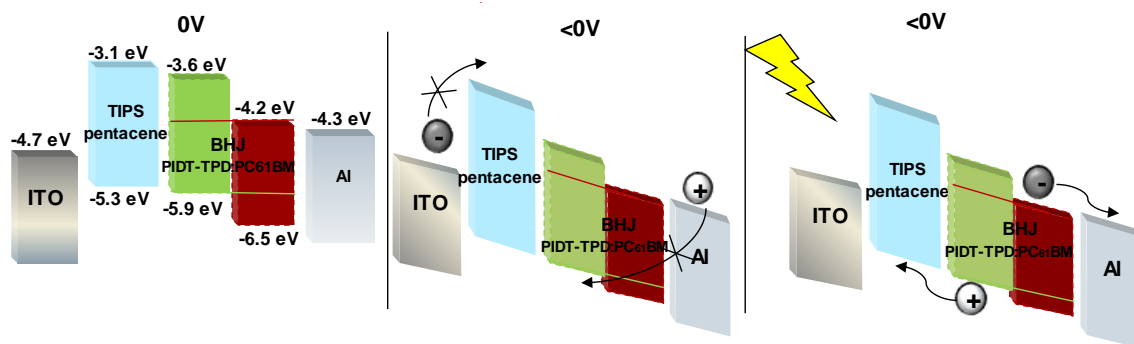


**Figure 6.2.** Energy levels of PIDT-TPD (green) and PC<sub>61</sub>BM (red), as derived from CV, and working mechanism of the OPD in dark (left panel), in dark at reverse bias (middle panel), and under illumination at reverse bias (right panel).

Energy levels of PIDT-TPD and PC<sub>61</sub>BM were determined with CV measurements. PIDT-TPD was chosen as the donor because it exhibited relatively high HOMO and LUMO energy levels with respect to the PC<sub>61</sub>BM acceptor. The HOMO–HOMO and LUMO–LUMO offsets were both 0.6 eV, as shown in the left panel of Figure 6.2. Without a doubt, this facilitates an efficient exciton separation in the BHJ. PL measurements of the PIDT-TPD/PC<sub>61</sub>BM blends in paper V further indicated their suitability as the photoactive layer, since the strong emission of PIDT-TPD was completely quenched in all three blends.

Morphological characterization of the blends was carried out with atomic force microscopy (AFM, Figure 6.3a-c) and transmission electron microscopy (TEM, Figure 6.3d-f). The PIDT-TPD/PC<sub>61</sub>BM 2:1 blend (Figure 6.3a,d) exhibited a smooth surface with a root mean square (RMS) roughness of 1.12 nm. The 1:1 blend (Figure 6.3b,e) had more uniform phase domain distribution and lower RMS surface roughness of 0.79 nm. In contrast, the 1:2 blend (Figure 6.3c,f) presented a substantially different morphology with a high RMS roughness of 4.10 nm and visible aggregates in large isolated domains. Further morphological characterization with dynamic mechanical thermal analysis (DMTA) in paper V revealed a thermal transition in the 1:2 blend that is ascribable to a substantial crystallization of the PC<sub>61</sub>BM-rich phase. The 2:1 blend lacked such transition completely, suggesting that PC<sub>61</sub>BM was fully dispersed in the BHJ without desirable phase separation. However, the 1:1 blend showed thermal transitions evident from both the polymer-rich (2:1) and the PC<sub>61</sub>BM-rich (1:2) blend, which tentatively indicates an ideal degree of phase separation in the 1:1 blend for an efficient charge transport in the OPD devices.

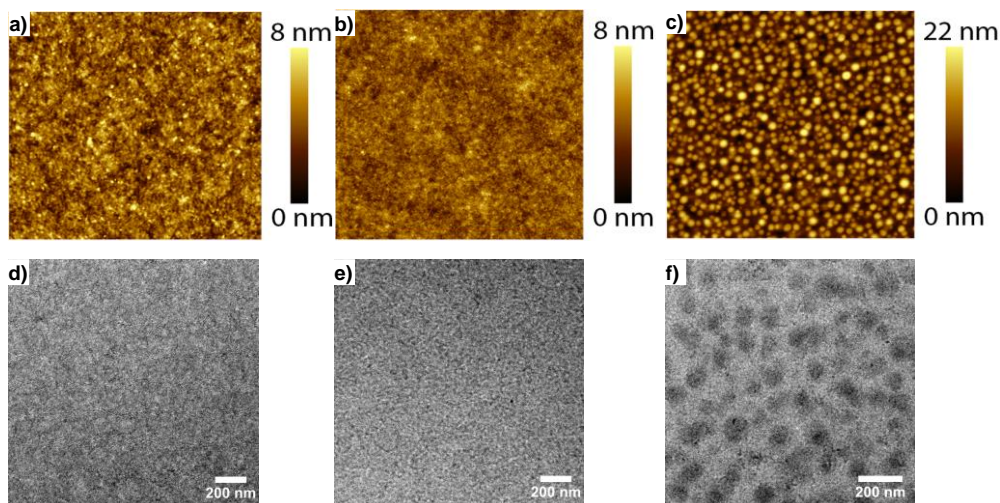


**Figure 6.3.** Tapping mode AFM topography images ( $5 \times 5 \mu\text{m}$ ) of the PIDT-TPD/PC<sub>61</sub>BM blend films in (a) 2:1 ratio, (b) 1:1 ratio, and (c) 1:2 ratio. Bright-field TEM images of the corresponding blend films in (d) 2:1, (e) 1:1, and (f) 1:2 ratio.

### 6.1.3. Performance of the OPDs

Figure 6.2 illustrates the OPD device architecture and performance in dark conditions at 0 V (left panel), in dark at reverse bias (middle panel), and under illumination at reverse bias (right panel). The BHJ comprising the blend of PIDT-TPD/PC<sub>61</sub>BM was sandwiched between the ITO/interlayer and the Al contact. In this study, 6,13-bis(triisopropylsilylethynyl)pentacene (TIPS pentacene) was selected as the interlayer because of its relatively high LUMO energy level of  $-3.1$  eV, which makes it an electron blocking layer that effectively reduces the  $J_d$  of the OPDs at reverse bias (see Figure 6.2, middle panel), as reported earlier by Montenegro Benavides et al.<sup>[303]</sup> Under illumination, the photogenerated electrons and holes are driven by the external bias and thereby drifted to the respective electrodes (see Figure 6.2, right panel).

Typical optoelectronic characterization of the OPDs is shown in Figure 6.4a,b and the most relevant device characteristics are summarized in Table 6.1. The best performance is obtained with the PIDT-TPD/PC<sub>61</sub>BM 1:1 blend, as expected at this stage. The device exhibited a very low  $J_d$ , which remained stable at  $1 \text{ nA/cm}^2$  even at a high reverse bias of  $-5 \text{ V}$  (Figure 6.4a). The corresponding device also delivered a high EQE of 52% at 610 nm in the far-orange/red spectral region (Figure 6.4b). Importantly, maintaining a high performance at high reverse bias ( $-5 \text{ V}$ ) is desired for the integration of the OPD as the light-sensitive component into real-life imaging and communication applications.<sup>[69,304]</sup>

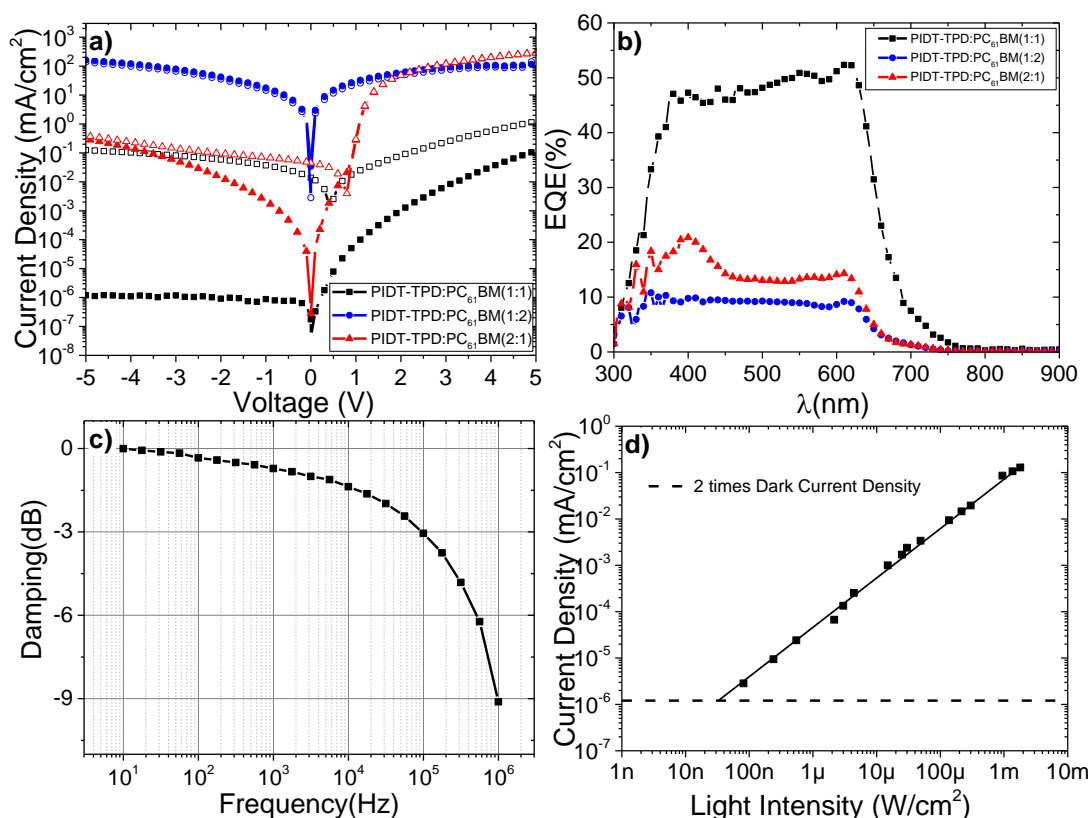


**Figure 6.4.** (a)  $J$ - $V$  characteristics of the OPDs comprising PIDT-TPD/PC<sub>61</sub>BM blend in 1:1 (black squares), 1:2 (blue circles), and 2:1 ratio (red triangles) in the dark (solid symbols) and under green light at 532 nm at 780 μW/cm<sup>2</sup> (open symbols). (b) EQE of the devices. (c) Frequency response of the device comprising the 1:1 blend, as driven at -5 V. (d) Linearity plot of the device comprising 1:1 blend under different intensities of green light at 532 nm.

The device based on the 2:1 blend had a much higher  $J_d$  (290 μA/cm<sup>2</sup>) and only a negligible photocurrent as compared to the optimal 1:1 blend, while the 1:2 blend led to electrical short circuits. Also the EQEs obtained from the latter two blends were consistently lower than that of the 1:1 blend. These results are in line with the morphological characterization. The absence of well-interconnected domains in the 2:1 blend and the presence of large agglomerates in the 1:2 blend clearly suppressed the charge separation and transport in the BHJ. SCLC mobility measurements in paper V further confirmed that the 1:1 blend exhibited the highest and most balanced electron ( $\mu_e$ ) and hole mobility ( $\mu_h$ ) from the three different blends (see Table 6.1).

Figure 6.4c presents the frequency response of the best performing device based on PIDT-TPD/PC<sub>61</sub>BM 1:1 blend, and the average 3 dB cutoff frequency at -5 V bias was recorded at 100 kHz. This is an impressive value for a red (610 nm) OPD, although the cutoff frequencies

reported for other polymer-based OPDs have reached the order of MHz.<sup>[66,72,301]</sup> However, the PIDT-TPD/PC<sub>61</sub>BM 1:1 blend exhibited a low  $J_d$  of 1 nA/cm<sup>2</sup> even at high reverse bias of –5 V, thereby outperforming the devices presented previously.<sup>[64,66,72,293,294,301]</sup> The detectivities of the devices were calculated using Equation (3.7) in Chapter 3.3, given the assumption that the noise was dominated by the shot noise from dark current.<sup>[59]</sup> Thanks to the low  $J_d$  of the OPD comprising the 1:1 blend, a high  $D^*$  of  $1.44 \times 10^{13}$  Jones was calculated at –5 V and 610 nm. Moreover, figure 6.4d demonstrates the good linearity of the photocurrent over 6 decades of different intensities of green light at 532 nm. The lowest detectable signal was 34 nW/cm<sup>2</sup>, as defined at  $J_{ph} = 2 \times J_d$  (dashed line).

**Table 6.1.** SCLC mobilities and OPD device performance at –5 V bias.

polymer/ PC <sub>61</sub> BM ratio	$\mu_h^a$ (cm <sup>2</sup> /V s)	$\mu_e^b$ (cm <sup>2</sup> /V s)	$J_d^c$ (mA/cm <sup>2</sup> )	EQE, 610 nm <sup>c</sup> (%)	$D^*^c$ (Jones)	cutoff freq. <sup>c</sup> (kHz)
1:1	$4.5 \times 10^{-5}$	$3.2 \times 10^{-5}$	1.09 [1.26] $\times 10^{-6}$	52.5 [52.0]	1.44 [1.27] $\times 10^{13}$	200 [100]
1:2	$3.1 \times 10^{-6}$	$1.5 \times 10^{-5}$	d	9.2 [9.0]	d	d
2:1	$4.2 \times 10^{-5}$	$6.0 \times 10^{-6}$	0.29 [0.40]	14.3 [14.0]	2.26 [1.92] $\times 10^9$	e

<sup>a</sup>Hole-only device structure: ITO/PEDOT:PSS/active layer/MoO<sub>3</sub>/Al. <sup>b</sup>Electron-only device structure: ITO/ZnO/active layer/LiF/Al. <sup>c</sup>Value for the best performing device. Average value for 16 devices (1:1 blend) or 4 devices (1:2 and 2:1 blend) given in brackets. <sup>d</sup>Short-circuiting devices. <sup>e</sup>Not measured. The active layer thickness was 400 nm.

In summary, OPDs in this study cover a wide spectrum from ultraviolet to the visible red region. An ideal intermixing of the donor and acceptor material was necessary for an efficient charge extraction in the OPD device. The optimum PIDT-TPD/PC<sub>61</sub>BM 1:1 blend fulfilled the form factor requirements that are desired for the application of the photodetector into real-life applications: a high EQE (52%), an ultra-low dark current (1 nA/cm<sup>2</sup>), a relatively high 3 dB cutoff frequency (100 kHz), and a high detectivity ( $1.44 \times 10^{13}$  Jones) that are maintained at high reverse bias (–5 V). In comparison, poly(3-hexylthiophene) (P3HT) is a widely used and top-performing donor polymer in modern solution-processed OPDs.<sup>[69,70,305]</sup> A P3HT-based OPD with a corresponding device architecture was reported to exhibit a detectivity of  $1.63 \times 10^{13}$  Jones, which is comparable to that obtained from PIDT-TPD, but it had a markedly lower cutoff frequency (32 kHz) compared to the PIDT-TPD device.<sup>[303]</sup> Conventional silicon-based

photodetectors typically exhibit detectivities of  $\sim 3\text{--}4 \times 10^{13}$  Jones or higher,<sup>[213,215]</sup> which is very close to the performance of the PIDT-TPD device in this study. The device comprising PIDT-TPD as the donor also showed a linear photoresponse even at low irradiance power. Overall, these results are among the best reported in literature for visible solution-processed OPDs based on a D–A copolymer. An interesting figure of merit then is that the detectivity of (dark adapted) human eye is estimated to be of the order of  $10^{17}$  Jones at 500 nm,<sup>[306]</sup> which is a remarkable value compared to any of the man-made photodetectors.

## 6.2. PIDT-2TPD as the Acceptor for All-PPDs

### 6.2.1. The D–A–A Design Motif

The previous chapter introduced a highly functional polymer/fullerene blend for OPD devices. Fullerene derivatives can deliver good charge transport properties and high efficiencies for the photoresponse devices, but they exhibit a rather weak light absorption, especially toward the low-energy spectral region, and low long-term stability of the BHJ morphology.<sup>[307-309]</sup> These disadvantages intrinsically limit the performance of the photoresponse devices. Therefore, it is desirable to develop photoactive materials that can retain the high performance over a long period of time, exhibit strong and complimentary absorption for broad spectrum detection, and allow flexibility for the tuning of the electronic properties – both of the donor and the acceptor.

The use of both p-type donor and n-type acceptor polymers is a versatile method that allows precise engineering of the optical and electronic properties of the BHJ. However, thus far only a few examples have been reported where polymer/polymer blends have been used in all-polymer photodetectors (all-PPDs). Wang et al.<sup>[310]</sup> used P3HT as the donor and a ladder-structured polypyrrone as the acceptor and obtained an EQE of  $\sim 20\%$  and a  $D^*$  of  $1.3 \times 10^{11}$  Jones at 610 nm. Introduction of the naphthalene diimide (NDI)- and perylene diimide (PDI)-based acceptor polymers, with various combinations of donor polymers, delivered detectivities in the order of  $10^{12}$  Jones and spectral responses extending up to 1100 nm.<sup>[311-314]</sup> These values are comparable to the fullerene-based OPDs, but the relatively low absorption coefficients of the NDI- and PDI-based acceptors partially limited the EQEs of the devices below 25%. This sets a strong motivation to develop polymeric acceptors with strong light absorption.

From molecular design point of view, the acceptor polymer should ideally have (i) strong and complementary absorption with the donor polymer and (ii) low-lying LUMO energy level

to obtain sufficient LUMO–LUMO offset and driving force for charge extraction in blends with the donor. The combination of IDT as the electron-rich unit and the interconnected 2TPD as the electron-deficient unit in PIDT-2TPD, i.e., using the so-called D–A–A design strategy, delivered these properties when used as an acceptor in blend with P3HT donor. The all-PPDs fabricated from the P3HT/PIDT-2TPD blend showed strong photoresponse and nearly planar detectivity over the entire visible spectral range, thereby indicating that PIDT-2TPD is a highly functional new type of n-type material for BHJ devices.

### 6.2.2. Characterization of the P3HT/PIDT-2TPD Blend

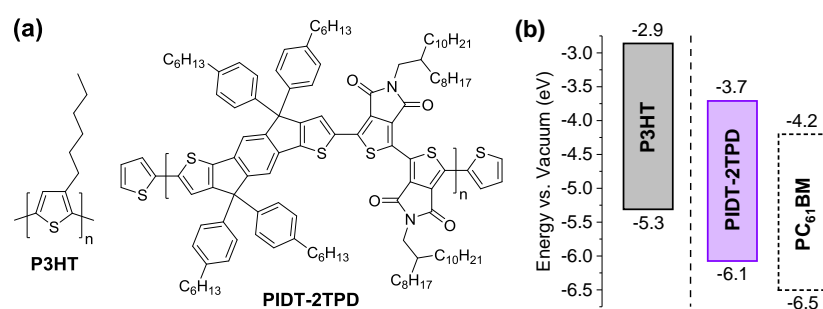


**Figure 6.5.** (a) Chemical structures and (b) energy levels of P3HT donor and PIDT-2TPD acceptor in comparison to PC<sub>61</sub>BM, as derived from CV.

The chemical structures of P3HT and PIDT-2TPD are shown in Figure 6.5a. The former was commercially available and the synthesis of the latter polymer is described in Chapter 4.2. The HOMO and LUMO energy levels of the polymers were measured by CV. Connecting the two TPD units stabilized the LUMO and decreased that energy level, both of the 2TPD monomer and the PIDT-2TPD copolymer, and made it suitable as acceptor, as illustrated in comparison to PC<sub>61</sub>BM in Figure 6.5b. The HOMO–HOMO and LUMO–LUMO offsets were both 0.8 eV, which is – without a doubt – sufficient for exciton separation in the photoactive layer.

Figure 6.6a presents the absorption coefficient versus wavelength curves of the polymers in solution. PIDT-2TPD showed slightly stronger absorption peaking at 609 nm, as compared to the absorption maximum of P3HT at 458 nm. When going to the solid-state thin films (Figure 6.6b), the absorption profile of PIDT-2TPD remained similar to that in solution. P3HT showed a broadened and red-shifted absorption with the peak maximum at 516 nm, which is ascribable to its characteristic  $\pi$ – $\pi$  stacking in the solid state.<sup>[315-317]</sup> As a result, the absorption coefficient of P3HT increased in comparison to PIDT-2TPD in the solid state. It is important to note that the absorption of PIDT-2TPD was significantly stronger than the values reported

previously for NDI- and PDI-based acceptors (i.e., in the range of  $1\text{--}4 \times 10^4 \text{ cm}^{-1}$ ).<sup>[318-320]</sup> Both P3HT and PIDT-2TPD exhibited an  $E_{\text{opt}}$  of 1.9 eV, as estimated from the onset of absorption in thin films. The absorption coefficient versus wavelength curves of the P3HT/PIDT-2TPD blends in 2:1, 1:1, and 1:2 ratio are included in Figure 6.6b. All three blends exhibited strong complementary absorption from 350 to 680 nm, but the absorption from P3HT dominated in the 2:1 and 1:1 blends, as expected from the neat polymer films. PL measurements in paper VI indicated that the high intensity emission of PIDT-2TPD was completely quenched in the 2:1 and 1:1 blends. Even the acceptor-rich (1:2) blend showed only a weak trace of emission from PIDT-2TPD, which further confirmed an efficient exciton separation taking place in the photoactive layer.

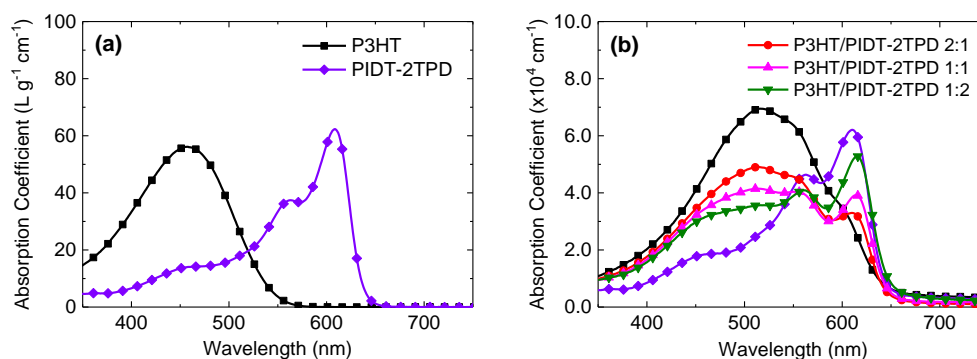


**Figure 6.6.** (a) Absorption coefficients of P3HT and PIDT-2TPD in chlorobenzene solution. (b) Absorption coefficients of the neat polymers and polymer/polymer blends in thin films.

AFM imaging was employed to study the surface morphology of the blends (Figure 6.7). All three blends exhibited relatively smooth surfaces but the RMS roughness was highest for the P3HT/PIDT-2TPD 2:1 blend (2.11 nm, Figure 6.7a). The RMS roughness decreased to 1.44 nm for the 1:1 blend (Figure 6.7b) and further to 1.06 nm for the 1:2 blend (Figure 6.7c). This was in line with the expectation that the more amorphous PIDT-2TPD would be highly miscible and interfere with the more crystalline P3HT domains. DMTA temperature scans in paper VI indicated that the 2:1 and 1:1 blends exhibited thermal transitions ascribable to both P3HT-rich and PIDT-2TPD-rich phases, whereas the 1:2 blend showed a dominant thermal transition of the PIDT-2TPD-rich phase. This suggests that P3HT was effectively dispersed in the acceptor-rich (1:2) blend without desirable phase separation. In contrast, the donor-rich (2:1) blend showed signatures of a continuous and interpenetrating network of P3HT-rich and PIDT-2TPD-rich phases, which is ideal for efficient charge extraction in the devices.

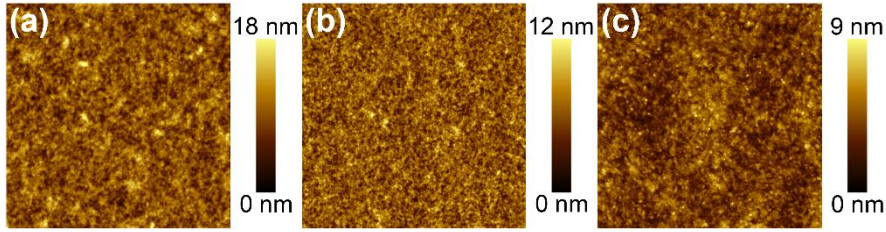


**Figure 6.7.** Tapping mode AFM topography images ( $5 \times 5 \mu\text{m}$ ) of P3HT/PIDT-2TPD blends in (a) 2:1 ratio, (b) 1:1 ratio, and (c) 1:2 ratio.

### 6.2.3. Performance of the All-PPDs

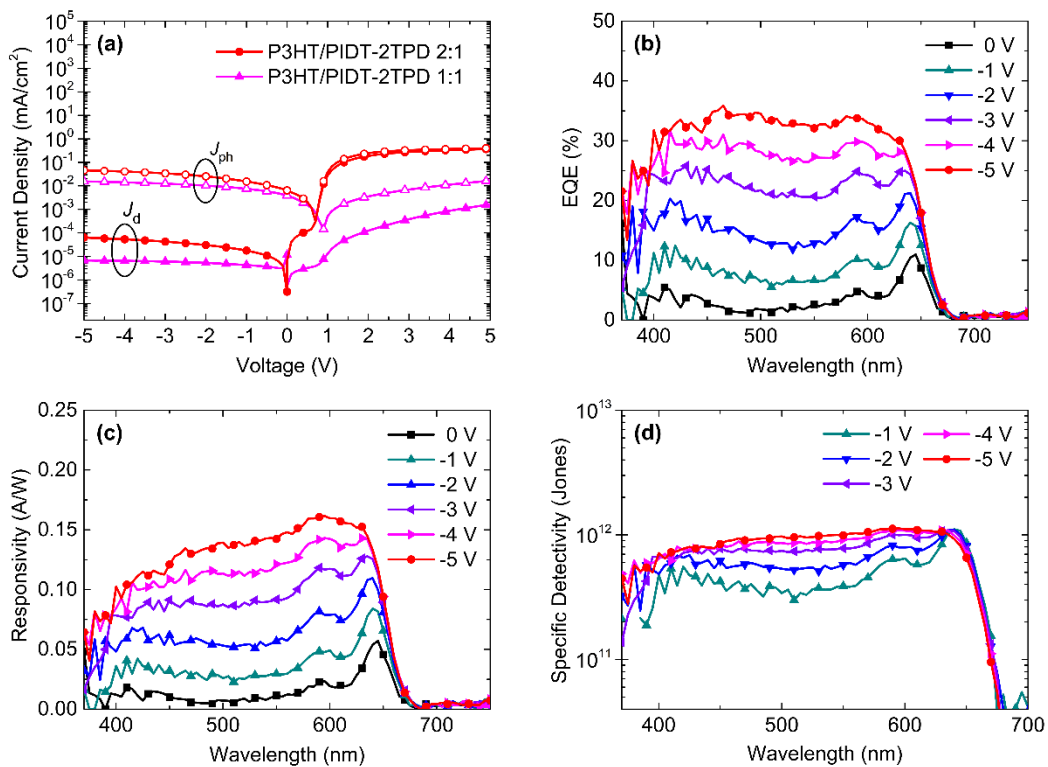


**Figure 6.8.** (a)  $J$ - $V$  characteristics of the all-PPDs comprising P3HT/PIDT-2TPD blend in 2:1 (red circles) and 1:1 ratio (pink triangles) in the dark (solid symbols) and under green light at 532 nm at  $780 \mu\text{W}/\text{cm}^2$  (open symbols). (b) EQE, (c) responsivity, and (d) specific detectivity of the device based on the 1:1 blend at different bias voltages.

The all-PPDs were fabricated by using the P3HT/PIDT-2TPD blend in 2:1, 1:1, or 1:2 ratio as the active layer, which was sandwiched between the ITO/TIPS pentacene and the Al contact. TIPS pentacene was used as an electron blocking interlayer, as described in Chapter 6.1. The active layer thickness was optimized to 400 nm. The best device performance was obtained with the 2:1 blend, which exhibited a  $J_d$  of  $6.42 \times 10^{-5} \text{ mA}/\text{cm}^2$  at  $-5 \text{ V}$  bias (Figure 6.8a). It

is worth noting that this is among the lowest dark currents reported for all-PPDs at high  $-5$  V negative bias and also comparable to the devices based on the P3HT donor and the fullerene acceptor.<sup>[305,311,314,321]</sup> The  $J_d$  could be further decreased to  $6.83 \times 10^{-6}$  and  $2.85 \times 10^{-6}$  mA/cm<sup>2</sup> with the 1:1 and 1:2 blends, respectively, but the  $J_{ph}$  was three times lower for the 1:1 blend compared to the 2:1 blend (Table 6.2). The 1:2 blend did not show any photocurrent response under green light (therefore not shown in Figure 6.8a). SCLC mobility measurements in paper VI indicated that all of the three blends exhibited somewhat balanced charge transport, but the 2:1 and 1:1 blends delivered the highest mobilities. This result is in good agreement with the morphological characterization and the all-PPD device performance. A general observation is that the P3HT/PIDT-2TPD blend facilitated an efficient exciton separation in all of the studied concentrations, as observed from the PL quenching in paper VI, but the low charge mobility and lack of photocurrent response in the 1:2 blend can only be explained by its homogeneous morphology. The 2:1 blend exhibited a desired degree of phase separation for efficient charge extraction in the devices, and it was considered as the optimum active layer.

**Table 6.2.** SCLC mobilities and all-PPD device performance at  $-5$  V bias.

P3HT/PIDT- 2TPD ratio	$\mu_h^a$ (cm <sup>2</sup> /V s)	$\mu_e^b$ (cm <sup>2</sup> /V s)	$J_d$ (mA/cm <sup>2</sup> )	$J_{ph}$ (mA/cm <sup>2</sup> )
2:1	$9.2 \times 10^{-5}$	$4.0 \times 10^{-5}$	$6.42 \times 10^{-5}$	$4.57 \times 10^{-2}$
1:1	$6.0 \times 10^{-5}$	$9.1 \times 10^{-5}$	$6.83 \times 10^{-6}$	$1.56 \times 10^{-2}$
1:2	$6.4 \times 10^{-6}$	$9.8 \times 10^{-6}$	$2.85 \times 10^{-6}$	<sup>c</sup>

<sup>a</sup>Hole-only device structure: ITO/PEDOT:PSS/active layer/MoO<sub>3</sub>/Al. <sup>b</sup>Electron-only device structure: ITO/ZnO/active layer/LiF/Al. <sup>c</sup>No photocurrent response.

Based on the above results, further all-PPDs characterization was focused solely on the 2:1 blend. The active layer exhibited excellent electrochemical stability, which can be seen from the systematic increase of EQE with increasing negative bias in Figure 6.8b. As a result, the EQE reached over 30% at  $-5$  V. Responsivity and detectivity of the corresponding device were calculated using Equations (3.4) and (3.7) in Chapter 3.3.  $R$  increased linearly when the reverse bias was increased from 0 V to  $-5$  V, reaching 0.16 A/W at 610 nm, as shown in Figure 6.8c. Interestingly, the EQE and  $R$  graphs resembled the absorption of the blend film (Figure 6.6b), which indicated that both the P3HT donor and the PIDT-2TPD acceptor contributed to the photoresponse, and thereby validated the D–A–A design motif. Thanks to the low dark current at  $-5$  V, the  $D^*$  was  $1.1 \times 10^{12}$  Jones at 610 nm (Figure 6.8d). This value is in the same order

of magnitude with the best performing all-PPDs and, perhaps even more importantly, higher than the values reported so far for all-PPDs comprising P3HT as the donor.<sup>[310-314]</sup> Moreover, the  $D^*$  remained nearly planar from 370 to 660 nm, which is essentially over the entire visible range. This clearly confirmed the functionality of PIDT-2TPD as the acceptor in the BHJ. The 3dB cutoff frequency was recorded at  $1.5 \times 10^3$  Hz in paper VI, which is substantially lower than that obtained for the PIDT-TPD/PC<sub>61</sub>BM blend in Chapter 6.1. The lower photoresponse rate is probably due to a less efficient charge extraction that is common for all-polymer BHJ devices versus fullerene-based devices.<sup>[307]</sup>

In this study, PIDT-2TPD proved to be a highly functional new type of acceptor polymer for all-PPDs. The P3HT/PIDT-2TPD blend in 2:1 ratio showed a stable device performance in terms of delivering an EQE of ~30% and nearly planar detectivity essentially over the entire visible spectral range, when driven at a high reverse bias of -5 V. The analogy between the absorption profile of the blend and the photoresponse of the all-PPD device confirmed that the acceptor polymer had a strong contribution to the overall light absorption, which is critical for the performance of any all-polymer BHJ device.

## 7. Conclusion and Outlook

Taking into account the limited yield of emissive excitons from the lowest excited singlet state (set by the spin statistics) and the increase of nonradiative decay rate with decreasing energy gap (given by the energy gap law), an EQE of 1.1% from the OLED comprising BTT\* as the NIR emitter is probably close to the performance limit of a solution-processable fluorescent organic molecule in the >800 nm region. Therefore, any significant improvement in the EQE necessitates the involvement of triplet excitons in the emission process. One example of such system could be introduction of a TADF molecule as an “assistant dopant” in the well-defined blend of PIDT-2TPD host and BTT\* emitter. As discussed in Chapter 4.2 and paper II, the fluorescence efficiency of the host matrix had a significant influence on the NIR-performance of BTT\* molecule. This can be described as an “exciton pumping” effect of the host matrix, and it is plausible that the exciton feed could be further enhanced with the use of an additional TADF dopant, ultimately delivering NIR emission selectively from BTT\*. Of course, to make such a ternary blend of polymer host, TADF assistant dopant, and NIR small molecule work in an OLED it would require careful optimization of the singlet and triplet energy levels of the TADF molecule with respect to the host and the NIR emitter, along with many other aspects discussed in the literature<sup>[169-171,322]</sup> and throughout this thesis. Similar assistant dopant concept has been introduced previously by Adachi et al.,<sup>[32,164,230,241]</sup> but so far not applied successfully for solution-processed OLEDs nor for materials emitting beyond 800 nm.

Successful introduction of triplet excitons in the emission process leads to an improvement of EQE, but with a concomitant penalty of prolonged exciton lifetime in the order of hundreds of nanoseconds or even in the microsecond range. This limits the applicability of such emitters, for example in Li-fi networks, where fluorescent molecules can be integrated for a high-speed data transfer. In that perspective, the fast decay (2.5 ns) of the blend of PIDT-2TPD and 0.5% of BTT\* makes it highly appealing for the engineering of NIR optical networks.

Another important aspect of NIR emitters is their stability in the light-emitting devices. LECs, in general, can deliver high-intensity emission and good long-term stability thanks to the p–n junction doping structure, which ensures efficient electron and hole recombination and allows device fabrication without the use of air-sensitive cathode metals. The p- and n-type doping is believed to be responsible of exciton quenching by polarons, which effectively reduces the EQE of the devices, as studied in detail by van Reenen et al.<sup>[281,282]</sup> However, LECs comprising IDTT-based random copolymers as NIR emitters systematically delivered higher

radiances and EQEs than the corresponding OLED devices, as discussed in Chapter 5.2 and paper IV. This is a good indication of the benefits of polymeric emitters, related to their electrochemical stability and charge transport properties for an ideal formation of the p–n junction structure.

Two questions may arise when considering the development of NIR-LECs: (i) if the emission can be redshifted further in the NIR region while maintaining the device performance and (ii) if a blend of polymer matrix and small molecule as the NIR-emissive material can somewhat improve the device performance. Both of these questions could be addressed by synthesizing a low-gap small molecule comprising a fluorescent acceptor core, coupled with strong donor units, and finding a suitable host polymer with good charge transport properties. However, care must be taken in the design of small molecules, so that the electrochemical stability of the active layer, which is one of the major benefits of polymeric emitters, is not compromised when the LEC is driven with a high current density.<sup>[323]</sup> On the other hand, introduction of the electrolyte salt as a third component in the host/guest blend sets further requirements for efficient intermolecular host-to-guest energy/charge transfer, so as to obtain emissive excitons selectively at the NIR molecule and avoid “leaking” of emission both from the host and the guest sites, as reported previously by Tang et al.<sup>[204,324,325]</sup>

The performance of polymeric emitters is closely connected to their charge transport properties, and this was demonstrated with the photodetectors comprising either PIDT-TPD as the donor or PIDT-2TPD as the acceptor. The strong light absorption that is common for donor polymers was retained with the D–A–A structured acceptor polymer, which motivates the use of similar design strategy for other high-performance all-PPDs operating at different wavelengths. Similarly to the light-emitting devices, the application of photodetectors depend on their maximum bandwidth and wavelength range. Where visible red photodetectors can be used, e.g., for VLC networks and photo and video imaging, for biomedical applications one needs materials that can convert the low-energy NIR light, e.g., that of the BTT\* OLED at 840 nm, into a detectable current at high speeds. At the moment, there are only few examples of polymers that can deliver high photoresponse (and high speed) at this specific wavelength, the diketopyrrolopyrrole-based donors reported by Hendriks et al.<sup>[63]</sup> being one of such materials. Naturally, this is a strong motivation for further development of polymer donors and acceptors for the application in NIR photodetectors.

On a personal note, the most common questions I get asked in a non-scientific field on my research, as a synthetic chemist, are (i) can I tell about the applications of NIR emitters, (ii) who is going to build such devices, (iii) who is going to need such devices, and (iv) when, if ever, they will be available for consumers. These questions, among many others, have not only made me think about my work in a broad perspective, but also raised my self-awareness that is helpful for positioning the research in this thesis within the related scientific field. To grasp the latter issue, the research on organic NIR emitters has progressed tremendously since the beginning of my PhD project. The literature entitled as “far-red/NIR emitters”, presumably to highlight the (literally) invisible barrier of NIR region, albeit often reporting only a marginal device performance, has developed into titles such as “highly efficient”, “improved emissive state”, “small efficiency roll-off”, and “efficient nondoped NIR-OLED”, just to mention some examples. This is a clear indication that organic emitters are indeed attractive because of their benign environmental impact and applicability for biomedical and even implantable devices. However, many of the above mentioned titles still do not promise emission envelopes purely in the NIR, and further research is needed in that regard.

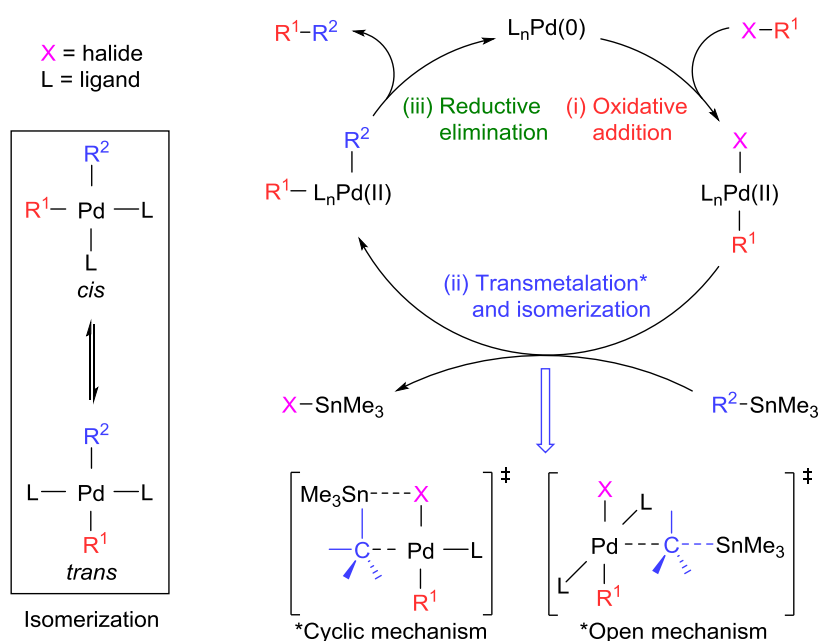
To further comment on the above questions, the technology is already available for anyone to implement into commercial purposes, and in the current view the development of organic NIR emitters and other optoelectronic materials will be faster than ever before. Yet the long-term stability of organic materials and their efficiency of converting electricity into light, or light into electricity, remain great challenges. Another is the effectiveness of mass production of the conjugated polymers and small molecules, and keeping their performance comparable to the small lab-scale batches. A major leap in these aspects is probably the factor that triggers the large-scale public interest toward organic optoelectronics.



## 8. Methods

This chapter provides additional information about the methodology that is discussed, but not described in detail earlier in this thesis, including Pd-catalyzed cross-coupling (Chapters 4–6), DFT calculation (Chapters 2, 4, and 5), and AFM and TEM imaging (Chapter 6). In particular, Stille coupling and its alternative, direct arylation, have been broadly applied throughout this thesis, and are therefore worth taking a closer look. For the same reason, although Pd-catalyzed Suzuki–Miyaura reaction is another famous cross-coupling method,<sup>[326]</sup> it is omitted from this chapter. DFT is a helpful tool to better understand the conformational and electronic structure of the synthesized (or planned) polymers and small molecules, but it is also a popular topic of debate,<sup>[327]</sup> as discussed shortly in this chapter. The AFM and TEM methods are described for an easy access to the conditions of the images presented in this thesis.

### 8.1. Stille Coupling



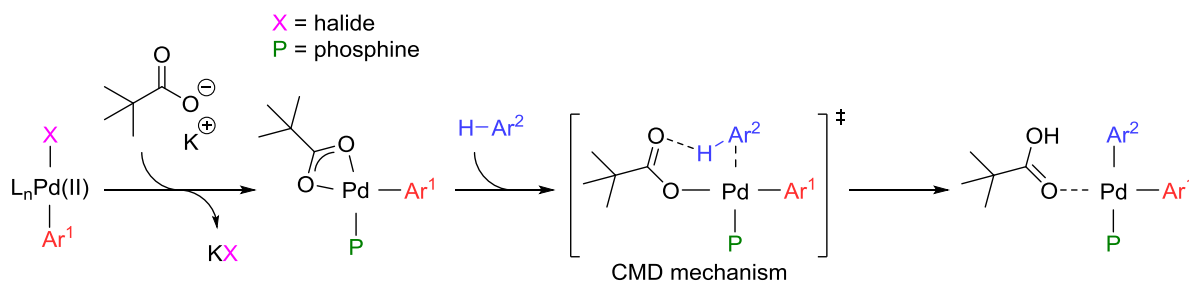
**Scheme 8.1.** A generic catalytic cycle of Pd-catalyzed Stille coupling.

The Pd-catalyzed Stille cross-coupling is an efficient method for the coupling of aromatic (or aliphatic) halides and corresponding organotin reagents (i.e., organostannanes).<sup>[328,329]</sup> Scheme 8.1 represents a simplified catalytic cycle of the Stille reaction proceeding as a Pd coordination complex. The key steps in the cycle are (i) oxidative addition of the aryl halide, (ii) addition of the secondary aryl group via transmetalation, followed by isomerization, and (iii) formation

of the new carbon–carbon bond via reductive elimination. Oxidative addition on Pd(0) occurs efficiently in coordination to electron-rich phosphine ligands.<sup>[330]</sup> Transmetalation is a critical step in the catalytic cycle, and the reaction is proposed to proceed either via a cyclic or an open transition state, as shown on the bottom of Scheme 8.1.<sup>[331-333]</sup> A third possible transmetalation pathway has been proposed to go through an ionic transition state.<sup>[332]</sup> The cyclic mechanism requires a good bridging anionic ligand (a halide), and more electronegative halides make the Pd(II) center more electrophilic, thus accelerating the transmetalation step.<sup>[334]</sup> Note, however, that the energy barrier for oxidative addition, step (i), increases accordingly, in the order  $I < Br < Cl < F$ .<sup>[335]</sup> The open (or ionic) transmetalation is favored for badly coordinating anionic ligands (other than halides), which create an electrophilic Pd(II) center (or a cationic Pd(II) center due to a complete dissociation of the anion), ultimately allowing a fast reaction through the step (ii). It is important to note that the transmetalation via either of the transition states is partly reversible, which means that if the final carbon–carbon bond formation, step (iii), is too slow, a number of undesired side reactions can take place via reverse transmetalations.<sup>[331-333]</sup> The reductive elimination step necessitates the carbon–carbon bond forming groups to be *cis* to each other (see the left side box in Scheme 8.1), thereby requiring isomerization of the *trans* intermediate after the transmetalation.<sup>[336,337]</sup>

$Pd_2(dba)_3$  (dba = dibenzylideneacetone) is a widely used catalyst in the Stille coupling, and a source of Pd(0), while tri(*o*-tolyl)phosphine is used as an additional electron-donating ligand. This is a versatile catalytic system, which typically gives excellent yields and high molecular weights,<sup>[338,339]</sup> the latter in the case of polymer synthesis, but it is also reported to be selective between different halides in the aromatic structures.<sup>[340]</sup> On the other hand, one of the above mentioned side reactions is homocoupling of the aryl halides and the organostannanes, which is the main source of structural defects. In the coupling of, say, donor and acceptor monomers to obtain a D–A copolymer, homocoupling leads to the formation of undesired D–D and A–A coupling products.<sup>[341,342]</sup> Some of the homocoupling pathways have been proposed to initiate from the oxidation of Pd(0) in the presence of molecular oxygen, and others from aryl group exchange and reduction of the Pd(II) center to Pd(0) by reductive impurities.<sup>[342-345]</sup> Although some of these undesired reactions may be difficult to control, it is of crucial importance to run the Stille coupling under oxygen-free, inert nitrogen or argon atmosphere.

## 8.2. Direct Arylation



**Scheme 8.2.** Transition state in the Pd-catalyzed and pivalate-assisted direct arylation.

What was not mentioned in the previous section is the toxicity of the organotin reagents used in the Stille coupling.<sup>[342,346]</sup> Direct arylation is an alternative, Pd-catalyzed coupling reaction that does not require the use of organometallic compounds as nucleophiles. Instead, it relies on the activation of weakly acidic ( $sp^2$ )C–H bonds in aromatic structures.<sup>[347,348]</sup> The reaction mechanism of direct arylation is far less studied than that of Stille coupling (Scheme 8.1), but a commonly accepted pathway proceeds via a transition state involving concerted metalation–deprotonation (CMD) of the aromatic structure, as presented in Scheme 8.2.<sup>[347,349]</sup> The CMD mechanism benefits from carboxylic acid as a cocatalyst in the presence of excess base, such as  $K_2CO_3$ . Pivalic acid (pivalate anion in the presence of base) has proven to be an excellent additive that increases the conversion and gives high yields.<sup>[347,350]</sup> After the oxidative addition of the aryl halide, the pivalate coordinates to the Pd(II) center making it highly electrophilic, and acts as a catalytic proton shuttle increasing the reactivity of the completely unactivated (hetero)aryl group.<sup>[347,351]</sup> In the CMD step, the pivalate deprotonates the secondary aryl group without the coordination of the proton to the metal center, while at the same time the C–Pd bond is formed.<sup>[349,351,352]</sup> After the dissociation of pivalic acid, a new carbon–carbon bond is formed via reductive elimination, as in the case of Stille coupling. However, another plausible mechanistic pathway involves the pivalate being coordinated to the Pd(II) center throughout the catalytic cycle.<sup>[347-349]</sup>

Apart from the decreased toxicity and increased atom economy of direct arylation,<sup>[353]</sup> it is worth mentioning that most aromatic monomers contain multiple reactive C–H bonds. The selectivity depends on the energy barrier to reach the CMD transition state,<sup>[354,355]</sup> but in many cases the reaction can occur at various positions leading to structural impurities, such as cross-linking, branching, and homocoupling.<sup>[342,349]</sup> This is particularly relevant for the synthesis of copolymers, for which the post-reaction purification is not as straightforward as for monomers

or small molecules. However, recent advances in the direct arylation have resulted in nearly defect-free polymers through the control of selectivity.<sup>[356-359]</sup>

### 8.3. DFT Calculation

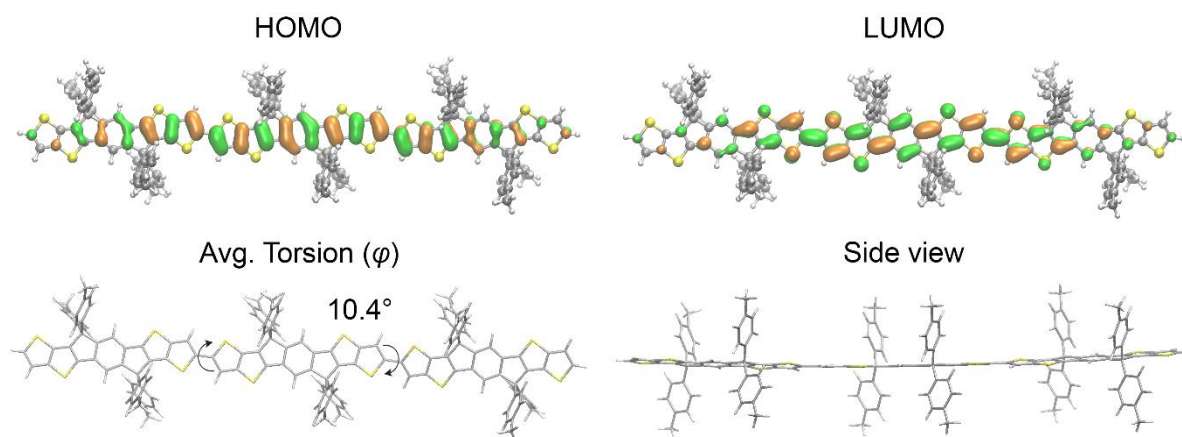


**Figure 8.1.** DFT-calculated HOMO hole density, LUMO electron density, and backbone torsion of a PIDTT model compound comprising three repeating units.

DFT calculation is, at the minimum, a supplementary approach to estimate the HOMO/LUMO (or IP/EA) energy levels, the corresponding orbitals distribution, and the structure (including conformation and backbone torsion) of the studied molecules. Combination of B3LYP hybrid functional and 6-31G(d,p) basis set is used for the optimization of the ground state geometry in gas phase.<sup>[360-362]</sup> As a common practice, the long alkyl side chains are truncated to shorter methyl (or methoxy etc.) groups to facilitate the calculations in a reasonable time scale. Instead of doing simulations on large polymer structures, smaller model compounds comprising 1–4 repeating units are typically calculated. Then, extrapolation to an infinite chain length allows the estimation of larger “polymeric” HOMO and LUMO energy levels.<sup>[91-93]</sup> Since the change in energy, i.e.,  $\Delta E_{\text{HOMO}}$  and  $\Delta E_{\text{LUMO}}$ , of the large conjugated structures becomes diminishingly small after 3–4 repeating units, it is often practical to calculate a single structure comprising three repeating units as a representative model compound, as shown for PIDTT in Figure 8.1. Importantly, however, different combinations of *cis* and *trans* isomers and/or torsion potential energy surfaces are calculated to find the energetically most stable conformation.<sup>[363,364]</sup>

One issue related to the relatively cheap B3LYP functional is that it tends to overestimate the torsion energy barrier, and thus the planarity of the conjugated (polymer) backbone.<sup>[365,366]</sup> Another, more general concern is that the HOMO hole and LUMO electron densities, and the corresponding energies, might be different in the solid state compared to the ideal gas-phase

conditions. However, the DFT-calculated HOMO and LUMO energies, and  $E_g$  values, were qualitatively similar with the CV-derived values throughout this thesis. Calculation of excited state energies and geometries, via time-dependent DFT calculations,<sup>[367]</sup> necessitate the use of long-range corrected functionals, such as  $\omega$ B97XD,<sup>[368]</sup> which allow the tuning of the range-separation parameter,  $\omega$ , by minimizing the error between IP and HOMO energies and/or that of EA and LUMO energies.<sup>[105,106,369,370]</sup> The vertical IP is calculated as the difference between the ground-state energy of a neutral  $N$  electron system and a cationic  $N - 1$  electron system, both at the optimized geometry of the  $N$  electron system. The vertical EA is calculated as the energy difference between the  $N$  electron system and an anionic  $N + 1$  electron system at the optimized geometry of the  $N$  electron system.<sup>[371]</sup>

#### 8.4. AFM and TEM

The AFM samples were prepared by spin-coating the active layer on a glass/PEDOT:PSS film (Chapter 6.1) or directly on a glass substrate (Chapter 6.2) from chlorobenzene solution. The concentration of PIDT-TPD (Chapter 6.1) and PIDT-2TPD (Chapter 6.2) were 15 mg/mL for all blends. Tapping-mode images were acquired with an NT-MDT NTEGRA Prima scanning probe microscope using NT-MDT NSG01 (single crystal silicon, reflective Au-coating) AFM probes at a resonant frequency of  $\sim 200$  kHz. The TEM samples (Chapter 6.1) were prepared by immersing the above glass/PEDOT:PSS/active layer sample in water, where PEDOT:PSS dissolved and the active layer floated off. The active layer film was transferred to a supporting Cu grid for TEM imaging on a FEI Tecnai T20 (LaB6, 200 kV) instrument.



## **Acknowledgements**

I acknowledge funding of this project by the European Community's Seventh Framework Programme (FP7/2007-2013) ITN Marie Skłodowska-Curie action under Grant Agreement No. 607585 (OSNIRO) and Flinders University.

First, I want to thank my supervisors Dr. Ergang Wang and Prof. Mats Andersson for giving me the opportunity to join the international and collaborative research groups at Chalmers and Flinders. I knew already during the application process that this PhD project will be demanding in all professional and scientific aspects, but at the same time an extraordinary opportunity to get involved in the world's top level research with multiple research groups and institutions, not to speak about the double-PhD degree. These were the exact reasons I wanted to join. On the other hand, I also enjoy certain freedom to explore my research, and I am happy that you both have genuinely supported me in these endeavors.

I want to point out that none of the research published in the papers and discussed in this thesis could have been done in such an extent without the contribution from our collaborators. Prof. Mammo, Zewdneh, and Birhan at AAU and Chalmers, it has been the greatest pleasure to work with you and get to know you all in person. I am grateful for the opportunity to work with Prof. Cacialli, Alessandro, Andrea, Giuseppe, and other collaborators and friends at UCL. I have enjoyed your high level of expertise and communication during this project, and your warm hosting during my secondment. Alessandro, many thanks for your help with my thesis. Prof. Edman, Shi, and all other co-workers at Uni Umeå and LunaLEC AB, I am happy that I got to know you and work with you. I want to thank you for the trustful and open atmosphere, and your critical feedback necessary for learning. I appreciate the aspect that Sandro and Cindy at Siemens Healthineers, and other related collaborators, have given for my studies. Our work has been educational in the most unexpected manner in my project. Cindy, thank you for the great time during our secondments and your help with my thesis.

I am grateful to all OSNIRO members for the networking, education, sharing, inspiration, and friendships. Prof. Scherf, Sybille, Sebnem, Amaranda, and others at Uni Wuppertal, thank you for your hospitality during my first secondment. Christos, Benedetta, and all other Advent people, I was privileged to experience the Greek culture during my secondment, and later work together with the paper. George was a great local guide. Prof. Janssen, Martijn, Stefan, Dario,

and others at TU/e, thank you for the hosting and generously providing all the facilities for my research during my secondment. Dario, thank you for the best moka coffee in my life.

I want to thank all the former and present group members at Chalmers and Flinders. Within the limitation of this chapter, Xiaofeng, thank you for helping me getting started at Chalmers and being a helpful colleague and trustworthy friend. Zhaojun, it was a pleasure to travel with you all the OSNIRO meetings and conferences. You are a lovely group member. *Kim, tack för din hjälp med min svenska. Det var svårt i början, antar inte alls lättare för dig, men viktigaste är att vi nu har ett kodspråk som bara vi två kan förstå.* Special thanks to Mariza, you if anyone can create a good atmosphere in and outside the work life. And thank you for the UV-Vis-NIR multi-color vision. Juuso and Benedikt, thank you for your valuable input in this project. Ulises for the inspiration and funny PhD advices, Cedrik for the Yoga-balanced spirit, David, Lidia, Josue, Wenjing, Francis, Qunping, Jiamin, Xinjian, Qiang (Tao-master), and Liangjian, thank you for your friendships and help throughout my PhD studies. Desta, Anirudh, Sait, Caroline, Jonas, Guler, and Bradley, thank you for welcoming me and taking me quickly as a member of the group. You are great scientists and even greater friends. I want to thank you all for your help with the synthesis, characterization, and electrochemistry, as well as your good spirit and enjoyable company at work and free time – let alone the conference trips.

I have enjoyed the company of people at Chalmers and Flinders – the Fika room and the Tea room. I want to thank Anders Mårtensson for providing the GPC data, Jason Young for helping with MALDI-TOF, and Mattias for helping with the microscopy for the cover image. Behabitu, thanks for your last minute (i.e., month) advices for my thesis. I am grateful for the support of David Lewis at Flinders and Jerker, Hanna, and Per at Chalmers. *Lotta och Frida, tusen tack för er hjälp med allt från min första lägenhet till disputation.* I also want to thank Juha Heiskanen at Uni Oulu for the discussions and collaboration. Thank you all!

Warm thanks to my family, Raija, for always being there as the *Äippä* when needed, *kiitos kun täytit reppuun neuvoista kalleimmat*, Pasi, to you I'm still the (silly) younger brother that you have to teach and look after, and I hope it stays that way, and Aake, I can't throw you over the flooding ditch anymore, but I hope can still throw you a hand in life whenever needed.

My fiancée, Mira, no words are enough to thank you for sharing all these years, countries, and memories with me. Obvious or not, you mean everything to me. *MRS* – I love you.

*Petri*

## Bibliography

- [1] T. Sekitani, H. Nakajima, H. Maeda, T. Fukushima, T. Aida, K. Hata, T. Someya, *Nat. Mater.* **2009**, *8*, 494.
- [2] M. S. White, M. Kaltenbrunner, E. D. Głowacki, K. Gutnichenko, G. Kettlgruber, I. Graz, S. Aazou, C. Ulbricht, D. A. M. Egbe, M. C. Miron, Z. Major, M. C. Scharber, T. Sekitani, T. Someya, S. Bauer, N. S. Sariciftci, *Nat. Photon.* **2013**, *7*, 811.
- [3] S. Park, K. Fukuda, M. Wang, C. Lee, T. Yokota, H. Jin, H. Jinno, H. Kimura, P. Zalar, N. Matsuhisa, S. Umezu, G. C. Bazan, T. Someya, *Adv. Mater.* **2018**, *30*, 1802359.
- [4] J. Huang, H. Zhu, Y. Chen, C. Preston, K. Rohrbach, J. Cumings, L. Hu, *ACS Nano* **2013**, *7*, 2106.
- [5] H. Zhu, Z. Fang, Z. Wang, J. Dai, Y. Yao, F. Shen, C. Preston, W. Wu, P. Peng, N. Jang, Q. Yu, Z. Yu, L. Hu, *ACS Nano* **2016**, *10*, 1369.
- [6] X. Xu, J. Zhou, L. Jiang, G. Lubineau, T. Ng, B. S. Ooi, H.-Y. Liao, C. Shen, L. Chen, J. Y. Zhu, *Nanoscale* **2016**, *8*, 12294.
- [7] S. Choi, H. Lee, R. Ghaffari, T. Hyeon, D.-H. Kim, *Adv. Mater.* **2016**, *28*, 4203.
- [8] Y. Khan, A. E. Ostfeld, C. M. Lochner, A. Pierre, A. C. Arias, *Adv. Mater.* **2016**, *28*, 4373.
- [9] D. Han, Y. Khan, J. Ting, S. M. King, N. Yaacobi-Gross, M. J. Humphries, C. J. Newsome, A. C. Arias, *Adv. Mater.* **2017**, *29*, 1606206.
- [10] A. Sandström, H. F. Dam, F. C. Krebs, L. Edman, *Nat. Commun.* **2012**, *3*, 1002.
- [11] D. Braga, N. C. Erickson, M. J. Renn, R. J. Holmes, C. D. Frisbie, *Adv. Funct. Mater.* **2012**, *22*, 1623.
- [12] Y. L. Kong, I. A. Tamargo, H. Kim, B. N. Johnson, M. K. Gupta, T.-W. Koh, H.-A. Chin, D. A. Steingart, B. P. Rand, M. C. McAlpine, *Nano Lett.* **2014**, *14*, 7017.
- [13] A. Pierre, I. Deckman, P. B. Lechêne, A. C. Arias, *Adv. Mater.* **2015**, *27*, 6411.
- [14] X. Xu, X. Zhou, K. Zhou, Y. Xia, W. Ma, O. Inganäs, *Adv. Funct. Mater.* **2018**, 1805570.
- [15] H. C. Gorton, J. M. Swartz, C. S. Peet, *Nature* **1960**, *188*, 303.
- [16] M. Gershenson, R. M. Mikulyak, *J. Appl. Phys.* **1961**, *32*, 1338.
- [17] N. H. Jr., S. F. Bevacqua, *Appl. Phys. Lett.* **1962**, *1*, 82.
- [18] M. I. Nathan, *Solid-State Electron.* **1963**, *6*, 425.
- [19] S. V. Galginaitis, *J. Appl. Phys.* **1964**, *35*, 295.
- [20] D. F. Williams, M. Schadt, *Proc. IEEE* **1970**, *58*, 476.
- [21] P. S. Vincett, W. A. Barlow, R. A. Hann, G. G. Roberts, *Thin Solid Films* **1982**, *94*, 171.
- [22] C. W. Tang, S. A. VanSlyke, *Appl. Phys. Lett.* **1987**, *51*, 913.
- [23] D. Y. Kim, T.-H. Lai, J. W. Lee, J. R. Manders, F. So, *Sci. Rep.* **2014**, *4*, 5946.
- [24] P. A. Haigh, F. Bausi, Z. Ghassemlooy, I. Papakonstantinou, H. Le Minh, C. Fléchon, F. Cacialli, *Opt. Express* **2014**, *22*, 2830.
- [25] D. Tsonev, S. Videv, H. Haas, *Proc. SPIE* **2014**, *9007*, 900702.
- [26] S. T. Le, T. Kanesan, F. Bausi, P. A. Haigh, S. Rajbhandari, Z. Ghassemlooy, I. Papakonstantinou, W. O. Popoola, A. Burton, H. Le Minh, F. Cacialli, A. D. Ellis, *Opt. Lett.* **2014**, *39*, 3876.

- [27] P. A. Haigh, F. Bausi, H. Le Minh, I. Papakonstantinou, W. O. Popoola, A. Burton, F. Cacialli, *IEEE J. Sel. Areas Commun.* **2015**, *33*, 1819.
- [28] B. Jang, J.-Y. Park, C.-H. Tung, I.-H. Kim, Y. Choi, *ACS Nano* **2011**, *5*, 1086.
- [29] S. Huang, R. K. Kannadorai, Y. Chen, Q. Liu, M. Wang, *Chem. Commun.* **2015**, *51*, 4223.
- [30] Z. Meng, F. Wei, R. Wang, M. Xia, Z. Chen, H. Wang, M. Zhu, *Adv. Mater.* **2016**, *28*, 245.
- [31] A. Shao, Y. Xie, S. Zhu, Z. Guo, S. Zhu, J. Guo, P. Shi, T. D. James, H. Tian, W.-H. Zhu, *Angew. Chem. Int. Ed.* **2015**, *54*, 7275.
- [32] T. Yamanaka, H. Nakanotani, S. Hara, T. Hirohata, C. Adachi, *Appl. Phys. Express* **2017**, *10*, 074101.
- [33] A. M. Smith, M. C. Mancini, S. Nie, *Nature Nanotechnol.* **2009**, *4*, 710.
- [34] C. V. Hoven, A. Garcia, G. C. Bazan, T.-Q. Nguyen, *Adv. Mater.* **2008**, *20*, 3793.
- [35] H. Ma, H.-L. Yip, F. Huang, A. K.-Y. Jen, *Adv. Funct. Mater.* **2010**, *20*, 1371.
- [36] F. Huang, H. Wu, Y. Cao, *Chem. Soc. Rev.* **2010**, *39*, 2500.
- [37] N. Thejokalyani, S. J. Dhoble, *Renew. Sust. Energy Rev.* **2014**, *32*, 448.
- [38] Q. B. Pei, G. Yu, C. Zhang, Y. Yang, A. J. Heeger, *Science* **1995**, *269*, 1086.
- [39] D. J. Dick, A. J. Heeger, Y. Yang, Q. Pei, *Adv. Mater.* **1996**, *8*, 985.
- [40] Q. Pei, Y. Yang, G. Yu, C. Zhang, A. J. Heeger, *J. Am. Chem. Soc.* **1996**, *118*, 3922.
- [41] C. Yang, Q. Sun, J. Qiao, Y. Li, *J. Phys. Chem. B* **2003**, *107*, 12981.
- [42] L. Edman, *Electrochim. Acta* **2005**, *50*, 3878.
- [43] J. Fang, P. Matyba, L. Edman, *Adv. Funct. Mater.* **2009**, *19*, 2671.
- [44] P. Matyba, K. Maturova, M. Kemerink, N. D. Robinson, L. Edman, *Nat. Mater.* **2009**, *8*, 672.
- [45] A. Asadpoordarvish, A. Sandström, L. Edman, *Adv. Eng. Mater.* **2016**, *18*, 105.
- [46] S. B. Meier, D. Tordera, A. Pertegás, C. Roldán-Carmona, E. Ortí, H. J. Bolink, *Mater. Today* **2014**, *17*, 217.
- [47] E. Fresta, R. D. Costa, *J. Mater. Chem. C* **2017**, *5*, 5643.
- [48] R. F. Potter, W. L. Eisenman, *Appl. Opt.* **1962**, *1*, 567.
- [49] S. R. Morrison, *Solid-State Electron.* **1963**, *6*, 485.
- [50] J. R. Biard, E. L. Bonin, W. T. Matzen, J. D. Merryman, *Proc. IEEE* **1964**, *52*, 1529.
- [51] M. DiDomenico, W. M. Sharpless, J. J. McNicol, *Appl. Opt.* **1965**, *4*, 677.
- [52] T. L. Tansley, *Opto-electron.* **1969**, *1*, 143.
- [53] F. K. Reinhart, *Appl. Phys. Lett.* **1973**, *22*, 372.
- [54] M. J. Hampshire, *Electron. Power* **1974**, *20*, 107.
- [55] F. F. So, S. R. Forrest, *IEEE Trans. Electron Devices* **1989**, *36*, 66.
- [56] S. R. Forrest, *IEEE Circuits Devices Mag.* **1989**, *5*, 33.
- [57] G. Yu, J. Gao, J. C. Hummelen, F. Wudl, A. J. Heeger, *Science* **1995**, *270*, 1789.
- [58] J. G. F. Hide, H. Wang, *Synth. Met.* **1997**, *84*, 979.
- [59] X. Gong, M. Tong, Y. Xia, W. Cai, J. S. Moon, Y. Cao, G. Yu, C.-L. Shieh, B. Nilsson, A. J. Heeger, *Science* **2009**, *325*, 1665.
- [60] M. Ramuz, L. Bürgi, C. Winnewisser, P. Seitz, *Org. Electron.* **2008**, *9*, 369.
- [61] P. E. Keivanidis, P. K. H. Ho, R. H. Friend, N. C. Greenham, *Adv. Funct. Mater.* **2010**, *20*, 3895.
- [62] C. J. Brabec, M. Heeney, I. McCulloch, J. Nelson, *Chem. Soc. Rev.* **2011**, *40*, 1185.

- [63] K. H. Hendriks, W. Li, M. M. Wienk, R. A. J. Janssen, *J. Am. Chem. Soc.* **2014**, *136*, 12130.
- [64] R. Nie, X. Deng, L. Feng, G. Hu, Y. Wang, G. Yu, J. Xu, *Small* **2017**, *13*, 1603260.
- [65] N. Gasparini, A. Gregori, M. Salvador, M. Biele, A. Wadsworth, S. Tedde, D. Baran, I. McCulloch, C. J. Brabec, *Adv. Mater. Technol.* **2018**, *3*, 1800104.
- [66] M. Punke, S. Valouch, S. W. Kettlitz, M. Gerken, U. Lemmer, *J. Lightwave Technol.* **2008**, *26*, 816.
- [67] X. Gong, M.-H. Tong, S. H. Park, M. Liu, A. Jen, A. J. Heeger, *Sensors* **2010**, *10*, 6488.
- [68] D. Yang, X. Zhou, D. Ma, A. Vadim, T. Ahamad, S. M. Alshehri, *Mater. Horiz.* **2018**, *5*, 874.
- [69] S. Tedde, E. S. Zaus, J. Furst, D. Henseler, P. Lugli, *IEEE Electron Device Lett.* **2007**, *28*, 893.
- [70] T. Rauch, M. Böberl, S. F. Tedde, J. Fürst, M. V. Kovalenko, G. Hesser, U. Lemmer, W. Heiss, O. Hayden, *Nat. Photonics* **2009**, *3*, 332.
- [71] R. D. Jansen-van Vuuren, A. Armin, A. K. Pandey, P. L. Burn, P. Meredith, *Adv. Mater.* **2016**, *28*, 4766.
- [72] Y. Yao, Y. Liang, V. Shrotriya, S. Xiao, L. Yu, Y. Yang, *Adv. Mater.* **2007**, *19*, 3979.
- [73] K. S. Nalwa, Y. Cai, A. L. Thoeming, J. Shinar, R. Shinar, S. Chaudhary, *Adv. Mater.* **2010**, *22*, 4157.
- [74] R. C. Evans, P. Douglas, H. D. Burrows, (Ed.), *Applied Photochemistry*, Springer, Dordrecht **2013**.
- [75] J. Roncali, *Macromol. Rapid Commun.* **2007**, *28*, 1761.
- [76] S. Lois, J.-C. Florès, J.-P. Lère-Porte, F. Serein-Spirau, J. J. E. Moreau, K. Miqueu, J.-M. Sotiropoulos, P. Baylère, M. Tillard, C. Belin, *Eur. J. Org. Chem.* **2007**, 4019.
- [77] S. C. Rasmussen, S. J. Evenson, C. B. McCausland, *Chem. Commun.* **2015**, *51*, 4528.
- [78] P. Alemany, D. Casanova, C. Dryzun, *Chem. Eur. J.* **2011**, *17*, 14896.
- [79] J. L. Brédas, *J. Chem. Phys.* **1985**, *82*, 3808.
- [80] J. Fleischhauer, S. Zahn, R. Beckert, U.-W. Grummt, E. Birckner, H. Görls, *Chem. Eur. J.* **2012**, *18*, 4549.
- [81] K. Kawabata, M. Saito, I. Osaka, K. Takimiya, *J. Am. Chem. Soc.* **2016**, *138*, 7725.
- [82] S. Hedström, E. Wang, P. Persson, *Mol. Phys.* **2017**, *115*, 485.
- [83] X. Xu, C. Wang, O. Bäcke, D. I. James, K. Bini, E. Olsson, M. R. Andersson, M. Fahlman, E. Wang, *Polym. Chem.* **2015**, *6*, 4624.
- [84] C. Kitamura, S. Tanaka, Y. Yamashita, *Chem. Mater.* **1996**, *8*, 570.
- [85] D. I. James, S. Wang, W. Ma, S. Hedström, X. Meng, P. Persson, S. Fabiano, X. Crispin, M. R. Andersson, M. Berggren, E. Wang, *Adv. Electron. Mater.* **2016**, *2*, 1500313.
- [86] S. Hedström, Q. Tao, E. Wang, P. Persson, *Phys. Chem. Chem. Phys.* **2015**, *17*, 26677.
- [87] Q. Tao, Y. Xia, X. Xu, S. Hedström, O. Bäcke, D. I. James, P. Persson, E. Olsson, O. Inganäs, L. Hou, W. Zhu, E. Wang, *Macromolecules* **2015**, *48*, 1009.
- [88] S. Ellinger, K. R. Graham, P. Shi, R. T. Farley, T. T. Steckler, R. N. Brookins, P. Taranekar, J. Mei, L. A. Padilha, T. R. Ensley, H. Hu, S. Webster, D. J. Hagan, E. W. Van Stryland, K. S. Schanze, J. R. Reynolds, *Chem. Mater.* **2011**, *23*, 3805.

- [89] A. Zampetti, A. Minotto, B. M. Squeo, V. G. Gregoriou, S. Allard, U. Scherf, C. L. Chochos, F. Cacialli, *Sci. Rep.* **2017**, *7*, 1611.
- [90] J. M. Toussaint, J. L. Brédas, *Synth. Met.* **1992**, *46*, 325.
- [91] J. Torras, J. Casanovas, C. Alemán, *J. Phys. Chem. A* **2012**, *116*, 7571.
- [92] S. Hedström, P. Henriksson, E. Wang, M. R. Andersson, P. Persson, *Phys. Chem. Chem. Phys.* **2014**, *16*, 24853.
- [93] R. E. Larsen, *J. Phys. Chem. C* **2016**, *120*, 9650.
- [94] J. L. Bredas, R. Silbey, D. S. Boudreaux, R. R. Chance, *J. Am. Chem. Soc.* **1983**, *105*, 6555.
- [95] X. Guo, M. Baumgarten, K. Müllen, *Prog. Polym. Sci.* **2013**, *38*, 1832.
- [96] G. W. P. van Pruissen, J. Brebels, K. H. Hendriks, M. M. Wienk, R. A. J. Janssen, *Macromolecules* **2015**, *48*, 2435.
- [97] Y. Guo, M. Li, Y. Zhou, J. Song, Z. Bo, H. Wang, *Macromolecules* **2017**, *50*, 7984.
- [98] A. D. McNaught, A. Wilkinson, *IUPAC. Compendium of Chemical Terminology (the "Gold Book")*, 2nd Ed., Blackwell Scientific Publications, Oxford **1997**.
- [99] P. I. Djurovich, E. I. Mayo, S. R. Forrest, M. E. Thompson, *Org. Electron.* **2009**, *10*, 515.
- [100] J.-L. Bredas, *Mater. Horiz.* **2014**, *1*, 17.
- [101] P. Atkins, R. Friedman, *Molecular Quantum Mechanics*, 4th Ed., Oxford University Press, New York **2005**.
- [102] A. J. Cohen, P. Mori-Sánchez, W. Yang, *Chem. Rev.* **2012**, *112*, 289.
- [103] T. Körzdörfer, J. S. Sears, C. Sutton, J.-L. Brédas, *J. Chem. Phys.* **2011**, *135*, 204107.
- [104] T. Körzdörfer, J.-L. Brédas, *Acc. Chem. Res.* **2014**, *47*, 3284.
- [105] H. Sun, Z. Hu, C. Zhong, X. Chen, Z. Sun, J.-L. Brédas, *J. Phys. Chem. Lett.* **2017**, *8*, 2393.
- [106] Z. C. Wong, W. Y. Fan, T. S. Chwee, M. B. Sullivan, *Phys. Chem. Chem. Phys.* **2017**, *19*, 21046.
- [107] S. M. Tadayyon, H. M. Grandin, K. Griffiths, L. L. Coatsworth, P. R. Norton, H. Aziz, Z. D. Popovic, *Org. Electron.* **2004**, *5*, 199.
- [108] D. Cahen, A. Kahn, *Adv. Mater.* **2003**, *15*, 271.
- [109] K. Seki, K. Kanai, *Mol. Cryst. Liq. Cryst.* **2006**, *455*, 145.
- [110] G. A. Mabbott, *J. Chem. Educ.* **1983**, *60*, 697.
- [111] P. T. Kissinger, W. R. Heineman, *J. Chem. Educ.* **1983**, *60*, 702.
- [112] T. Johansson, W. Mammo, M. Svensson, M. R. Andersson, O. Inganäs, *J. Mater. Chem.* **2003**, *13*, 1316.
- [113] N. G. Connelly, W. E. Geiger, *Chem. Rev.* **1996**, *96*, 877.
- [114] C. M. Cardona, W. Li, A. E. Kaifer, D. Stockdale, G. C. Bazan, *Adv. Mater.* **2011**, *23*, 2367.
- [115] A. J. Bard, L. R. Faulkner, *Electrochemical Methods: Fundamentals and Applications*, 2nd Ed., Wiley, New York **2001**.
- [116] N. Elgrishi, K. J. Rountree, B. D. McCarthy, E. S. Rountree, T. T. Eisenhart, J. L. Dempsey, *J. Chem. Educ.* **2018**, *95*, 197.
- [117] C. P. Andrieux, P. Hapiot, J. M. Savéant, *J. Electroanal. Chem.* **1993**, *349*, 299.
- [118] R. S. Nicholson, *Anal. Chem.* **1966**, *38*, 1406.
- [119] L. L. Miller, G. D. Nordblom, E. A. Mayeda, *J. Org. Chem.* **1972**, *37*, 916.

- [120] A. Maccoll, *Nature* **1949**, *163*, 178.
- [121] V. V. Pavlishchuk, A. W. Addison, *Inorg. Chim. Acta* **2000**, *298*, 97.
- [122] X. Xu, Z. Li, J. Wang, B. Lin, W. Ma, Y. Xia, M. R. Andersson, R. A. J. Janssen, E. Wang, *Nano Energy* **2018**, *45*, 368.
- [123] O. Stier, M. Grundmann, D. Bimberg, *Phys. Rev. B* **1999**, *59*, 5688.
- [124] B. Yang, J. Cox, Y. Yuan, F. Guo, J. Huang, *Appl. Phys. Lett.* **2011**, *99*, 133302.
- [125] L. Kronik, T. Stein, S. Refaely-Abramson, R. Baer, *J. Chem. Theory Comput.* **2012**, *8*, 1515.
- [126] M. Sauer, J. Hofkens, J. Enderlein, *Handbook of Fluorescence Spectroscopy and Imaging: From Single Molecules to Ensembles*, Wiley-VCH Verlag GmbH & Co. KGaA, Weinheim **2011**.
- [127] E. R. Williams, R. L. Steiner, D. B. Newell, P. T. Olsen, *Phys. Rev. Lett.* **1998**, *81*, 2404.
- [128] J. C. S. Costa, R. J. S. Taveira, C. F. R. A. C. Lima, A. Mendes, L. M. N. B. F. Santos, *Opt. Mater.* **2016**, *58*, 51.
- [129] J. R. Lakowicz, *Principles of Fluorescence Spectroscopy*, 3rd Ed., Springer, New York **2006**.
- [130] C.-P. Chen, S.-H. Chan, T.-C. Chao, C. Ting, B.-T. Ko, *J. Am. Chem. Soc.* **2008**, *130*, 12828.
- [131] W. S. Yoon, D. W. Kim, J.-M. Park, I. Cho, O. K. Kwon, D. R. Whang, J. H. Kim, J.-H. Park, S. Y. Park, *Macromolecules* **2016**, *49*, 8489.
- [132] Y. Yang, Z.-G. Zhang, H. Bin, S. Chen, L. Gao, L. Xue, C. Yang, Y. Li, *J. Am. Chem. Soc.* **2016**, *138*, 15011.
- [133] V. Schmiedova, P. Heinrichova, O. Zmeskal, M. Weiter, *Appl. Surf. Sci.* **2015**, *349*, 582.
- [134] M. Montalti, A. Credi, L. Prodi, M. T. Gandolfi, *Handbook of Photochemistry*, 3rd Ed., CRC Press, Boca Raton **2006**.
- [135] K. Rurack, M. Spieles, *Anal. Chem.* **2011**, *83*, 1232.
- [136] L. Porrès, A. Holland, L.-O. Pålsson, A. P. Monkman, C. Kemp, A. Beeby, *J. Fluoresc.* **2006**, *16*, 267.
- [137] C. Würth, M. Grabolle, J. Pauli, M. Spieles, U. Resch-Genger, *Nat. Protoc.* **2013**, *8*, 1535.
- [138] S. Sinha, C. Rothe, A. Beeby, L. E. Horsburgh, A. P. Monkman, *J. Chem. Phys.* **2002**, *117*, 2332.
- [139] P. Atkins, J. de Paula, R. Friedman, *Physical Chemistry: Quanta, Matter, and Change*, 2nd Ed., Oxford University Press, Oxford **2014**.
- [140] B. Brocklehurst, *Nature* **1969**, *221*, 921.
- [141] J. Wang, A. Chepelianskii, F. Gao, N. C. Greenham, *Nat. Commun.* **2012**, *3*, 1191.
- [142] W. Ratzke, L. Schmitt, H. Matsuoka, C. Bannwarth, M. Retegan, S. Bange, P. Klemm, F. Neese, S. Grimme, O. Schiemann, J. M. Lupton, S. Höger, *J. Phys. Chem. Lett.* **2016**, *7*, 4802.
- [143] B. Hu, L. Yan, M. Shao, *Adv. Mater.* **2009**, *21*, 1500.
- [144] J. S. Wilson, N. Chawdhury, M. R. A. Al-Mandhary, M. Younus, M. S. Khan, P. R. Raithby, A. Köhler, R. H. Friend, *J. Am. Chem. Soc.* **2001**, *123*, 9412.

- [145] J. S. Wilson, A. S. Dhoot, A. J. A. B. Seeley, M. S. Khan, A. Köhler, R. H. Friend, *Nature* **2001**, *413*, 828.
- [146] H. Yersin, R. Czerwieniec, M. Z. Shafikov, A. F. Suleymanova, *ChemPhysChem* **2017**, *18*, 3508.
- [147] H. Langhals, J. Karolin, L. B.-Å. Johansson, *J. Chem. Soc., Faraday Trans.* **1998**, *94*, 2919.
- [148] S. Kalinin, M. Speckbacher, H. Langhals, L. B. Å. Johansson, *Phys. Chem. Chem. Phys.* **2001**, *3*, 172.
- [149] H. F. Wittmann, R. H. Friend, M. S. Khan, J. Lewis, *J. Chem. Phys.* **1994**, *101*, 2693.
- [150] H. Yersin, A. F. Rausch, R. Czerwieniec, T. Hofbeck, T. Fischer, *Coord. Chem. Rev.* **2011**, *255*, 2622.
- [151] Y. Zhang, S. R. Forrest, *Chem. Phys. Lett.* **2013**, *590*, 106.
- [152] H. van Eersel, P. A. Bobbert, R. A. J. Janssen, R. Coehoorn, *J. Appl. Phys.* **2016**, *119*, 163102.
- [153] T. Sajoto, P. I. Djurovich, A. B. Tamayo, J. Oxgaard, W. A. Goddard, M. E. Thompson, *J. Am. Chem. Soc.* **2009**, *131*, 9813.
- [154] T. Hofbeck, H. Yersin, *Inorg. Chem.* **2010**, *49*, 9290.
- [155] E. Stanislovaityte, J. Simokaitiene, S. Raisys, H. Al-Attar, J. V. Grazulevicius, A. P. Monkman, V. Jankus, *J. Mater. Chem. C* **2013**, *1*, 8209.
- [156] N. Altınölçek, M. Aydemir, M. Tavaslı, P. L. Dos Santos, A. P. Monkman, *J. Organomet. Chem.* **2017**, *851*, 184.
- [157] K. Tuong Ly, R.-W. Chen-Cheng, H.-W. Lin, Y.-J. Shiau, S.-H. Liu, P.-T. Chou, C.-S. Tsao, Y.-C. Huang, Y. Chi, *Nat. Photon.* **2017**, *11*, 63.
- [158] H. Benjamin, M. A. Fox, A. S. Batsanov, H. A. Al-Attar, C. Li, Z. Ren, A. P. Monkman, M. R. Bryce, *Dalton Trans.* **2017**, *46*, 10996.
- [159] S. Y. Lee, T. Yasuda, H. Komiyama, J. Lee, C. Adachi, *Adv. Mater.* **2016**, *28*, 4019.
- [160] X.-K. Chen, Y. Tsuchiya, Y. Ishikawa, C. Zhong, C. Adachi, J.-L. Brédas, *Adv. Mater.* **2017**, *29*, 1702767.
- [161] A. Endo, M. Ogasawara, A. Takahashi, D. Yokoyama, Y. Kato, C. Adachi, *Adv. Mater.* **2009**, *21*, 4802.
- [162] A. Endo, K. Sato, K. Yoshimura, T. Kai, A. Kawada, H. Miyazaki, C. Adachi, *Appl. Phys. Lett.* **2011**, *98*, 083302.
- [163] H. Tanaka, K. Shizu, H. Miyazaki, C. Adachi, *Chem. Commun.* **2012**, *48*, 11392.
- [164] H. Uoyama, K. Goushi, K. Shizu, H. Nomura, C. Adachi, *Nature* **2012**, *492*, 234.
- [165] P. L. dos Santos, J. S. Ward, M. R. Bryce, A. P. Monkman, *J. Phys. Chem. Lett.* **2016**, *7*, 3341.
- [166] F. B. Dias, J. Santos, D. R. Graves, P. Data, R. S. Nobuyasu, M. A. Fox, A. S. Batsanov, T. Palmeira, M. N. Berberan-Santos, M. R. Bryce, A. P. Monkman, *Adv. Sci.* **2016**, *3*, 1600080.
- [167] M. K. Etherington, J. Gibson, H. F. Higginbotham, T. J. Penfold, A. P. Monkman, *Nat. Commun.* **2016**, *7*, 13680.
- [168] T. J. Penfold, F. B. Dias, A. P. Monkman, *Chem. Commun.* **2018**, *54*, 3926.
- [169] P. L. dos Santos, M. K. Etherington, A. P. Monkman, *J. Mater. Chem. C* **2018**, *6*, 4842.
- [170] R. S. Nobuyasu, Z. Ren, G. C. Griffiths, A. S. Batsanov, P. Data, S. Yan, A. P. Monkman, M. R. Bryce, F. B. Dias, *Adv. Optical Mater.* **2016**, *4*, 597.

- [171] J. Gibson, A. P. Monkman, T. J. Penfold, *ChemPhysChem* **2016**, *17*, 2956.
- [172] F. B. Dias, K. N. Bourdakos, V. Jankus, K. C. Moss, K. T. Kamtekar, V. Bhalla, J. Santos, M. R. Bryce, A. P. Monkman, *Adv. Mater.* **2013**, *25*, 3707.
- [173] V. Jankus, P. Data, D. Graves, C. McGuinness, J. Santos, M. R. Bryce, F. B. Dias, A. P. Monkman, *Adv. Funct. Mater.* **2014**, *24*, 6178.
- [174] L.-S. Cui, Y.-M. Xie, Y.-K. Wang, C. Zhong, Y.-L. Deng, X.-Y. Liu, Z.-Q. Jiang, L.-S. Liao, *Adv. Mater.* **2015**, *27*, 4213.
- [175] P. L. dos Santos, J. S. Ward, D. G. Congrave, A. S. Batsanov, J. Eng, J. E. Stacey, T. J. Penfold, A. P. Monkman, M. R. Bryce, *Adv. Sci.* **2018**, *5*, 1700989.
- [176] K. Walzer, B. Maennig, M. Pfeiffer, K. Leo, *Chem. Rev.* **2007**, *107*, 1233.
- [177] H. T. Nicolai, A. Hof, J. L. M. Oosthoek, P. W. M. Blom, *Adv. Funct. Mater.* **2011**, *21*, 1505.
- [178] B. Minaev, G. Baryshnikov, H. Agren, *Phys. Chem. Chem. Phys.* **2014**, *16*, 1719.
- [179] B. Geffroy, P. le Roy, C. Prat, *Polym. Int.* **2006**, *55*, 572.
- [180] Y. Sun, C. Borek, K. Hanson, P. I. Djurovich, M. E. Thompson, J. Brooks, J. J. Brown, S. R. Forrest, *Appl. Phys. Lett.* **2007**, *90*, 213503.
- [181] N. C. Giebink, S. R. Forrest, *Phys. Rev. B* **2008**, *77*, 235215.
- [182] J. R. Sommer, R. T. Farley, K. R. Graham, Y. Yang, J. R. Reynolds, J. Xue, K. S. Schanze, *ACS Appl. Mater. Interfaces* **2009**, *1*, 274.
- [183] K. R. Graham, Y. Yang, J. R. Sommer, A. H. Shelton, K. S. Schanze, J. Xue, J. R. Reynolds, *Chem. Mater.* **2011**, *23*, 5305.
- [184] G. Gu, D. Z. Garbuzov, P. E. Burrows, S. Venkatesh, S. R. Forrest, M. E. Thompson, *Opt. Lett.* **1997**, *22*, 396.
- [185] C. F. Madigan, M.-H. Lu, J. C. Sturm, *Appl. Phys. Lett.* **2000**, *76*, 1650.
- [186] C.-Y. Chen, W.-K. Lee, Y.-J. Chen, C.-Y. Lu, H. Y. Lin, C.-C. Wu, *Adv. Mater.* **2015**, *27*, 4883.
- [187] T. Yamasaki, K. Sumioka, T. Tsutsui, *Appl. Phys. Lett.* **2000**, *76*, 1243.
- [188] J. Lim, S. S. Oh, D. Y. Kim, S. H. Cho, I. T. Kim, S. H. Han, H. Takezoe, E. H. Choi, G. S. Cho, Y. H. Seo, S. O. Kang, B. Park, *Opt. Express* **2006**, *14*, 6564.
- [189] S. Möller, S. R. Forrest, *J. Appl. Phys.* **2002**, *91*, 3324.
- [190] N. Kaihiovirta, C. Larsen, L. Edman, *ACS Appl. Mater. Interfaces* **2014**, *6*, 2940.
- [191] K. Saxena, V. K. Jain, D. S. Mehta, *Opt. Mater.* **2009**, *32*, 221.
- [192] W. Brütting, J. Frischeisen, T. D. Schmidt, B. J. Scholz, C. Mayr, *Phys. Status Solidi A* **2013**, *210*, 44.
- [193] Z. Kafafi (Ed.), *Organic Electroluminescence*, CRC Press, Boca Raton **2005**.
- [194] G. Tregnago, T. T. Steckler, O. Fenwick, M. R. Andersson, F. Cacialli, *J. Mater. Chem. C* **2015**, *3*, 2792.
- [195] S. Tang, L. Edman, *Top. Curr. Chem.* **2016**, *374*, 40.
- [196] J. C. deMello, N. Tessler, S. C. Graham, R. H. Friend, *Phys. Rev. B* **1998**, *57*, 12951.
- [197] S. B. Meier, S. van Reenen, B. Lefevre, D. Hartmann, H. J. Bolink, A. Winnacker, W. Sarfert, M. Kemerink, *Adv. Funct. Mater.* **2013**, *23*, 3531.
- [198] J. Gao, J. Dane, *Appl. Phys. Lett.* **2004**, *84*, 2778.
- [199] J. Fang, Y. Yang, L. Edman, *Appl. Phys. Lett.* **2008**, *93*, 063503.
- [200] S. van Reenen, P. Matyba, A. Dzwilewski, R. A. J. Janssen, L. Edman, M. Kemerink, *J. Am. Chem. Soc.* **2010**, *132*, 13776.

- [201] D. A. W. Ross, P. A. Scattergood, A. Babaei, A. Pertegás, H. J. Bolink, P. I. P. Elliott, *Dalton Trans.* **2016**, 45, 7748.
- [202] J.-H. Hsu, H.-C. Su, *Phys. Chem. Chem. Phys.* **2016**, 18, 5034.
- [203] B. Nemati Bideh, H. Shahroosvand, *Sci. Rep.* **2017**, 7, 15739.
- [204] S. Tang, J. Pan, H. A. Buchholz, L. Edman, *J. Am. Chem. Soc.* **2013**, 135, 3647.
- [205] K. J. Chee, V. Kumar, C. V. Nguyen, J. Wang, P. S. Lee, *J. Phys. Chem. C* **2016**, 120, 11324.
- [206] P. Lundberg, E. M. Lindh, S. Tang, L. Edman, *ACS Appl. Mater. Interfaces* **2017**, 9, 28810.
- [207] C.-T. Liao, H.-F. Chen, H.-C. Su, K.-T. Wong, *J. Mater. Chem.* **2011**, 21, 17855.
- [208] F. AlTal, J. Gao, *Org. Electron.* **2015**, 18, 1.
- [209] J. Mindemark, S. Tang, J. Wang, N. Kaihovirta, D. Brandell, L. Edman, *Chem. Mater.* **2016**, 28, 2618.
- [210] C. Larsen, R. Forchheimer, L. Edman, D. Tu, *Org. Electron.* **2017**, 45, 57.
- [211] J. E. Namanga, N. Gerlitzki, A.-V. Mudring, *Adv. Funct. Mater.* **2017**, 27, 1605588.
- [212] K.-J. Baeg, M. Binda, D. Natali, M. Caironi, Y.-Y. Noh, *Adv. Mater.* **2013**, 25, 4267.
- [213] M. Kielar, O. Dhez, G. Pecastaings, A. Curutchet, L. Hirsch, *Sci. Rep.* **2016**, 6, 39201.
- [214] B. Nabet (Ed.), *Photodetectors: Materials, Devices and Applications*, Woodhead Publishing, Oxford **2016**.
- [215] L. Dou, Y. Yang, J. You, Z. Hong, W.-H. Chang, G. Li, Y. Yang, *Nat. Commun.* **2014**, 5, 5404.
- [216] G. Konstantatos, I. Howard, A. Fischer, S. Hoogland, J. Clifford, E. Klem, L. Levina, E. H. Sargent, *Nature* **2006**, 442, 180.
- [217] G. Sarasqueta, K. R. Choudhury, J. Subbiah, F. So, *Adv. Funct. Mater.* **2011**, 21, 167.
- [218] H. Shekhar, O. Solomeshch, D. Liraz, N. Tessler, *Appl. Phys. Lett.* **2017**, 111, 223301.
- [219] P. E. Keivanidis, S.-H. Khong, P. K. H. Ho, N. C. Greenham, R. H. Friend, *Appl. Phys. Lett.* **2009**, 94, 173303.
- [220] M. Binda, A. Iacchetti, D. Natali, L. Beverina, M. Sassi, M. Sampietro, *Appl. Phys. Lett.* **2011**, 98, 073303.
- [221] S. Xiong, L. Li, F. Qin, L. Mao, B. Luo, Y. Jiang, Z. Li, J. Huang, Y. Zhou, *ACS Appl. Mater. Interfaces* **2017**, 9, 9176.
- [222] R. Englman, J. Jortner, *Mol. Phys.* **1970**, 18, 145.
- [223] J. V. Caspar, B. P. Sullivan, E. M. Kober, T. J. Meyer, *Chem. Phys. Lett.* **1982**, 91, 91.
- [224] Q. Zhao, J. Z. Sun, *J. Mater. Chem. C* **2016**, 4, 10588.
- [225] Y. Zhang, Y. Wang, J. Song, J. Qu, B. Li, W. Zhu, W.-Y. Wong, *Adv. Optical Mater.* **2018**, 1800466.
- [226] Z. He, L. Zhang, J. Mei, T. Zhang, J. W. Y. Lam, Z. Shuai, Y. Q. Dong, B. Z. Tang, *Chem. Mater.* **2015**, 27, 6601.
- [227] S. Baysec, E. Preis, S. Allard, U. Scherf, *Macromol. Rapid Commun.* **2016**, 37, 1802.
- [228] L. Yu, Z. Wu, G. Xie, C. Zhong, Z. Zhu, D. Ma, C. Yang, *Chem. Commun.* **2018**, 54, 1379.
- [229] P. Ledwon, P. Zassowski, T. Jarosz, M. Lapkowski, P. Wagner, V. Cherpak, P. Stakhira, *J. Mater. Chem. C* **2016**, 4, 2219.
- [230] H. Nakanotani, T. Higuchi, T. Furukawa, K. Masui, K. Morimoto, M. Numata, H. Tanaka, Y. Sagara, T. Yasuda, C. Adachi, *Nat. Commun.* **2014**, 5, 4016.

- [231] Y. Tao, K. Yuan, T. Chen, P. Xu, H. Li, R. Chen, C. Zheng, L. Zhang, W. Huang, *Adv. Mater.* **2014**, *26*, 7931.
- [232] P. Data, P. Pander, M. Okazaki, Y. Takeda, S. Minakata, A. P. Monkman, *Angew. Chem. Int. Ed.* **2016**, *55*, 5739.
- [233] W. Zeng, H.-Y. Lai, W.-K. Lee, M. Jiao, Y.-J. Shiu, C. Zhong, S. Gong, T. Zhou, G. Xie, M. Sarma, K.-T. Wong, C.-C. Wu, C. Yang, *Adv. Mater.* **2018**, *30*, 1704961.
- [234] L. Yu, Z. Wu, G. Xie, W. Zeng, D. Ma, C. Yang, *Chem. Sci.* **2018**, *9*, 1385.
- [235] L. Yao, S. Zhang, R. Wang, W. Li, F. Shen, B. Yang, Y. Ma, *Angew. Chem. Int. Ed.* **2014**, *53*, 2119.
- [236] S. Wang, X. Yan, Z. Cheng, H. Zhang, Y. Liu, Y. Wang, *Angew. Chem. Int. Ed.* **2015**, *54*, 13068.
- [237] J. Xue, C. Li, L. Xin, L. Duan, J. Qiao, *Chem. Sci.* **2016**, *7*, 2888.
- [238] J. Xue, Q. Liang, Y. Zhang, R. Zhang, L. Duan, J. Qiao, *Adv. Funct. Mater.* **2017**, *27*, 1703283.
- [239] T. Liu, L. Zhu, C. Zhong, G. Xie, S. Gong, J. Fang, D. Ma, C. Yang, *Adv. Funct. Mater.* **2017**, *27*, 1606384.
- [240] Y. Yuan, Y. Hu, Y.-X. Zhang, J.-D. Lin, Y.-K. Wang, Z.-Q. Jiang, L.-S. Liao, S.-T. Lee, *Adv. Funct. Mater.* **2017**, *27*, 1700986.
- [241] D.-H. Kim, A. D'Aléo, X.-K. Chen, A. D. S. Sandanayaka, D. Yao, L. Zhao, T. Komino, E. Zaborova, G. Canard, Y. Tsuchiya, E. Choi, J. W. Wu, F. Fages, J.-L. Brédas, J.-C. Ribierre, C. Adachi, *Nat. Photon.* **2018**, *12*, 98.
- [242] H. Xiang, J. Cheng, X. Ma, X. Zhou, J. J. Chruma, *Chem. Soc. Rev.* **2013**, *42*, 6128.
- [243] T. T. Steckler, O. Fenwick, T. Lockwood, M. R. Andersson, F. Cacialli, *Macromol. Rapid Commun.* **2013**, *34*, 990.
- [244] Y. Dong, W. Cai, X. Hu, C. Zhong, F. Huang, Y. Cao, *Polymer* **2012**, *53*, 1465.
- [245] T. L. D. Tam, W. Ye, H. H. R. Tan, F. Zhou, H. Su, S. G. Mhaisalkar, A. C. Grimsdale, *J. Org. Chem.* **2012**, *77*, 10035.
- [246] D. G. Patel, F. Feng, Y.-y. Ohnishi, K. A. Abboud, S. Hirata, K. S. Schanze, J. R. Reynolds, *J. Am. Chem. Soc.* **2012**, *134*, 2599.
- [247] Y. Dong, W. Cai, M. Wang, Q. Li, L. Ying, F. Huang, Y. Cao, *Org. Electron.* **2013**, *14*, 2459.
- [248] T. Vangerven, P. Verstappen, J. Drijkoningen, W. Dierckx, S. Himmelberger, A. Salleo, D. Vanderzande, W. Maes, J. V. Manca, *Chem. Mater.* **2015**, *27*, 3726.
- [249] J. Brebels, K. C. C. W. S. Klider, M. Kelchtermans, P. Verstappen, M. Van Landeghem, S. Van Doorslaer, E. Goovaerts, J. R. Garcia, J. Manca, L. Lutsen, D. Vanderzande, W. Maes, *Org. Electron.* **2017**, *50*, 264.
- [250] D. Chen, Y. Zhao, C. Zhong, S. Gao, G. Yu, Y. Liu, J. Qin, *J. Mater. Chem.* **2012**, *22*, 14639.
- [251] S. Beaupré, A. Pron, S. H. Drouin, A. Najari, L. G. Mercier, A. Robitaille, M. Leclerc, *Macromolecules* **2012**, *45*, 6906.
- [252] A. Petrozza, S. Brovelli, J. J. Michels, H. L. Anderson, R. H. Friend, C. Silva, F. Cacialli, *Adv. Mater.* **2008**, *20*, 3218.
- [253] L. Zhang, S. Hu, J. Chen, Z. Chen, H. Wu, J. Peng, Y. Cao, *Adv. Funct. Mater.* **2011**, *21*, 3760.

- [254] O. Fenwick, S. Fusco, T. N. Baig, F. Di Stasio, T. T. Steckler, P. Henriksson, C. Fléchon, M. R. Andersson, F. Cacialli, *APL Mater.* **2013**, *1*, 032108.
- [255] R. Noriega, J. Rivnay, K. Vandewal, F. P. V. Koch, N. Stingelin, P. Smith, M. F. Toney, A. Salleo, *Nat. Mater.* **2013**, *12*, 1038.
- [256] G. Latini, A. Downes, O. Fenwick, A. Ambrosio, M. Allegrini, C. Daniel, C. Silva, P. G. Gucciardi, S. Patanè, R. Daik, W. J. Feast, F. Cacialli, *Appl. Phys. Lett.* **2005**, *86*, 011102.
- [257] X. Gao, B. Hu, G. Tu, *Org. Electron.* **2014**, *15*, 1440.
- [258] T. T. Steckler, M. J. Lee, Z. Chen, O. Fenwick, M. R. Andersson, F. Cacialli, H. Sirringhaus, *J. Mater. Chem. C* **2014**, *2*, 5133.
- [259] Y. Zhang, X. Gao, J. Li, G. Tu, *Dyes Pigm.* **2015**, *120*, 112.
- [260] P. Li, O. Fenwick, S. Yilmaz, D. Breusov, D. J. Caruana, S. Allard, U. Scherf, F. Cacialli, *Chem. Commun.* **2011**, *47*, 8820.
- [261] O. Fenwick, J. K. Sprafke, J. Binas, D. V. Kondratuk, F. Di Stasio, H. L. Anderson, F. Cacialli, *Nano Lett.* **2011**, *11*, 2451.
- [262] M. Sassi, N. Buccheri, M. Rooney, C. Botta, F. Bruni, U. Giovanella, S. Brovelli, L. Beverina, *Sci. Rep.* **2016**, *6*, 34096.
- [263] X. Xu, P. Cai, Y. Lu, N. S. Choon, J. Chen, B. S. Ong, X. Hu, *Macromol. Rapid Commun.* **2013**, *34*, 681.
- [264] D. Dang, W. Chen, S. Himmelberger, Q. Tao, A. Lundin, R. Yang, W. Zhu, A. Salleo, C. Müller, E. Wang, *Adv. Energy Mater.* **2014**, *4*, 1400680.
- [265] W. Li, Y. Pan, L. Yao, H. Liu, S. Zhang, C. Wang, F. Shen, P. Lu, B. Yang, Y. Ma, *Adv. Optical Mater.* **2014**, *2*, 892.
- [266] X. Han, Q. Bai, L. Yao, H. Liu, Y. Gao, J. Li, L. Liu, Y. Liu, X. Li, P. Lu, B. Yang, *Adv. Funct. Mater.* **2015**, *25*, 7521.
- [267] C. E. Housecroft, E. C. Constable, *Coord. Chem. Rev.* **2017**, *350*, 155.
- [268] J. Gao, *Curr. Opin. Electrochem.* **2018**, *7*, 87.
- [269] J. Liang, L. Li, X. Niu, Z. Yu, Q. Pei, *J. Phys. Chem. C* **2013**, *117*, 16632.
- [270] A. Sandström, A. Asadpoordarvish, J. Enevold, L. Edman, *Adv. Mater.* **2014**, *26*, 4975.
- [271] A. Sandström, L. Edman, *Energy Technol.* **2015**, *3*, 329.
- [272] A. K. Pal, D. B. Cordes, A. M. Z. Slawin, C. Momblona, A. Pertegas, E. Orti, H. J. Bolink, E. Zysman-Colman, *RSC Adv.* **2017**, *7*, 31833.
- [273] A. Pertegás, D. Tordera, J. J. Serrano-Pérez, E. Ortí, H. J. Bolink, *J. Am. Chem. Soc.* **2013**, *135*, 18008.
- [274] D. Gedefaw, Y. Zhou, S. Hellström, L. Lindgren, L. M. Andersson, F. Zhang, W. Mammo, O. Inganäs, M. R. Andersson, *J. Mater. Chem.* **2009**, *19*, 5359.
- [275] M. Bolognesi, D. Gedefaw, D. Dang, P. Henriksson, W. Zhuang, M. Tassarolo, E. Wang, M. Muccini, M. Seri, M. R. Andersson, *RSC Adv.* **2013**, *3*, 24543.
- [276] X. Xu, Z. Li, O. Backe, K. Bini, D. I. James, E. Olsson, M. R. Andersson, E. Wang, *J. Mater. Chem. A* **2014**, *2*, 18988.
- [277] E. Wang, J. Bergqvist, K. Vandewal, Z. Ma, L. Hou, A. Lundin, S. Himmelberger, A. Salleo, C. Müller, O. Inganäs, F. Zhang, M. R. Andersson, *Adv. Energy Mater.* **2013**, *3*, 806.
- [278] M. Lafrance, C. N. Rowley, T. K. Woo, K. Fagnou, *J. Am. Chem. Soc.* **2006**, *128*, 8754.

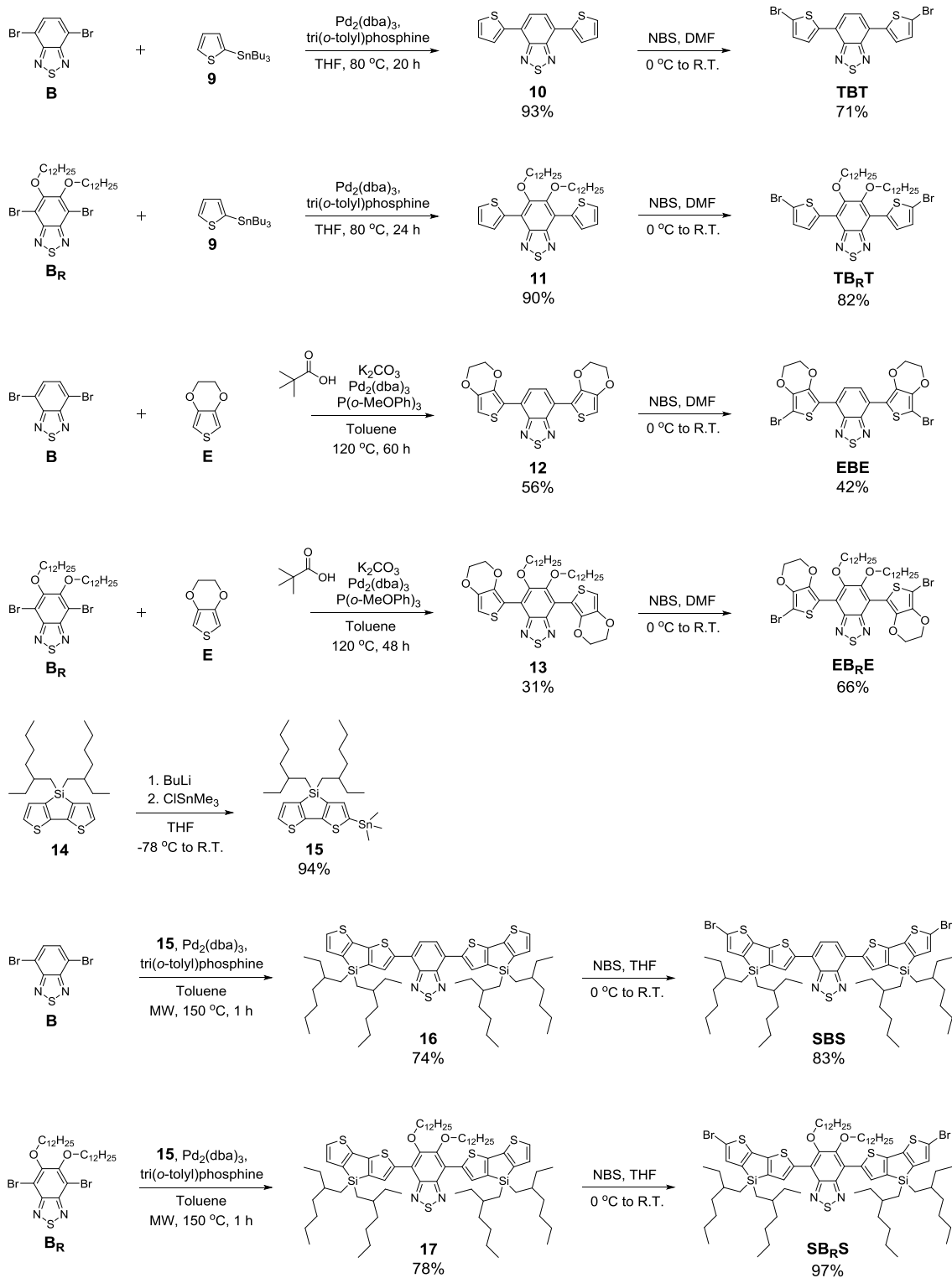
- [279] E. Kloser, S. Böhmendorfer, L. Brecker, H. Kählig, T. Netscher, K. Mereiter, T. Rosenau, *Eur. J. Org. Chem.* **2011**, 2011, 2450.
- [280] M. R. Cargill, G. Sandford, P. Kilickiran, G. Nelles, *Tetrahedron* **2013**, 69, 512.
- [281] S. van Reenen, M. V. Vitorino, S. C. J. Meskers, R. A. J. Janssen, M. Kemerink, *Phys. Rev. B* **2014**, 89, 205206.
- [282] S. van Reenen, R. A. J. Janssen, M. Kemerink, *Adv. Funct. Mater.* **2015**, 25, 3066.
- [283] S. Tang, H. A. Buchholz, L. Edman, *J. Mater. Chem. C* **2015**, 3, 8114.
- [284] K. Yamazaki, J. Kuwabara, T. Kanbara, *Macromol. Rapid Commun.* **2013**, 34, 69.
- [285] S. J. Choi, J. Kuwabara, T. Kanbara, *ACS Sustainable Chem. Eng.* **2013**, 1, 878.
- [286] J. Kudrjasova, R. Herckens, H. Penxten, P. Adriaensens, L. Lutsen, D. Vanderzande, W. Maes, *Org. Biomol. Chem.* **2014**, 12, 4663.
- [287] X. Wang, K. Wang, M. Wang, *Polym. Chem.* **2015**, 6, 1846.
- [288] J. Kudrjasova, J. Kesters, P. Verstappen, J. Brebels, T. Vangerven, I. Cardinaletti, J. Drijkoningen, H. Penxten, J. Manca, L. Lutsen, D. Vanderzande, W. Maes, *J. Mater. Chem. A* **2016**, 4, 791.
- [289] A. Petrone, D. B. Lingerfelt, N. Rega, X. Li, *Phys. Chem. Chem. Phys.* **2014**, 16, 24457.
- [290] W. Zhang, Y. Han, X. Zhu, Z. Fei, Y. Feng, N. D. Treat, H. Faber, N. Stingelin, I. McCulloch, T. D. Anthopoulos, M. Heeney, *Adv. Mater.* **2016**, 28, 3922.
- [291] H. Chen, M. Hurhangee, M. Nikolka, W. Zhang, M. Kirkus, M. Neophytou, S. J. Cryer, D. Harkin, P. Hayoz, M. Abdi-Jalebi, C. R. McNeill, H. Sirringhaus, I. McCulloch, *Adv. Mater.* **2017**, 29, 1702523.
- [292] A. Asadpoordarvish, A. Sandström, C. Larsen, R. Bollström, M. Toivakka, R. Österbacka, L. Edman, *Adv. Funct. Mater.* **2015**, 25, 3238.
- [293] X. Zhou, D. Yang, D. Ma, *Adv. Optical Mater.* **2015**, 3, 1570.
- [294] B. Zhang, M. T. Trinh, B. Fowler, M. Ball, Q. Xu, F. Ng, M. L. Steigerwald, X. Y. Zhu, C. Nuckolls, Y. Zhong, *J. Am. Chem. Soc.* **2016**, 138, 16426.
- [295] C. L. Chochos, S. A. Choulis, *Prog. Polym. Sci.* **2011**, 36, 1326.
- [296] W. Zhang, J. Smith, S. E. Watkins, R. Gysel, M. McGehee, A. Salleo, J. Kirkpatrick, S. Ashraf, T. Anthopoulos, M. Heeney, I. McCulloch, *J. Am. Chem. Soc.* **2010**, 132, 11437.
- [297] J. J. Intemann, K. Yao, H.-L. Yip, Y.-X. Xu, Y.-X. Li, P.-W. Liang, F.-Z. Ding, X. Li, A. K. Y. Jen, *Chem. Mater.* **2013**, 25, 3188.
- [298] R. He, L. Yu, P. Cai, F. Peng, J. Xu, L. Ying, J. Chen, W. Yang, Y. Cao, *Macromolecules* **2014**, 47, 2921.
- [299] C. L. Chochos, A. Katsouras, N. Gasparini, C. Koulogiannis, T. Ameri, C. J. Brabec, A. Avgeropoulos, *Macromol. Rapid Commun.* **2017**, 38, 1600614.
- [300] H. Song, Y. Deng, Y. Gao, Y. Jiang, H. Tian, D. Yan, Y. Geng, F. Wang, *Macromolecules* **2017**, 50, 2344.
- [301] T. Hamasaki, T. Morimune, H. Kajii, S. Minakata, R. Tsuruoka, T. Nagamachi, Y. Ohmori, *Thin Solid Films* **2009**, 518, 548.
- [302] K. A. Mazzi, C. K. Luscombe, *Chem. Soc. Rev.* **2015**, 44, 78.
- [303] C. Montenegro Benavides, M. Biele, O. Schmidt, C. J. Brabec, S. F. Tedde, *IEEE Trans. Electron Devices* **2018**, 65, 1516.

- [304] F. P. García de Arquer, A. Armin, P. Meredith, E. H. Sargent, *Nat. Rev. Mater.* **2017**, *2*, 16100.
- [305] S. F. Tedde, J. Kern, T. Sterzl, J. Fürst, P. Lugli, O. Hayden, *Nano Lett.* **2009**, *9*, 980.
- [306] F. Stöckmann, *Appl. Phys.* **1975**, *7*, 1.
- [307] H. Kang, W. Lee, J. Oh, T. Kim, C. Lee, B. J. Kim, *Acc. Chem. Res.* **2016**, *49*, 2424.
- [308] E. Y. Ko, G. E. Park, J. H. Lee, H. J. Kim, D. H. Lee, H. Ahn, M. A. Uddin, H. Y. Woo, M. J. Cho, D. H. Choi, *ACS Appl. Mater. Interfaces* **2017**, *9*, 8838.
- [309] Q.-Y. Li, J. Xiao, L.-M. Tang, H.-C. Wang, Z. Chen, Z. Yang, H.-L. Yip, Y.-X. Xu, *Org. Electron.* **2017**, *44*, 217.
- [310] Q. Wang, J. Qi, W. Qiao, Z. Y. Wang, *Dyes Pigm.* **2015**, *113*, 160.
- [311] X. Wang, L. Lv, L. Li, Y. Chen, K. Zhang, H. Chen, H. Dong, J. Huang, G. Shen, Z. Yang, H. Huang, *Adv. Funct. Mater.* **2016**, *26*, 6306.
- [312] J. Qi, W. Qiao, X. Zhou, D. Yang, J. Zhang, D. Ma, Z. Y. Wang, *Macromol. Chem. Phys.* **2016**, *217*, 1683.
- [313] L. Hu, W. Qiao, J. Han, X. Zhou, C. Wang, D. Ma, Z. Y. Wang, Y. Li, *Polym. Chem.* **2017**, *8*, 528.
- [314] L. Hu, W. Qiao, X. Zhou, X. Zhang, D. Ma, Y. Li, Z. Y. Wang, *Polymer* **2017**, *114*, 173.
- [315] C. Scharsich, R. H. Lohwasser, M. Sommer, U. Asawapirom, U. Scherf, M. Thelakkat, D. Neher, A. Köhler, *J. Polym. Sci., Part B: Polym. Phys.* **2012**, *50*, 442.
- [316] J.-S. Kim, J.-H. Kim, W. Lee, H. Yu, H. J. Kim, I. Song, M. Shin, J. H. Oh, U. Jeong, T.-S. Kim, B. J. Kim, *Macromolecules* **2015**, *48*, 4339.
- [317] W. Wang, F. Zhang, L. Li, M. Gao, B. Hu, *ACS Appl. Mater. Interfaces* **2015**, *7*, 22660.
- [318] T. Earmme, Y.-J. Hwang, N. M. Murari, S. Subramaniyan, S. A. Jenekhe, *J. Am. Chem. Soc.* **2013**, *135*, 14960.
- [319] Y.-J. Hwang, T. Earmme, B. A. E. Courtright, F. N. Eberle, S. A. Jenekhe, *J. Am. Chem. Soc.* **2015**, *137*, 4424.
- [320] Z. Li, W. Zhang, X. Xu, Z. Genene, D. Di Carlo Rasi, W. Mammo, A. Yartsev, M. R. Andersson, R. A. J. Janssen, E. Wang, *Adv. Energy Mater.* **2017**, *7*, 1602722.
- [321] L. Li, F. Zhang, J. Wang, Q. An, Q. Sun, W. Wang, J. Zhang, F. Teng, *Sci. Rep.* **2015**, *5*, 9181.
- [322] M. K. Etherington, F. Franchello, J. Gibson, T. Northey, J. Santos, J. S. Ward, H. F. Higginbotham, P. Data, A. Kurowska, P. L. Dos Santos, D. R. Graves, A. S. Batsanov, F. B. Dias, M. R. Bryce, T. J. Penfold, A. P. Monkman, *Nat. Commun.* **2017**, *8*, 14987.
- [323] P. Data, A. Swist, M. Lapkowski, J. Soloducho, K. Darowicki, A. P. Monkman, *Electrochim. Acta* **2015**, *184*, 86.
- [324] S. Tang, H. A. Buchholz, L. Edman, *ACS Appl. Mater. Interfaces* **2015**, *7*, 25955.
- [325] J. Wang, S. Tang, A. Sandström, L. Edman, *ACS Appl. Mater. Interfaces* **2015**, *7*, 2784.
- [326] A. J. J. Lennox, G. C. Lloyd-Jones, *Chem. Soc. Rev.* **2014**, *43*, 412.
- [327] J.-L. Brédas, *Chem. Mater.* **2017**, *29*, 477.
- [328] D. Milstein, J. K. Stille, *J. Am. Chem. Soc.* **1978**, *100*, 3636.
- [329] J. K. Stille, *Angew. Chem. Int. Ed. Engl.* **1986**, *25*, 508.
- [330] A. F. Littke, L. Schwarz, G. C. Fu, *J. Am. Chem. Soc.* **2002**, *124*, 6343.
- [331] A. L. Casado, P. Espinet, *J. Am. Chem. Soc.* **1998**, *120*, 8978.
- [332] P. Espinet, A. M. Echavarren, *Angew. Chem. Int. Ed.* **2004**, *43*, 4704.

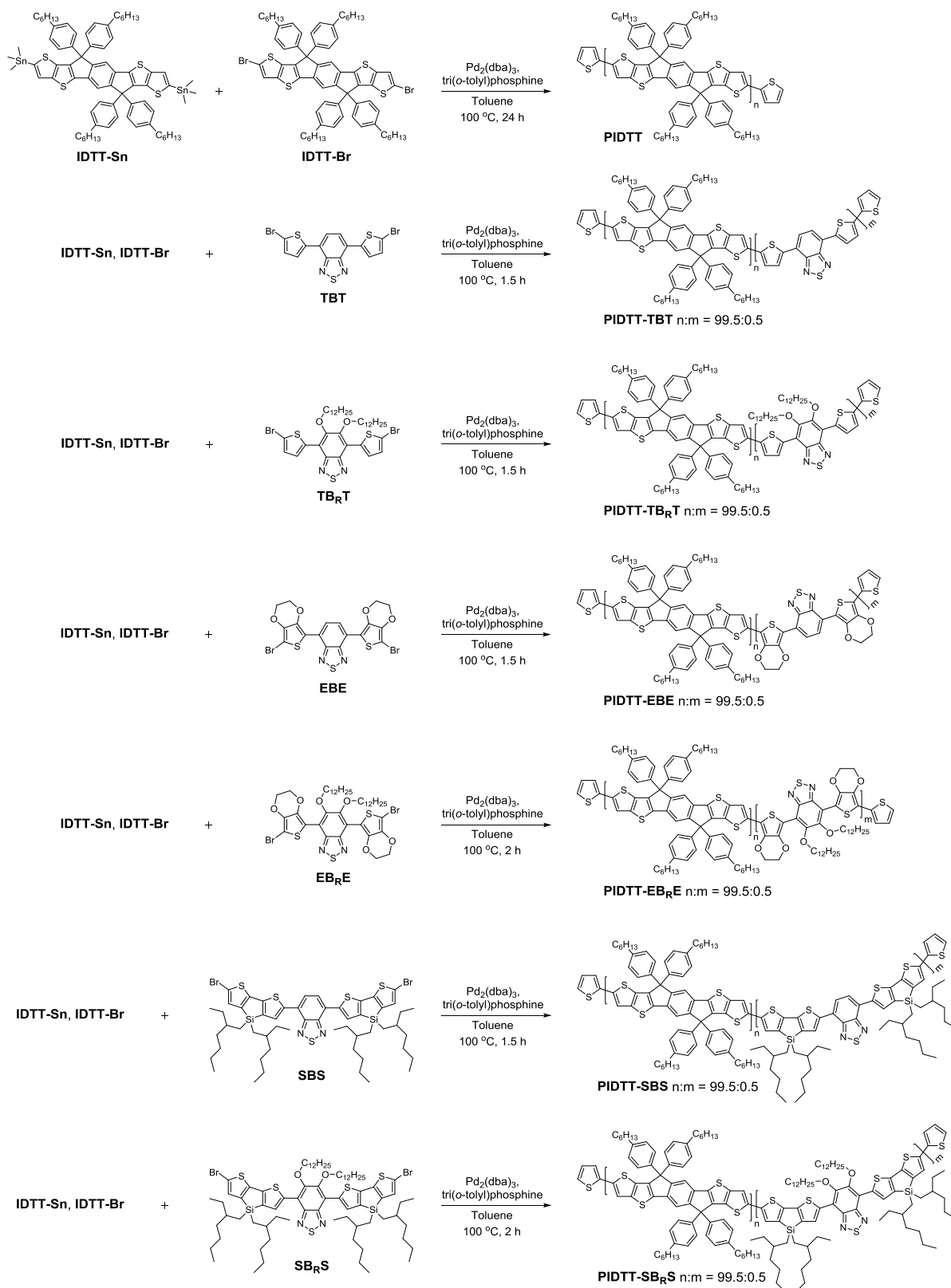
- [333] C. Cordovilla, C. Bartolomé, J. M. Martínez-Ilarduya, P. Espinet, *ACS Catal.* **2015**, *5*, 3040.
- [334] A. Ariafard, Z. Lin, I. J. S. Fairlamb, *Organometallics* **2006**, *25*, 5788.
- [335] K. Vikse, T. Naka, J. S. McIndoe, M. Besora, F. Maseras, *ChemCatChem* **2013**, *5*, 3604.
- [336] V. P. Ananikov, D. G. Musaev, K. Morokuma, *Organometallics* **2005**, *24*, 715.
- [337] M. Pérez-Rodríguez, A. A. C. Braga, M. Garcia-Melchor, M. H. Pérez-Temprano, J. A. Casares, G. Ujaque, A. R. de Lera, R. Álvarez, F. Maseras, P. Espinet, *J. Am. Chem. Soc.* **2009**, *131*, 3650.
- [338] B. Carsten, F. He, H. J. Son, T. Xu, L. Yu, *Chem. Rev.* **2011**, *111*, 1493.
- [339] W. Li, L. Yang, J. R. Tumbleston, L. Yan, H. Ade, W. You, *Adv. Mater.* **2014**, *26*, 4456.
- [340] Y. Zhang, X. Gao, J. Li, G. Tu, *J. Mater. Chem. C* **2015**, *3*, 7463.
- [341] W. Hong, S. Chen, B. Sun, M. A. Arnould, Y. Meng, Y. Li, *Chem. Sci.* **2015**, *6*, 3225.
- [342] G. Pirotte, P. Verstappen, D. Vanderzande, W. Maes, *Adv. Electron. Mater.* **2018**, *4*, 1700481.
- [343] A. L. Casado, J. A. Casares, P. Espinet, *Organometallics* **1997**, *16*, 5730.
- [344] V. Calò, A. Nacci, A. Monopoli, P. Cotugno, *Chem. Eur. J.* **2009**, *15*, 1272.
- [345] A. E. Rudenko, B. C. Thompson, *J. Polym. Sci., Part A: Polym. Chem.* **2015**, *53*, 135.
- [346] R. M. Pankow, L. Ye, N. S. Gobalasingham, N. Salami, S. Samal, B. C. Thompson, *Polym. Chem.* **2018**, *9*, 3885.
- [347] M. Lafrance, K. Fagnou, *J. Am. Chem. Soc.* **2006**, *128*, 16496.
- [348] L. Ackermann, *Chem. Rev.* **2011**, *111*, 1315.
- [349] T. Bura, J. T. Blaskovits, M. Leclerc, *J. Am. Chem. Soc.* **2016**, *138*, 10056.
- [350] M. Lafrance, D. Lapointe, K. Fagnou, *Tetrahedron* **2008**, *64*, 6015.
- [351] B. Biswas, M. Sugimoto, S. Sakaki, *Organometallics* **2000**, *19*, 3895.
- [352] M. García-Melchor, A. A. C. Braga, A. Lledós, G. Ujaque, F. Maseras, *Acc. Chem. Res.* **2013**, *46*, 2626.
- [353] J.-R. Pouliot, F. Grenier, J. T. Blaskovits, S. Beaupré, M. Leclerc, *Chem. Rev.* **2016**, *116*, 14225.
- [354] S. I. Gorelsky, *Organometallics* **2012**, *31*, 4631.
- [355] S. I. Gorelsky, *Coord. Chem. Rev.* **2013**, *257*, 153.
- [356] S. Kowalski, S. Allard, K. Zilberberg, T. Riedl, U. Scherf, *Prog. Polym. Sci.* **2013**, *38*, 1805.
- [357] F. Livi, N. S. Gobalasingham, B. C. Thompson, E. Bundgaard, *J. Polym. Sci., Part A: Polym. Chem.* **2016**, *54*, 2907.
- [358] N. S. Gobalasingham, R. M. Pankow, S. Ekiz, B. C. Thompson, *J. Mater. Chem. A* **2017**, *5*, 14101.
- [359] T. Bura, S. Beaupré, M.-A. Légaré, J. Quinn, E. Rochette, J. T. Blaskovits, F.-G. Fontaine, A. Pron, Y. Li, M. Leclerc, *Chem. Sci.* **2017**, *8*, 3913.
- [360] W. J. Hehre, R. Ditchfield, J. A. Pople, *J. Chem. Phys.* **1972**, *56*, 2257.
- [361] J. P. Perdew, Y. Wang, *Phys. Rev. B* **1992**, *45*, 13244.
- [362] A. D. Becke, *J. Chem. Phys.* **1993**, *98*, 5648.
- [363] G. Raos, A. Famulari, V. Marcon, *Chem. Phys. Lett.* **2003**, *379*, 364.

- [364] N. E. Jackson, B. M. Savoie, K. L. Kohlstedt, M. Olvera de la Cruz, G. C. Schatz, L. X. Chen, M. A. Ratner, *J. Am. Chem. Soc.* **2013**, *135*, 10475.
- [365] S. Liu, Z. Kan, S. Thomas, F. Cruciani, J.-L. Brédas, P. M. Beaujuge, *Angew. Chem. Int. Ed.* **2016**, *55*, 12996.
- [366] S. Liu, X. Song, S. Thomas, Z. Kan, F. Cruciani, F. Laquai, J.-L. Bredas, P. M. Beaujuge, *Adv. Energy Mater.* **2017**, *7*, 1602574.
- [367] C. Adamo, D. Jacquemin, *Chem. Soc. Rev.* **2013**, *42*, 845.
- [368] J.-D. Chai, M. Head-Gordon, *Phys. Chem. Chem. Phys.* **2008**, *10*, 6615.
- [369] H. Sun, C. Zhong, J.-L. Brédas, *J. Chem. Theory Comput.* **2015**, *11*, 3851.
- [370] L. N. Anderson, M. B. Oviedo, B. M. Wong, *J. Chem. Theory Comput.* **2017**, *13*, 1656.
- [371] J. Lu, S. Zhu, Z. Zhou, Q. Wu, G. Zhao, *Int. J. Quantum Chem.* **2006**, *106*, 2073.

## Appendix



**Scheme A1.** Synthesis of the D–A–D segments discussed in Chapter 5.2.



**Scheme A2.** Synthesis of the IDTT-based copolymers discussed in Chapter 5.2.